ADVANCES IN INVERSE TRANSPORT METHODS

AND APPLICATIONS TO NEUTRON TOMOGRAPHY

A Dissertation

by

ZEYUN WU

Submitted to the Office of Graduate Studies of
Texas A&M University
in partial fulfillment of the requirements for the degree of

Doctor of Philosophy

December 2010

Major Subject: Nuclear Engineering

ADVANCES IN INVERSE TRANSPORT METHODS

AND APPLICATIONS TO NEUTRON TOMOGRAPHY

A Dissertation

by

ZEYUN WU

Submitted to the Office of Graduate Studies of
Texas A&M University
in partial fulfillment of the requirements for the degree of

Doctor of Philosophy

Approved by:

Co-Chairs of Committee,	Marvin L. Adams
	William S. Charlton
Committee Members,	Jim E. Morel
	Jean C. Ragusa
	Jianxin Zhou
Head of Department,	Raymond J. Juzaitis

December 2010

Major Subject: Nuclear Engineering

ABSTRACT

Advances in Inverse Transport Methods

and Applications to Neutron Tomography . (December 2010)

Zeyun Wu, B.S., Tsinghua University, China;

M.S.E., Tsinghua University, China;

M.E., Texas A&M University

Co-Chairs of Advisory Committee: Dr. Marvin L. Adams
                                    Dr. William S. Charlton

The purpose of the inverse-transport problems that we address is to reconstruct the material distribution inside an unknown object undergoing a nondestructive evaluation. We assume that the object is subjected to incident beams of photons or particles and that the exiting radiation is measured with detectors around the periphery of the object. In the present work we focus on problems in which radiation can undergo significant scattering within the optically thick object. We develop a set of reconstruction strategies to infer the material distribution inside such objects. When we apply these strategies to a set of neutron-tomography test problems we find that the results are substantially superior to those obtained by previous methods.

We first demonstrate that traditional analytic methods such as filtered back projection (FBP) methods do not work for very thick, highly scattering problems. Then we explore deterministic optimization processes, using the nonlinear conjugate gradient iterative updating scheme to minimize an objective functional that characterizes the misfits between forward predicted measurements and actual detector readings. We find that while these methods provide more information than the analytic methods such as FBP, they do not provide sufficiently accurate solutions of problems in which the radiation undergoes significant scattering.

We proceed to present some advances in inverse transport methods. Our strategies offer several advantages over previous reconstruction methods. First, our optimization procedure involves the systematic use of both deterministic and stochastic methods, using the strengths of each to mitigate the weaknesses of the other. Another key feature is that we treat the *material* (a discrete quantity) as the unknown, as opposed to individual *cross sections* (continuous variables). This changes the mathematical nature of the problem and greatly reduces the dimension of the search space. In our hierarchical approach we begin by learning some characteristics of the object from relatively inexpensive calculations, and then use knowledge from such calculations to guide more sophisticated calculations. A key feature of our strategy is dimension-reduction schemes that we have designed to take advantage of known and postulated constraints.

We illustrate our approach using some neutron-tomography model problems that are several mean-free paths thick and contain highly scattering materials. In these problems we impose reasonable constraints, similar to those that in practice would come from prior information or engineering judgment. Our results, which identify exactly the correct materials and provide very accurate estimates of their locations and masses, are substantially better than those of deterministic minimization methods and dramatically more efficient than those of typical stochastic methods.

ACKNOWLEDGEMENTS

First I would like to express my sincere gratitude to my advisor, Dr. Marvin L. Adams. It is he who initiated and foresaw the significance of this research project, namely developing advances in inverse transport methods and applying them to neutron tomography problems. Dr. Adams spent many hours in countless research meetings with me during the years of my graduate study. I greatly appreciate his advice at every stage of this work and thank him for his help, patience and example in both academic and life in general.

I would also like to express my thanks to the other members of my advisory committee, Dr. Jim E. Morel, Dr William S. Charlton, Dr. Jean C. Ragusa, and Dr. Jianxin Zhou (from Math Dept.), with whom I had many fruitful research communications. Special thanks go out to Qiming Li for his guidance during my internship at Schlumberger Ltd. in Sugar Land, Houston in fall 2008.

I am also grateful to Dr. Wolfgang Bangerth and Dr. Peter Kuchment from the Math Dept., Dr. Mark Everett from the Geophysics Dept., Dr. Jim Ji from the Electrical Engineering Dept., and Dr. Sergiy Butenko from the Industrial Engineering Dept. for their enlightened advice to mitigate the difficulties we encountered in the research.

I would also like to thank all of the wonderful people I've known during my stay in College Station. All of the friendships that have developed throughout my time make my life entertaining and energetic and will be cherished for years to come. It is wonderful to be surrounded by so many loving and caring friends when I take time off from the computer.

Last but not least, I am greatly indebted to my family. My parents miss me so much that they keep informing me to take care of myself during the years that I have been so far away from them. My wife, Yayun Yu, lives with me and always encourages me to devote myself to accomplish the work completely. Without her

support, patience and endless love, I do not think I could have endured the tough process and walked through the long journey to finish this dissertation.

TABLE OF CONTENTS

LIST OF FIGURES

LIST OF TABLES

CHAPTER I

INTRODUCTION

I.A   Background

A radiographic imaging system, no matter what radiation is applied (x-ray, gammas, neutrons, etc), follow the same general principle: that radiation is attenuated on passing through the object of interest. After passing through the object, the remaining beam enters a detector placed on the back side of the object and registers the fraction of initial radiation intensity that has been transmitted by each path through the object. Any inhomogeneous information inside in the object will be finally revealed as a change of radiation intensity in the detector. Fig. I.1 illustrates a typical radiographic imaging system, where the source part is marked as a neutron beam.
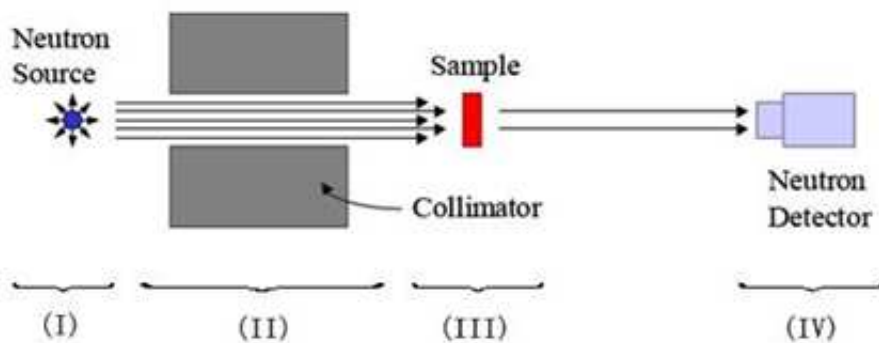
Fig. I.1: An idealized facility configuration for radiographic imaging system.

This dissertation follows the style of *Journal of Nuclear Materials*.

A radiography system traditionally consists four main parts, as illustrated in Fig. I.1: (I) the source; (II) an efficient collimator to control the source beam (usually it is a divergent beam); (III) a sample positioning system; and (IV) a radiography camera or film. This ideal model is sometimes referred as "dynamic radiographic imaging" [1].

Transmission images in standard radiography are captured in the camera with both the sample in place and the sample not in place. The two- and three-dimensional characteristics of the sample could then be determined by the following standard transmission equation, provided that scattered particles can be neglected:

$$I(x) = I_0 e^{-\int_0^x \Sigma_t(s)ds}, \tag{I.1}$$

which yields the result

$$\int_0^x \Sigma_t(s)ds = -\ln\left(\frac{I(x)}{I_0}\right). \tag{I.2}$$

This basic methodology, sometimes referred to as the simple exponential attenuation method (SEAM), has been used successfully for numerous applications. However, when it is applied to highly scattering media, the scattering component of the beam intensity exiting the sample is not adequately specified by SEAM. This leads to decreased system resolution when the scattered particles are recorded at the image plane. This is sometimes called scattering-blur in the realm of optical imaging science. Overcoming the scattering-blur drawback of SEAM has been the focus of a great deal of research and development [1–4].

Before the Computed Tomography (CT) technology was invented, projection-based radiography dominated in radiation imaging applications. Even today, with CT well developed and powerful computers readily available, people in neutron imaging research area, as a relatively small scientific community, still mainly focus on radiographs (films). Basically, tomography ("Tomo" means "to cut" in Greek) refers to the cross-sectional image reconstruction of an object from transmitted and reflected radiation collected by illuminating the object from many different directions [5, 6].

In other words, a tomography imaging system deals with reconstructing an internal image of an object based on its peripheral exiting radiations. The impact of this technology in imaging systems has been revolutionary.

Fig. I.2: Sketch for traditional computer tomography (CT) procedure.

A sketch of a traditional computer tomography system is depicted in Fig. I.2. Similar to the radiography system, the tomography system also includes three main parts: the source beam, the object under investigation, and the detector system. The major difference between tomography and radiography is that tomography relies on computations and the images it produces are reconstructed properties internal to the object.

From a mathematical point of view, tomography reconstruction methods could be classified into two main categories. One is the analytic (or direct) tomography method [5–7], which mainly involves the following principles: (1) Radon transform and inverse Radon transform, which maps and anti-maps a transmission line set to a projected point set; (2) Fourier projection-slice theorem (also referred to as central-slice theorem), which in two dimensions states that the Fourier transform of the projection of a two-dimensional function onto a line is equal to a slice, parallel to the projection line, through the origin of the two-dimensional Fourier transform of that function. One of the most common methods in the analytic tomography reconstruction category is back projection reconstruction (BPR). BPR can be subdivided to simple BPR, filtered BPR, convolution BPR and so on based on the different key

technologies used with it. Among them, the Filtered Back Projection (FBP) is the best known due to the excellent outcome and wide usage in medical and non-medical applications.

Another category of tomographic reconstruction methods is the iterative image reconstruction (IIR) method [8–10]. BPR usually demands projections from hundreds of different directions, but in some scenarios it is unable or barely able to obtain enough projections. Also, recall that BPR does not account for scattered particles and thus is of questionable value for objects in which particles undergo significant scattering. In these cases BPR yields poor results and IIR could be a good alternative. IIR first defines a forward model, which is capable of calculating the detector responses for the beam passing through a known object (where "known" means the cross sections defining the object are known). In addition to this forward model, an inverse method is also needed to influence the "guess" of the object structure. The inverse method typically works with an objective function, which connects the information provided by forward model with that of the real measured images. The forward model can then be repeated using a more accurate guess provided by the inverse method and the system goes to the next iteration. These iterations continue until the calculated image matched the measured image to within some tolerance (i.e., the objective function is minimized). This is the fundamental concept behind the iterative imaging reconstruction (IIR) schemes. IIR schemes mainly differ in their choices of forward models and how the spatial distributions of the optical properties of the medium are updated.

I.B Research Objective

Neutron transport within a non-multiplying object with arbitrary anisotropic scattering can be described with multigroup transport equation [11–13]:

$$\underline{\Omega} \cdot \underline{\nabla} \psi_g(\underline{r}, \underline{\Omega}) + \Sigma_{tg}(\underline{r}) \psi_g(\underline{r}, \underline{\Omega}) =$$

$$\sum_{g'=1}^{G} \sum_{l=0}^{\infty} \sum_{m=-l}^{l} Y_{lm}(\underline{\Omega}) \Sigma_{sg' \to g}^{l}(\underline{r}) \phi_{lm,g'}(\underline{r}) + S_{ext,g}(\underline{r}, \underline{\Omega}) \quad , \tag{I.3}$$

where $\Sigma_{tg}(\underline{r})$ and $\Sigma_{sg' \to g}(\underline{r})$ are the total and scattering macroscopic cross sections associated with each energy group g. These functions are determined by the material composition of the interacting object. We use $\underline{r}$ to denote the position vector and $\underline{\Omega}$ to denote the unit vector in the direction of particle travel. S is a volumetric source rate density and Y_{lm} is a spherical-harmonics function.

The forward transport problem is to solve for the angular flux ψ_g if the physics constants $\{\Sigma_{tg}, \Sigma_{sg' \to g}\}$ are provided as functions of position. The angular flux ψ_g determines the scalar flux ϕ_g and current $\underline{J_g}$ through the following relationship:

$$\phi_g(\underline{r}) = \int_{4\pi} \psi_g(\underline{r}, \underline{\Omega}) d\Omega, \tag{I.4}$$

$$\underline{J_g}(\underline{r}) = \int_{4\pi} \underline{\Omega} \psi_g(\underline{r}, \underline{\Omega}) d\Omega. \tag{I.5}$$

In an inverse transport problem, on the contrary, the usual task is to infer the material distribution within the object based on the limited information about angular flux ψ that is obtained from detections of exiting radiation. Most methods for solving such problems have focused on inferring cross sections information from the detection measurements and have not explicitly addressed the issue of inferring material distribution from these constants. A familiar example of an inverse problem in radiation transport is tomography in medical applications, which attempts to reconstruct the interior of a patient from transmitted and reflected radiation collected while illuminating the patient from different directions [5, 6].
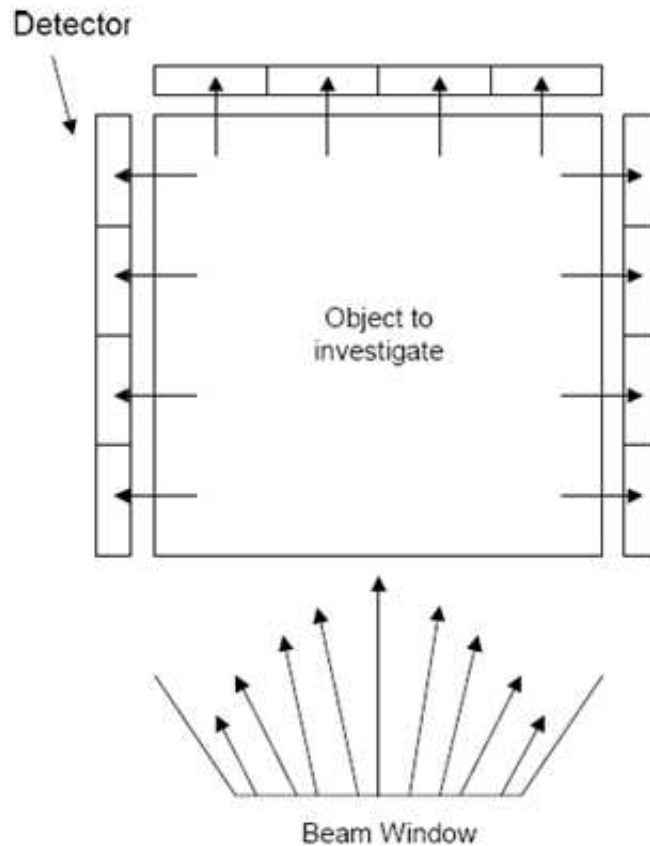
Fig. I.3: Schematic of the inverse problem we address in this research.

We use "inverse transport" and "tomography" to mean the inference of material distribution inside an object based upon detection and analysis of radiation emerging from the object. We assume that the object is subjected to incident neutron beams and we measure the exiting radiation with detectors around the periphery of the object. Fig. I.3 depicts a two-dimensional cross section of the beam-object-detector system in an exemplified problem. The source beam is not necessarily mono-directional because even a collimated beam has some physical divergence in practice. The detectors can be collimated such that they only record radiation coming from a particular cone of directions. The beam is incident into the object under investigat-

ing from one side, and the detectors are placed in other three periphery sides of the object for the purpose of not only detecting the direct transmitted radiation from the back side of the object but also the radiation exiting the left and right side of the system due to scattering. This design is very beneficial for problems in which particles undergo large numbers of scatterings [3]. Each side detector measures the scattered neutron component at a variety of locations around the object, and these scattered components could be used to help estimate the source of neutron reactions in the sample. This information could lead to a more accurate reconstruction of the surveyed object.

In many cases, especially when particles are likely to undergo multiple scattering events within the object, inverse problems are ill-conditioned and thus very difficult to solve. This is the class of problems that we address. When standard radiography (and tomography) methods are applied to highly scattering objects the results are usually inconclusive or misleading, because the scattered component of the exiting radiation overwhelms the transmitted component [3]. The task of this research is to develop systematic approaches to reconstruct the material distribution inside an unknown object even when scattered particles dominate the exiting radiation.

One of the more common tomographic techniques is the filtered back projection (FBP) method [5, 6, 14–17]. In this technique, the projection data can be considered as line integrals along the particle beam lines and the tomographic method recovers the density function (the images) via a projection process applied to the filtered Fourier transform of the line integrals. As noted above, for highly scattering objects this method has difficulty because the scattered particles can overwhelm the signal from the un-scattered particles. Standard back projection techniques applied in X-ray tomography meet limited success when applied to neutron tomography, again because of scattering [2]. Even with collimated beams and collimated detectors FBP still fails for optically thick, highly scattering problems. We will illustrate this issue with example FBP results in Chapter II.

Neutron radiography and tomography offer significant benefits for some applications compared to systems that use other particles [18–24]. For example, neutron radiography exhibits better resolution given low atomic-number materials, such as carbon, water, etc., especially when these materials are enclosed within heavy metals, while imaging systems based on other particles would usually fail in these situations [18, 25]. Although the research described here is not limited to neutrons, it could significantly broaden the applicability of neutron tomography by allowing it to treat highly-scattering objects.

In this research, we focus on tomography applications with optically thick objects containing highly scattering materials and we develop a systematic reconstruction strategy to infer the material distribution inside such objects. While our techniques should be applicable to various kinds of radiation, we use neutrons in our examples. In our examples we assume the availability of radiation measurements on all sides of the object except the one on which the probe beam is incident. In next section we present a sketch of our proposed methodology and point out the advances that our research has produced.

I.C   Our Methods in This Research

Due to the failure of analytic tomography methods for thick and high scattering objects, the reconstruction methods we focus in this research mainly fall into the second category described in section I.A, namely, the iterative-based image reconstruction methods. We cast the inverse problem as an optimization problem and consider iterative approaches to minimizing a functional that serves as a measure of the difference between the real object and the latest guess (iterate). In this approach, which is not new, a forward model capable of calculating the detector response does so with an initial "guess" of the material distribution in the unknown object. An inverse model then creates a better "guess" of the object structure in every iterative loop. The forward model can then be repeated using the more accurate guess. This

process continues until the determined material distribution minimizes the functional that characterizes the difference between predicted and measured results. This is the fundamental concept behind the model-based iterative imaging reconstruction (MO-BIIR) schemes. MOBIIR schemes mainly differ in their choice of forward model and how the spatial distributions of the interaction properties (cross sections, in the case of neutrons) of the medium are updated.

A variety of tomography methods based on MOBIIR schemes have been studied in the past [26–37]. While these studies have principally been in the area of optical-photon or low-energy x-ray medical imaging, they have led to a variety of creative methods and their general principles can be extended to neutron imaging. Some of these studies are based on diffusion theory [26–30, 32, 33, 35] and some of them are developed with transport theory [31, 34], but methods applied to these studies are dominantly deterministic. We also notice many researchers have attempted to address the inverse problems with stochastic-based optimization methods such as simulated annealing (SA) [38–44], genetic algorithms (GA) [45–49] and other combinatorial tomography (CT) methods [50–52] in variety of applications. The deterministic methods are generally applied to simple models and can be susceptible to getting stuck in local minima, while the stochastic methods have advantages regarding these concerns but normally require substantial computational time.

In this work we present a methodology that combines both deterministic and stochastic iterative methods within a systematic approach for applying constraints. The constraints can enforce physical realities as well as postulates about the contents of the object. Our approach dramatically reduces the effective dimension of the parameter space that is ultimately searched, which dramatically decreases computational effort while dramatically increasing the chance of a solution that is close to reality. The idea of combining deterministic and stochastic methods in image reconstruction has gained interest among researchers before. Dedkova [53] recently proposed a new algorithm based on the combination of deterministic and stochas-

tic methods to be used to obtain the best results of a reconstruction process of the surface conductivity distribution with the applications in electrical impedance tomography (ECT).

However, to our knowledge the methodology that we propose here is new. In our hierarchical approach we begin by learning some characteristics of the object from relatively inexpensive calculations, and then use the knowledge from such calculations to guide successively more sophisticated calculations. Our algorithm proceeds as follows:

1. **Gradient-based deterministic search:** Here we apply the basic deterministic search algorithm, in which cross-section parameters are the unknowns. However, we employ a simplified transport model (for example one-group or two-group transport or diffusion), perhaps on a spatial grid that is not as fine as the ultimate desired resolution. Thus, the dimension of the search space is manageable.

2. **Cell Grouping:** Based on the results from the deterministic optimization process, we group into *regions* the cells that are likely to contain the same material. Another kind of region is identified as likely to contain one or more interfaces between materials. Henceforth each cell will be associated with a region, with materials varying by region according to some chosen constraints (see step 4). After this grouping, the forthcoming search process will work on regions rather than cells, which greatly reduces the search-space dimension and thus greatly saves computation time.

3. **Material Restriction:** The purpose of this step is to narrow the material candidates to be considered in each region. Given the few-group parameters found in step 1 for the cells in a given region, an algorithm determines which materials could realistically have few-group parameters that are similar, and

then places those materials in the material candidate library (MCL) for that region.

4. **Further Constraints:** To further reduce the search space we can impose other constraints that embody prior knowledge or that are postulated. For example, we could constrain the algorithm to consider only material sub-objects with relatively sharp boundaries as opposed to fragmentary objects. We could bias the stochastic search process so that it favors a small number of material regions embedded in a single-material background. The chosen constraints restrict the kinds of material distributions that will be considered as viable candidates in the final step.

5. **Stochastic-based Combinatorial Optimization:** In this stage we produce a sequence of guesses for the material distribution and compute the objective function for each guess. We apply a stochastic-based heuristic search method, informed by the constraints and biases chosen in step 4, to select a material in each cell. At this stage a full-fidelity transport forward model is applied to evaluate the objective function for each material distribution. The algorithm terminates either when a suitably small objective function is found or when an iteration limit is reached.

The main contribution of our research is this overall approach, which systematically combines deterministic and stochastic methods within a framework that applies significant practical constraints, thereby dramatically improving solutions while dramatically reducing costs. In addition, we have introduced or employed modest improvements to the deterministic and stochastic optimization methods themselves. In the deterministic optimization stage, we have implemented several improvements to the approach described by Klose et al. [36,37] and corrected by Scipolo [54]. First, we have created a variable change to impose non-negativity constraints on cross sections; this is described in a forthcoming publication [55]. To increase efficiency we

apply a Krylov subspace iterative technique that speeds up each forward calculation. We employ a nonlinear conjugate gradient (CG) [56] updating scheme as the heart of our search procedure and integrate Brent's method [57] into the associated line-search algorithm. We also allow illumination of the object from all four sides of a rectangular object in 2D, with each illumination producing a set of measurements. All four sets are included in the sum that defines the objective function.

In stochastic optimization stage, the key feature in our approach is that we treat the *material* (a discrete quantity) as the unknown, as opposed to individual *cross sections* (continuous variables). This changes the mathematical nature of the problem, and in fact greatly reduces the dimension of the search space. It also automatically imposes the important constraint that cross sections for a given region must be cross sections of a real material. We incorporate further constraints that filter out unrealistic configurations and thus prevent the algorithm from wasting time computing them with the (expensive) high-fidelity forward transport model.

To illustrate our methodology we consider model problems in a two-dimensional X-Y Cartesian coordinate system. We assume an incident beam of thermal neutrons from one side of the object at a time, with measurement of exiting radiation from other three sides. Our forward solver employs a single (thermal) energy group, the discrete-ordinates method for angular discretization, an analytic treatment of the first-collision source, and the step-characteristic method for spatial discretization. In this research we do not consider the complications of model or measurement errors - our aim here is to evaluate whether our methodology works in a simple setting that permits sharp analysis and sharp conclusions.

I.D   Overview of Chapters

In this introductory chapter we have given a background discussion, described the objective of our work, and provided a brief summary of the methods we devise

with a highlight of the advances we introduced in this research. Our subsequent discussions are organized as follows.

We begin in Chapter II by explaining the fundamentals of FBP-based analytic tomography methods and applying them to test problems of interest. Our application uses the general Monte-Carlo simulation code MCNP [58] to construct simulated "measurements" for our tests. We give a detailed description of the MCNP model we develop and the radiation tallies that we acquired. We explore the FBP-based reconstruction method using a MATLAB-based utility that we have adapted to reconstruct the total cross section of the test problem. The local tomography method, a derivative method of FBP method, is also investigated in this chapter to reconstruct the interface area of the material distribution. The results obtained in this chapter illustrate the conclusion that FBP-based methods may provide certain useful information in problems with some or no scattering, but in highly scattering problems these methods will generally fail even with collimated beams and detectors. This motivates us to consider a different class of methods.

In Chapter III we describe and illustrate deterministic optimization methods, focusing the one that we apply as the first step in our hierarchical approach. We follow the gradient-based iterative scheme based on the work of Klose et al. [36, 37] and Scipolo [54], but we also devise methods that address the difficulties we encountered with this scheme. These contributions to the deterministic optimization procedure are highlighted in the introductory section of the chapter.

In Chapter IV the main innovations of our work, most of which can be viewed as advanced dimension-reduction techniques. We describe our hierarchical approach in detail and also describe particular algorithms that can be used at each step in our hierarchy, including algorithms that accomplish the following tasks: cell grouping, material restriction, and combinatorial optimization with smart constraints imposed.

In Chapter V we present computational results from a range of test problems to illustrate the efficiency and advantages of our systematic approach to inverse

problems. We conclude in Chapter VI with a summary of our salient points and our view of the future potential for application and extension of this research.

CHAPTER II

ANALYTIC TOMOGRAPHY METHOD

II.A   Introduction

The methodology we apply in this research to solve the inverse problem is iterative based optimization. Before we discuss our approach, in this chapter we discuss the application of analytic tomography methods to the problems of interest. The purpose is to understand the difficulties that traditional tomography methods encounter if they are applied to inverse problems with thick and highly scattering objects.

The terminology "analytic tomography", also referred to as "direct tomography", applies to reconstruction methods based on the underlying idea of the Radon Transform [5, 6, 59], e.g., line integrals along projection trajectories. With some inversion techniques such as filtered back projection (FBP) applied to the projections, analytic tomography methods are capable of reconstructing material properties to infer what is inside an object without opening it up [7, 60]. Analytic tomography methods have gained significant interest among researchers and have been applied to variety of applications [14–17, 61] for several decades. Although most of these applications principally address photon-based tomography, we illustrate the method using neutron-tomography examples.

The usual material property that the FBP method reconstructs is material total cross section, or attenuation coefficient. Such properties are normally referred to as *density functions* of the positions within the object. They are determined by the composition of the material and in most cases are sufficient to infer the material itself. But under some circumstances, we are interested to know the interface area between two different materials rather than the materials themselves [62–64]. Local tomography has been invented to achieve this goal.

Local tomography, also known as Lambda tomography or "high frequency tomography" was first introduced respectively by Vainberg et al. [65] and Smith & Kein-

ert [15] independently. The method was further extended by Kuchment et al. [16] and continues to be extensively studied [17, 66–68]. Local tomography recovers *the first derivative of the density function* rather than density function itself. This can offer advantages compared to the traditional tomography [16, 69].

Though the analytic tomography methodologies are generally easy to apply and fast in process, they can fail if the underlying assumption of the Radon Transform - that the exiting radiation is simply the entering radiation multiplied by an attenuation factor that depends on an integral along the beam path - is not satisfied, as is the case for example if the exiting radiation includes a significant portion of scattered radiation. We will elaborate this conclusion after presenting some results from applying these methods to out test problem in the section E of this chapter.

We are especially interested in local tomography methods because of their potential to provide material interface locations, which could provide useful constraints on a more detailed optimization search procedure. However, as we show later in this chapter, local tomography also fails for optically thick objects with significant scattering.

II.B   Analytic Reconstruction Method

In this section we will briefly go through the mathematical basis of analytic tomography based traditional filtered back-projection (FBP) method, which is dominantly applied in computerized tomography (CT). Most of the materials in this section could be found in details in the Chapter 3 of the Kak & Slaney's book [5]. Essentially, the FBP based analytic reconstruction method could be summarized by the following three major parts:

II.B.1   Line integral to obtain projections/measurements

A line integral represents the integral of some properties of the object along a line. These integrations work as set of projections/measurements required for analytic tomography methods to recover the image of the cross section of an object. In other words, the necessary projections required for analytic reconstruction are provided by the line integral procedure. Through line integral, the physical properties along the integration line are mapped into one projection, and if we could map this information back from the projection, we would recover the corresponding properties along the line. After all integration lines are recovered and analyzed together, the whole cross section image is recovered. This is the concept of analytic tomography method. Therefore the line integral works as the foundation of the methodology.

To better describe the fundamentals of line integrals, we use Fig. II.1 as an example: the object is represented by a two-dimensional function $f(x, y)$ and each integral line is determined by the (θ, t) parameters. Here θ is the angle of a set of parallel lines, relative to some reference direction, and t is a coordinate along an axis perpendicular to the lines.

The projection $P_\theta(t)$ in Fig. II.1 could be obtained through the following line integral as:

$$P_\theta(t) = \int_{-\infty}^{+\infty} \int_{-\infty}^{+\infty} f(x, y)\delta(x\cos\theta + y\sin\theta - t)dxdy. \tag{II.1}$$

Here $x\cos\theta + y\sin\theta = t$ represents the equation of line AB in Fig. II.1 and the function $P_\theta(t)$ is known as the Radon Transform of the function $f(x, y)$.

II.B.2   Fourier slice theorem (FST)

The Fourier Slice Theorem is the key to analytic tomographic imaging systems. It discloses the relationship between the measured projection data and the two-dimensional Fourier transform of the density function in the cross sectional object, which is represented in Fig. II.2.
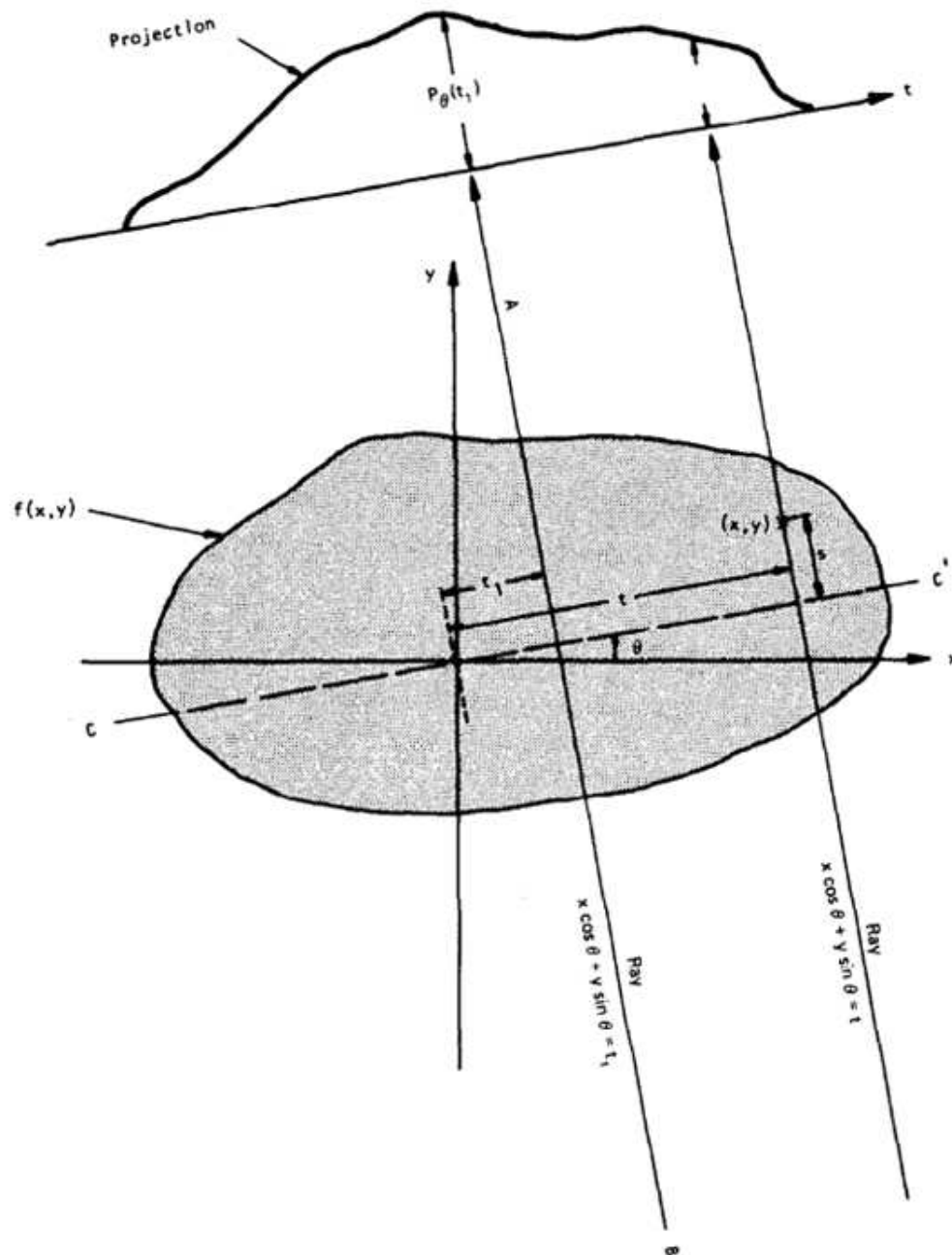
Fig. II.1: $P_\theta(t_1)$ is the projection of the density function $f(x, y)$ shown from an angle θ and a position t_1. [70]
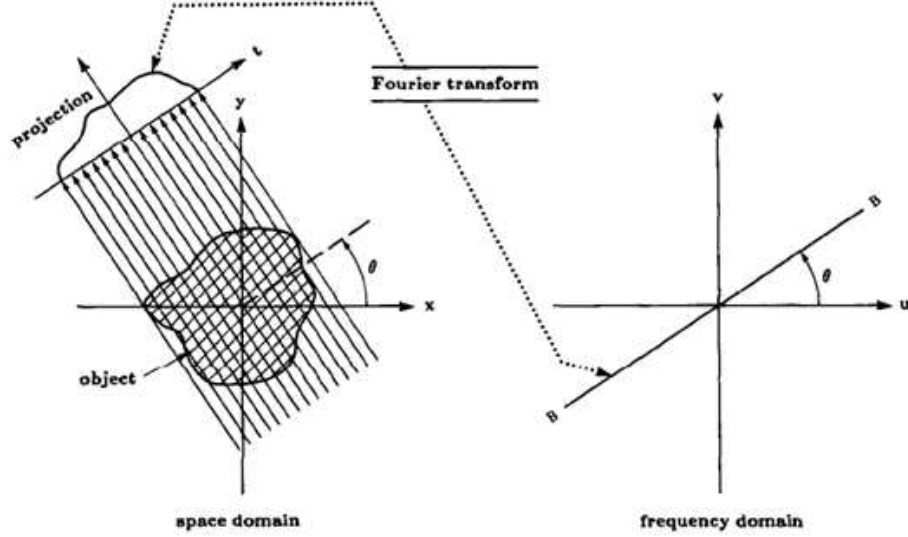
Fig. II.2: The Fourier Slice Theorem relates the Fourier transform of a projection to the Fourier transform of the object along a radial line. [71]

The two dimensional Fourier transform applied to $f(x, y)$ is

$$F(u, v) = \int_{-\infty}^{+\infty} \int_{-\infty}^{+\infty} f(x, y) e^{-j2\pi(ux+vy)} dx dy. \tag{II.2}$$

If we apply Fourier transform on the projection $P_\theta(t)$ into its frequency domain, we have

$$S_\theta(\omega) = \int_{-\infty}^{+\infty} P_\theta(t) e^{-j2\pi\omega t} dt. \tag{II.3}$$

Then the Fourier Slice Theorem (FST) states that

$$S_\theta(\omega) = F(\omega \cos\theta, \omega \sin\theta). \tag{II.4}$$

The proof of this statement can be found in [5]. Mathematically, FST in two dimensions states that the Fourier Transform of the projection of a two-dimensional function f onto a line is equal to a slice through the origin of the two-dimensional Fourier transform of that function, with the slice taken parallel to the projection line. This is a very important result which indicates that by taking the projections of a

density function at number of angles and Fourier transforming each of these projections, we can determine the values of $F(u,v)$ on radial lines as shown in Fig. II.2. If an infinite number of projections are taken, $F(u,v)$ would be known at all points in the uv-plane. With the known $F(u,v)$, the density function $f(x,y)$ can be retrieved by using the inverse Fourier transform on $F(u,v)$. This leads to the third part of the basic analytic tomography method.

II.B.3 Filter back projection (Inverse transform)

The inverse reconstruction method applied to specific problems depends the type of projection data measured. For simple description purpose, we discuss the methods here based on parallel beam projection data, which is also the source beam we are interested in for this research.

The two variable inverse Fourier transform is described as

$$f(x,y) = \int_{-\infty}^{+\infty} \int_{-\infty}^{+\infty} F(u,v)e^{j2\pi(ux+vy)}dudv. \tag{II.5}$$

By changing the rectangular coordinate variables (u,v) into polar coordinate variable (ω, θ), and applying the property of symmetry and the results from Fourier Slice Theorem, we could change the form of Eq. (II.5) into

$$f(x,y) = \int_0^{\pi} \left[\int_{-\infty}^{+\infty} S_\theta(\omega) |\omega| e^{j2\pi\omega t}d\omega \right] d\theta, \tag{II.6}$$

where $t = x\cos\theta + y\sin\theta$.

To better understand Eq. (II.6) we obtained above, we define

$$Q_\theta(t) = \int_{-\infty}^{+\infty} S_\theta(\omega) |\omega| e^{j2\pi\omega t}d\omega \tag{II.7}$$

and name it as "filtered projection" which indicates a filtering operator worked on $S_\theta(\omega)$. Then we have

$$f(x,y) = \int_0^{\pi} Q_\theta(x\cos\theta + y\sin\theta)d\theta. \tag{II.8}$$

Eq. (II.8) represents the pure "back-projection" process.

It has been shown [5, 14, 16] that

$$Q_\theta(t) = \frac{1}{2\pi^2 t} * \frac{\partial P_\theta(t)}{\partial t} = \text{Hilbert Transform of } \frac{\partial P_\theta(t)}{\partial t}. \tag{II.9}$$

So the back projection can also be represented as

$$f(x, y) = \int_0^\pi H_t \frac{\partial P_\theta(t)}{\partial t} d\theta. \tag{II.10}$$

Eq. (II.8) or Eq. (II.10) states that each filtered projection is to be "back pro-jected" and makes the same contribution to the reconstruction of all those points on the line associated with this projection. Therefore the reconstruction process of analytic tomography is to smear back each filtered projection to recover the image plane.

II.C   Local Tomography

Local tomography recovers a function different from the density function f , which is the goal of most tomography methods. To illuminate this method and some advantages behind this method, we introduce local tomography following the logic of lectures from Faridani [17].

We start this section with the definition of line integral as described in Eq. (II.1)

$$P_\theta(t) = \int_{-\infty}^{+\infty} \int_{-\infty}^{+\infty} f(x, y)\delta(x \cos\theta + y \sin\theta - t)dxdy.$$

By performing the same procedure as we addressed in the previous section, the reconstructed function $f(x, y)$ would be

$$f(x, y) = \int_0^\pi H_t \frac{\partial P_\theta(t)}{\partial t} d\theta. \tag{II.11}$$

This equation could also be presented as the following form:

$$f(x, y) = \int_0^\pi [\Lambda P_\theta(t)]d\theta, \tag{II.12}$$

here the sign Λ denotes as Calderon's operator [66], which is defined as

$$\Lambda = \sqrt{-\Delta}, \text{ where } \Delta = \text{Laplacian operator.}$$

A local tomography method, in contrast to the traditional analytic tomography, does not attempt to reconstruct the function f itself but instead produces the related function $Lf = \Lambda f + \mu\Lambda^{-1}f$, which is derived as [17,66]:

$$\Lambda^{-1}f = \int_0^\pi [P_\theta(t)]\, d\theta, \tag{II.13}$$

$$\Lambda f = \int_0^\pi [-\Delta P_\theta(t)]\, d\theta. \tag{II.14}$$

Here Eq. (II.13) is just direct back projection operated on $P_\theta(t)$ and easy to apply. To implement Eq. (II.14), we notice the Fourier transform of $-\Delta P_\theta(t)$ is

$$
\begin{aligned}
&\int_{-\infty}^{+\infty} [-\Delta P_\theta(t)]\, e^{-j2\pi\omega t} dt \\
&= -(j\omega)^2 \int_{-\infty}^{+\infty} P_\theta(t) e^{-j2\pi\omega t} dt \\
&= \omega^2 \int_{-\infty}^{+\infty} P_\theta(t) e^{-j2\pi\omega t} dt \\
&= \omega^2 S_\theta(\omega)
\end{aligned}
,
$$

where $S_\theta(\omega)$ is defined in Eq. (II.3), so we could change Eq. (II.14) into

$$\Lambda f(x,y) = \int_0^\pi \left[\int_{-\infty}^{+\infty} S_\theta(\omega)|\omega|^2 e^{j2\pi\omega t} d\omega \right] d\theta. \tag{II.15}$$

This is the final back projection formula we obtained for local tomography, analogous to Eq. (II.6) in traditional analytic tomography methods.

Local tomography does not recover the correct density function f, however it yields a function Λf which has exactly the same singularities as f in the sense that both functions have the same wavefront sets [16]. Therefore this method has many advantages. First, it is local (which gives local tomography its name). This means that in order to recover the value of Λf at some point x, one needs only the Radon data $P_\theta(t)$ for lines passing close to the point x; this is not true for the actual

inversion formula Eq. (II.6). Another advantage is that Λf has singularities located at the same positions as the ones of f, but those of Λf are much 'stronger' than those of f (and hence are significantly highlighted in an image); the reason for this is that Λ is of positive order. Hence, if one is only interested in the singularities of f, one would be much better off using the local tomography formula in Eq. (II.15) rather than the actual tomography formula in Eq. (II.6). This advantage is the particular reason that we interest in local tomography in our research. The singularity of our interest is a simple discontinuity in f which could be used to infer the material interface inside the investigating object. One more additional advantages of local tomography include the fact that it is often computationally simpler and the local experimental data often contains fewer errors since, for example, demagnification may not be required [66].

II.D MCNP Simulation

As described in the previous sections, we know that it is obligatory to obtain a number of projections before we can perform analytic tomography methods to reconstruct the density images as we desire. In this research we obtain the requisite projections by carrying out computational simulations of experiments with Monte-Carlo modeling and simulation.

We use the general Monte Carlo transport code MCNP [58] to model and simulate the beam-object-detector system. The schematic layout of the our test problem and configuration for the computational experiment is illustrated in Fig. II.3.

As shown in Fig. II.3, an investigated object with square shape (10cm $\times$ 10cm in dimension) is composed of two materials: water and iron. It is subjected to a plane mono-directional neutron source defined with thermal Maxwell energy spectrum. An array of 20 detectors, each 0.5 cm wide, is placed on the other side of the object. They measure the radiation emerging from the object after being transmitted through or scattered by the materials in the object.

(a) X-Y View   (b) X-Z View
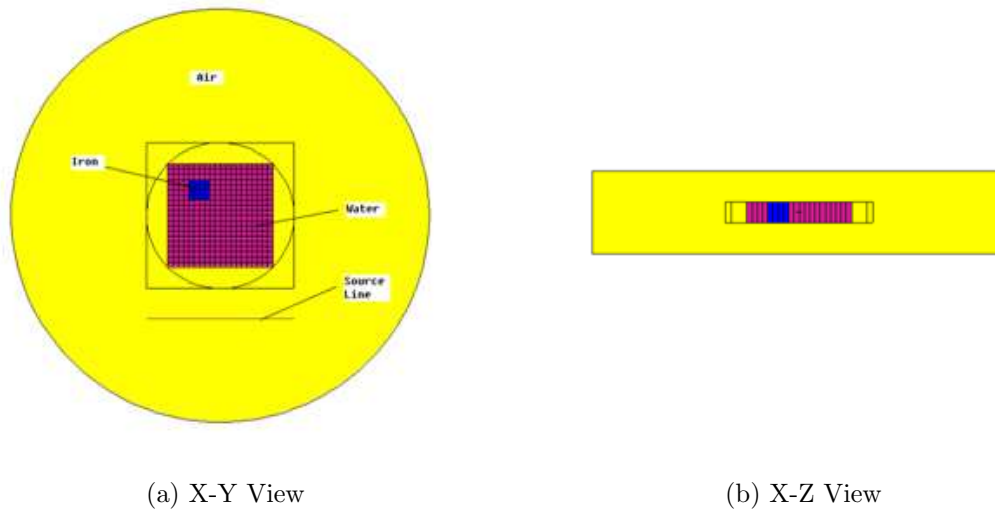
Fig. II.3: Test problem layout and experimental configuration in MCNP.

The plane neutron source in Maxwell spectrum is defined with the following MCNP inputs:

```
sdef    pos=0 -2 0 vec=0 1 0 dir=1 erg=d2 y=-2 x=d3 z=d4
sp2     -2 2.5e-8        $ Maxwellian thermal energy spectrum
si3     h -1.42 1.42
sp3     d 0 1
si4     h -2 2
sp4     d 0 1
```

The materials in the test problem are defined in MCNP as below:

```
m1      1001 -0.111894   $ water
        8016 -0.888106
m2      26000 -1.000000  $ Iron
m3      6000 -0.000124   $ C(air)
        7014 -0.755268   $ N
        8016 -0.231781   $ O
```

```
18000 -0.012827  $ Ar
```

The simulation procedure of the test problem is depicted in the Fig. II.4. The neutron particles coming from the beam are incident to the object, and since the object is optically thick comparing to the mean free path (mfp) of the neutrons with thermal energy range, most of initial interactions (absorption and scattering) happen within 2 to 3 mfp (the thermal neutron mfp in water is around 1.5 cm) of the incident surface. Therefore only a small percentage of neutrons are able to transmit uncollided through the object and reach the surface where detectors are placed.
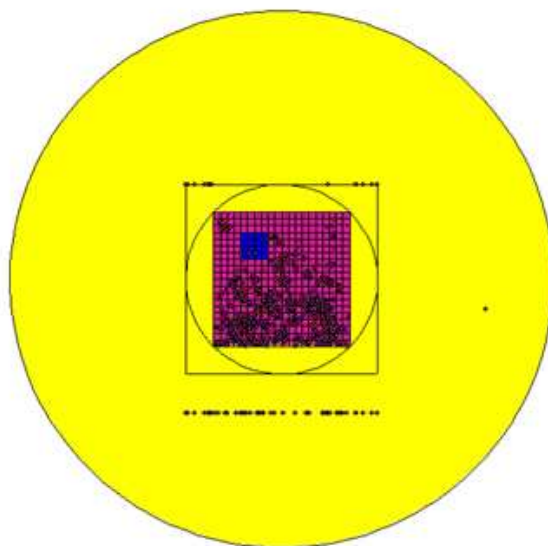
Fig. II.4: Particles transport procedure simulated in the test problem by MCNP.

We perform an experimental simulation with different types of tally in MCNP to approximate the detector readings of the transmitted radiation exiting the back side of the object. The detector reading is collimated because we attempt to preserve the direct transmission particle information as much as possible. The definition of different tally for collimated detector readings in MCNP is written as:

```
c Tally section
```

```
fq0      s c $ Change the order of tallies output
c F1 Tally
f11:n    4
fs11     -100 -101 -102 -103 -104 -105 -106
         -107 -108 -109 -110 -111 -112 -113
         -114 -115 -116 -117 -118 -119 -120
sd11     (1 20r 1)
c11      0 0.996194698 1  $ polar anger from 180-90, 90-5, 5-0.
c F2 Tally
f12:n    4
fs12     -100 -101 -102 -103 -104 -105 -106
         -107 -108 -109 -110 -111 -112 -113
         -114 -115 -116 -117 -118 -119 -120
sd12     (1 20r 1)
c12      1
c F5 Tally
fir15:n  0 5.1 0 7r nd $ Array of point detectors
c15      -1 1
fs15     -5 19i 5
```

The measurements obtained in different tally type is illustrated in Fig. II.5. The plots in Fig. II.5 has been normalized for comparison purpose. We find although different measurements from different tally type have differences in magnitude, they almost follow the same profile (see Fig. II.5). Since the magnitude in measurements don't influence the tomography results [5], for the consideration of computational cost (For example, F5 tally normal takes much longer time to compute than F1 tally.), in the later on experiments we only count collimated current (F1 tally with c card in MCNP) exiting the surface of the object as the transmitted projection, which is needed for analytic tomography. A dummy disk is attached with the object
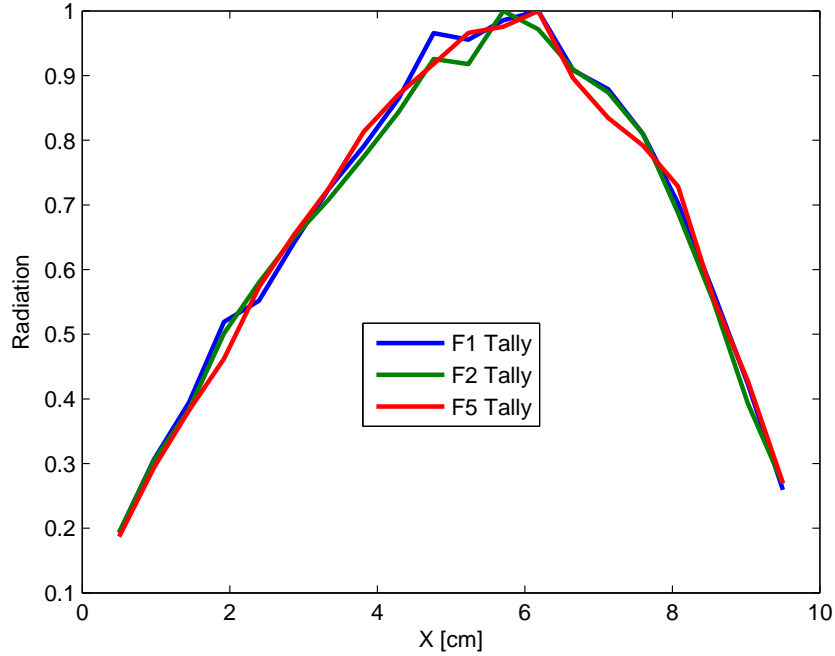
Fig. II.5: Comparison of normalized measurements from different MCNP tally type.

(see Fig. II.3) to work as a coordinate which stays invariant when object is rotated as described in the forthcoming paragraphs. The full MCNP input deck for the modeling and simulation of the test problem can be found in Appendix A.1.

To meet the conditions of most CT methods, we must obtain simulated measurements from multiple groups of projections. We achieved this goal by rotating the system around an axis through the center of the system. However, instead of rotating the source and detector system, we rotate the object with the source beam and detector system invariant. The tool mcnp_pstudy [72] is used for this. Mcnp_pstudy allows the complete parameter space of all cases to be specified in a single MCNP input deck, and automatically generates the required input decks and submits the full set of cases to a Linux cluster for computation. The rotating procedure is demonstrated with the multiple pictures in Fig. II.6.

In Fig. II.6 we only displays six scenarios as exemplified cases; however, in the experiment we rotate the object uniformly in 20 directions from 0 to 360 degrees,
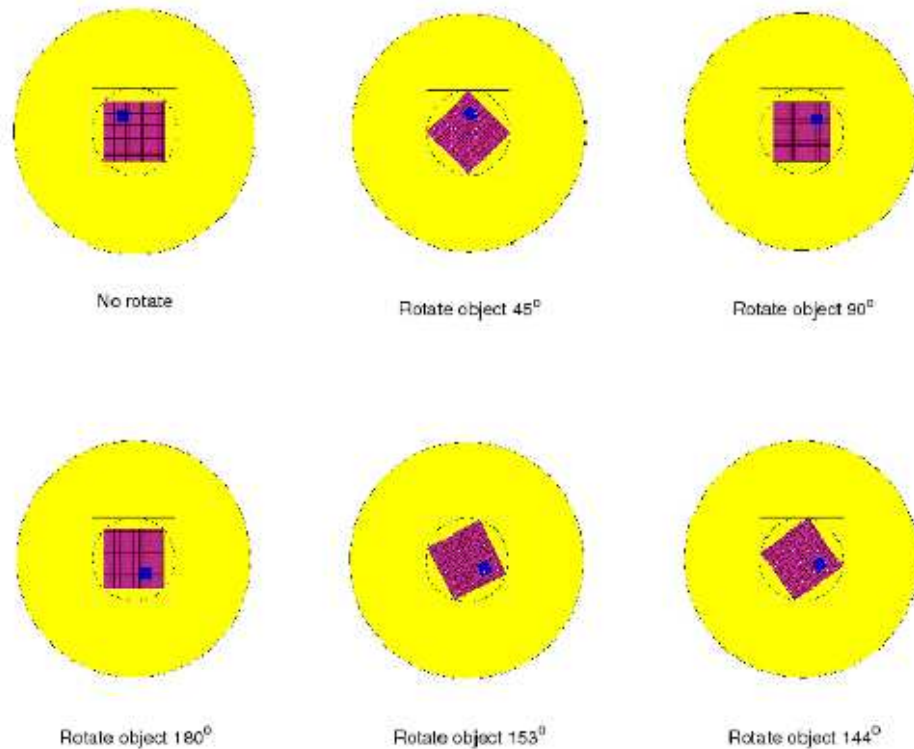
Fig. II.6: Rotate the object in different angles.

collecting 20 sets of projection information, and each projection has 30 detector readings uniformly distributed along the back side of the object. All these projections are used in analytic tomography methods to recover the density image associate with our test problem in Fig. II.3. The input source of the test problem in the format of mcnp_pstudy is attached in Appendix A.2.

The simulated count rates in the collimated detectors are shown in Fig. II.7 for five of the 20 different orientations of the object.

As we expect, because of the iron inclusion embedded in the upper left region of the object (see Fig. II.3), an asymmetry exists in the plot profile with no rotation. This information is automatically used in the reconstruction procedure. With
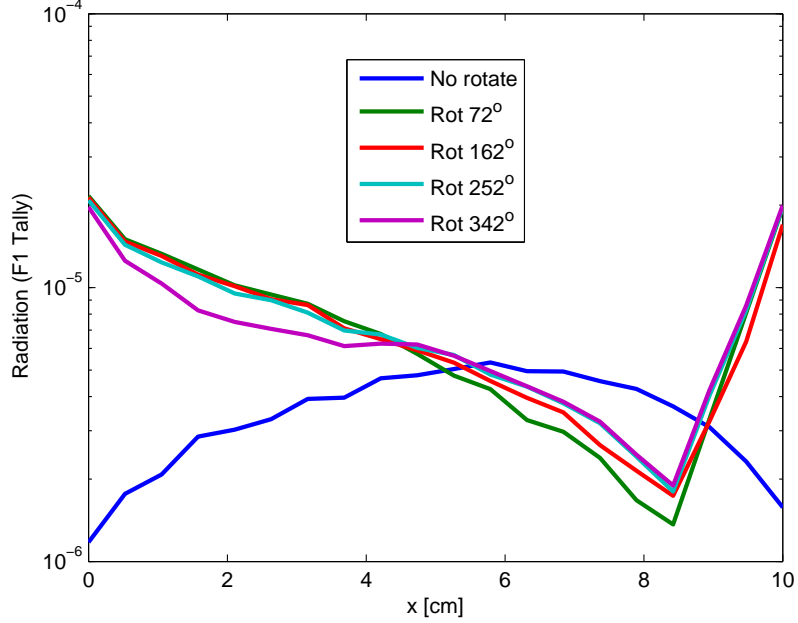
Fig. II.7: Transmitted radiation measured with object rotated in different angle.

the radiation detection information available, we are ready to perform tomography algorithms to recover the tomogram of our interest.

II.E Implementation and Results

Before we perform back projection operations on the measurements, there is one more thing to be clarified. The density image associate with the test problem we attempt to recover here is actually the total cross section distribution among the object. It is described in the simple attenuation model

$$I_\theta(t) = I_0 e^{-\int_{-\infty}^{+\infty} \Sigma_t(x,y)ds}. \tag{II.16}$$

To map Eq. (II.16) to the form of Radon transform in (1), we do the following manipulation

$$P_\theta(t) = \ln\left(\frac{I_0}{I_\theta(t)}\right) = \int_{-\infty}^{+\infty} \int_{-\infty}^{+\infty} \Sigma_t(x,y)\delta(x\cos\theta + y\sin\theta - t)dxdy. \tag{II.17}$$

Eq. (II.17) discloses the relationship between the measurements yielded from MCNP simulation and the projections required for the filtered back projection process. Now we are ready to employ a MATLAB-based FBP utility to recover the total cross section image associated with the test problem.

The reconstructed Σ_t image we obtained from this experiment is shown in Fig. II.8. We see no evidence of the iron inclusion. Recall that the incident beam has a Maxwellian distribution and note that the cross section is a function of neutron energy. This means that the attenuation of the uncollided beam intensity is not as simple as is shown in Eq. (II.16), but in fact includes integration over all neutron energies. Thus, it is not straightforward to say exactly what the "correct" answer is for the $\Sigma_t(x, y)$ that we are asking FBP to construct. Nevertheless, we would expect a viable method to find that Σ_t is different in the region that contains the iron. For comparison the material map is shown in Fig. II.9.

Optically thick, highly scattering problems violate the fundamental assumption behind FBP, namely that the detector signal is proportional to $e^{-\tau}$, where τ is proportional to a line integral of the quantity of interest (such as total cross section or density). This is because scattered particles contribute more to the detector signal than the directly transmitted particles. Collimation of source and detector can help significantly, and we have employed collimation in our application of FBP. However, this is not sufficient for the test problem described above, as Fig. II.8 illustrates. This figure shows the FBP reconstruction of Σ_t in the test object; clearly (and not surprisingly) this is far from the correct solution, and in fact does not suggest that there are any embedded heterogeneities. For comparison we create a smaller version of the same problem, in which the dimensions are reduced by a factor of five. This reduces the optical depth of the shortest path through the water from more than 7 mean free paths to less than 1.5 mean free paths. In this case FBP (with collimated sources and detectors) is able to locate the embedded object, as shown in Fig. II.10 with a comparison to the real distribution shown in Fig. II.11.
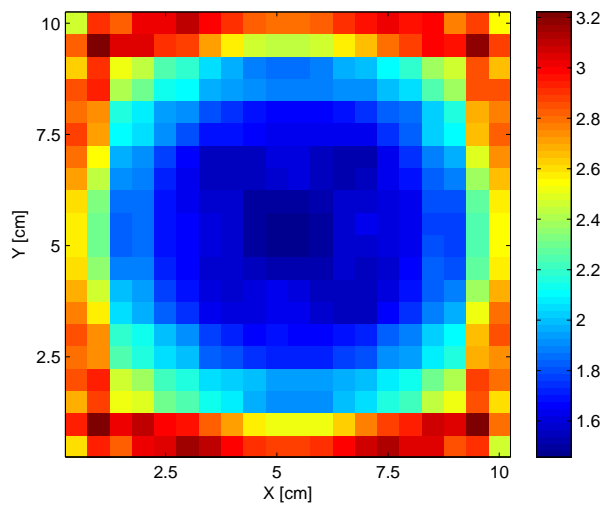
Fig. II.8: Σ_t reconstructed with FBP method for the test problem.
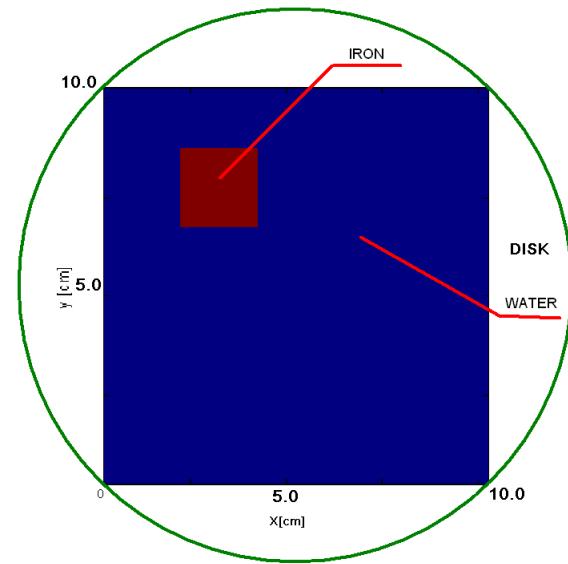
Fig. II.9: Geometry and material configuration of the test problem.
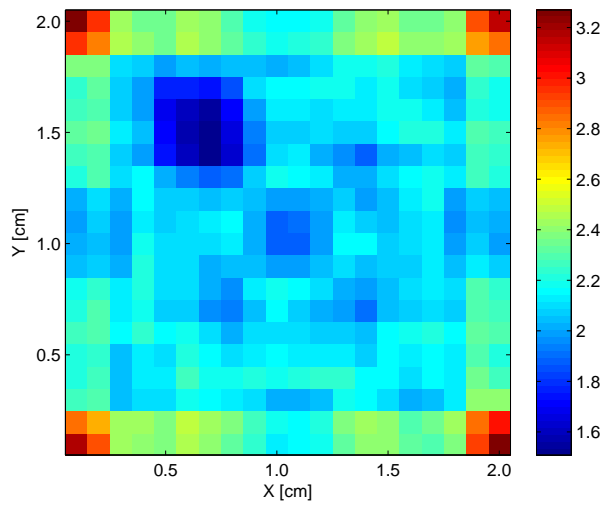
Fig. II.10: Σ_t reconstructed with FBP method for a smaller version of the test problem.
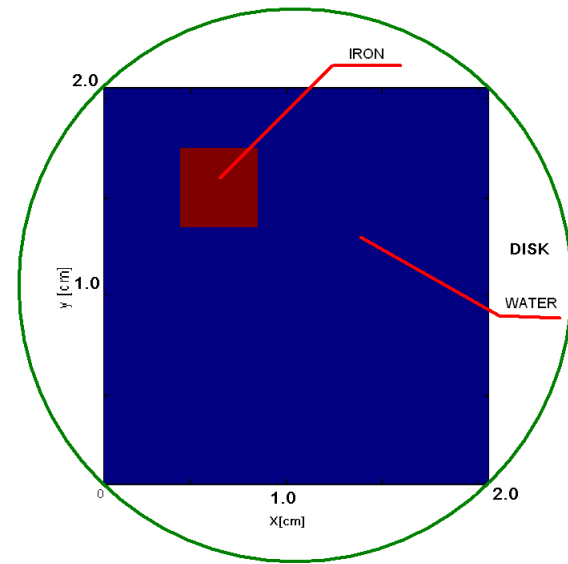
Fig. II.11: Geometry and material configuration of a smaller version of the test problem

The implementation of local tomography becomes straight forward through an observant comparison of Eq. (II.12) with Eq. (II.13) and Eq. (II.14). With back-projection operation on $H_t \frac{\partial P_\theta(t)}{\partial t}$, we recover the density function f. Therefore it's natural to conclude that if we have a desire to recover the function $\Lambda^{-1}f$ and Λf, we only need to operate back-projection on $P_\theta(t)$ and $-\Delta P_\theta(t)$ respectively. However, there's an alternative approach to recover Λf, which is described in Eq. (II.15). Following the logic in Eq. (II.15), we could save the energy that would be required to compute $-\Delta P_\theta(t)$ directly. Instead, we first compute the Fourier transform of projection (i.e. $S_\theta(\omega)$), and then multiply it with $|\omega|^2$ which works as a filter here, and in the last step we operate on the product with an inverse Fourier transform to obtain $-\Delta P_\theta(t)$. Then we operate back projection on $-\Delta P_\theta(t)$ to obtain Λf. The whole theory of this alternative approach is buried in Eq. (II.15). This alternative may look like more complicated in the computation but it is in fact simpler in the implementation, because it takes the advantage of normal tomography algorithms. The only thing that changes between them is that the filter applied to the filtration projection switches from $|\omega|$ to $|\omega|^2$.

We perform local tomography to the test problem with the small modification to the MATLAB utilities that is described in the preceding paragraphs. The image of derivatives of the density function (Λf) is reconstructed and the material interface information deduced from Λf is inferred. The results of the test problem with 10cm $\times$ 10cm in dimension are illustrated in Fig. II.12.

The left picture in Fig. II.12 is Λf tomogram reconstructed with the local tomography algorithm. In this picture the interface between water and air are strongly highlighted; however the interface between the iron inclusion and the water is hardly discerned. This is due to the same reason as we find in the normal tomogram: the object is so thick and highly scattering that the scattering component makes significant contribution to transmitted projections, even with collimation. This violates the underlying basis of line integral rule, so the results from local tomography could

(a) Property image reconstructed by local tomography   (b) Material interface inferred from local image
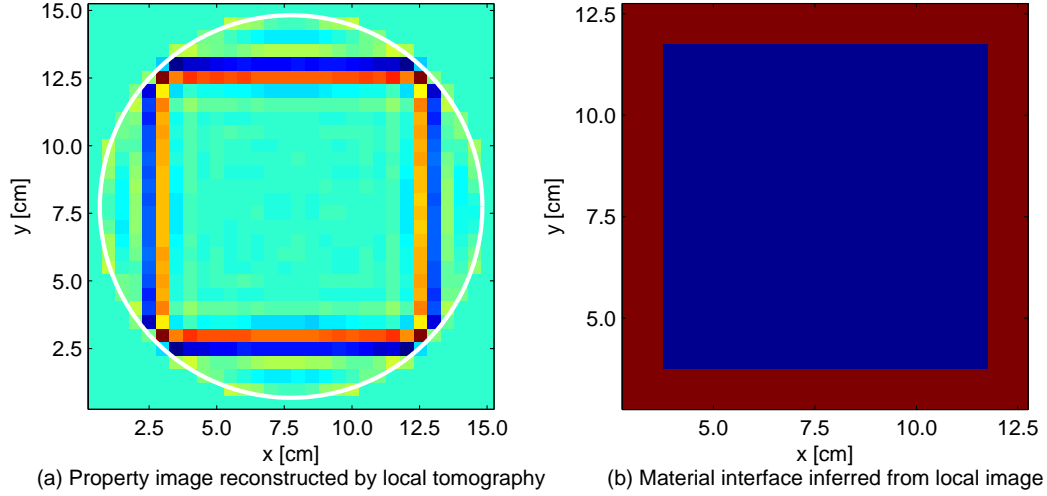
Fig. II.12: Local tomography for the test problem. Left: Reconstruction image of f ; Right: Material interface indicated by information provided in the left image for the test problem.

not provide us anything valuable. This conclusion is further proved in the right picture in Fig. II.12 which is anticipated to identify the interface information within the object by utilizing the information in the left reconstructed image. This is also the motivation that we investigate local tomography in the research. The criterion we apply to determine the interface based on the gradients calculation of the quantities in the left image, i.e. we assume $g = \Lambda f$, and let

$$h = \left| \frac{\partial g}{\partial x} \right| + \left| \frac{\partial g}{\partial y} \right|,$$

then any cells with $h > \frac{1}{2} h_{mean}$ will be recognized as boundary cells. The theory behind the criterion is that theΛf function normally will have a very sharp slope in boundary areas. Unfortunately in the right picture of Fig. II.12, this algorithm does not find any interface in the boundary between water and inclusion which implies the failure of this method.

As we have done previously in the normal tomogram experiment, we also applied local tomography to the smaller version of the same problem, in which the dimensions

are 2cm $\times$ 2cm in x and y coordinates. The same criterion is applied to find the interface area. The Λf tomogram and the interface information inferred from it are illustrated in Fig. II.13. In this case, the left tomogram is able to locate the inclusion boundaries and the interface area in the object is recognized by our algorithm and very close to the white box which is the accurate interface boundary.

(a) Property image reconstructed by local tomography　(b) Material interface inferred from local image
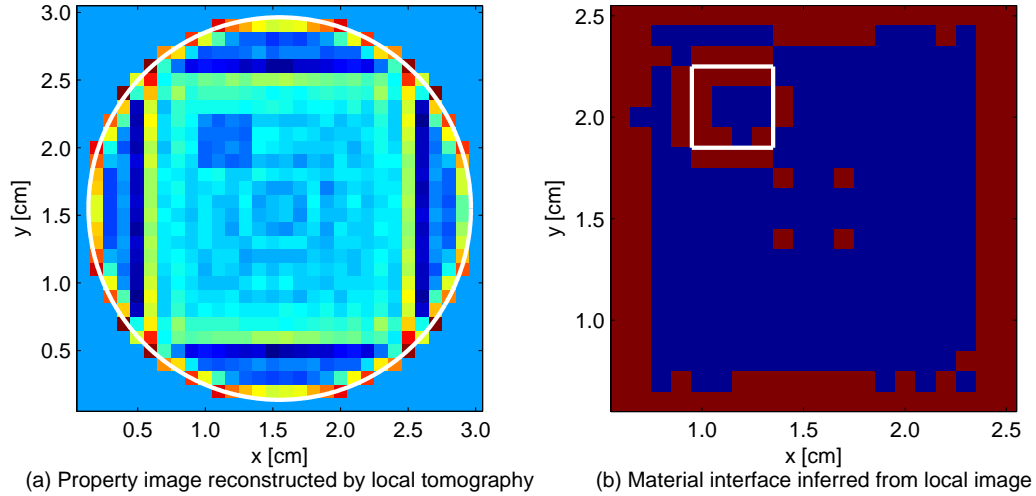
Fig. II.13: Local tomography for a smaller version of test problem. Left: Reconstruction image of Λf; Right: Material interface indicated by information provided in the left image for a smaller version of the test problem. (The white box shows the correct location of the interface.)

II.F   Summary of Chapter II

In this chapter we have discussed the FBP based analytic tomography method and applied it to a test problem that is optically thick and consists of highly scattering materials. The results we obtained from our experiment demonstrate that the analytic tomography method is not a workable approach to address such problems even with collimated source and detectors applied. This is due to the fact that the

basic assumption underlying line-integral methods is violated when the scattering component significantly contributes to the transmitted projections.

The local tomography method was also investigated and applied to the test problem to explore the efficiency and advantages of this method in identifying the material interfaces within the object. However, due to the same reason it fails to achieve the goal in the thick problem with highly scattering medium as well. This conclusion may be generalized to all the FBP based tomography methods. For thick problem undergoing many highly scatterings, we must turn to other methodologies such as iterative based optimization methods. These are the topics we present in the rest of this dissertation.

CHAPTER III

GRADIENT-BASED DETERMINISTIC OPTIMIZATION

III.A   Introduction

Beginning with this chapter, we pose our tomography problem as an optimization problem with a goal to minimize a pre-defined multi-variable objective function. Contrasting to the analytic methodology that we discussed in Chapter II, the dominant approaches in the minimization category are iterative-based reconstruction methods. The important ingredients in these methods are an efficient numerical method to solve the forward model and an efficient inverse model to search for the optimal values. We focus on deterministic optimization in this chapter and address stochastic optimization in next chapter in the course of our development the general tomography method (which involves both deterministic and stochastic components).

Recall that the purpose of the research is to infer material properties inside an object based upon detection and analysis of radiation emerging from the object under investigation. This goal is relatively simple to achieve under the following conditions:

- Mono-directional beams of radiation can be sent into the object,

- Emerging intensity can be detected on the other side with high spatial (and perhaps directional) resolution,

- Radiation has low probability of scattering within the object, and

- Different internal materials have different attenuation coefficients (different total cross sections).

We assume that if everything about the object (material distributions) and any incident radiation is known, a forward model (i.e., solution of the transport equation) could accurately predict the measurements obtained by peripheral detectors. We further assume that detector measurements are given. In practice these would come

from physical detection systems, but during the testing phase of a method they may be simulated by Monte-Carlo or other simulation. Then we pose an optimization-based problem to determine the material distributions that minimize some measure of the difference between predicted and measured results. This measure, called the objective function (it is also referred to as cost function, misfit function, least-squared function, chi squared function etc. in other lectures), could for example be the sum of the squared relative difference between predictions and measures:

$$\Phi = \frac{\frac{1}{2}\sum_{i=1}^{N}(P_i - M_i)^2}{\frac{1}{2}\sum_{i=1}^{N}(M_i)^2}, \tag{III.1}$$

where Φ denotes the objective function, N is the total number of the detectors in the system, P and M are the predicted and measured values respectively. In our current model, M is obtained from the transport calculation in the mathematical model with accurate material properties. The schematic of the problem is depicted in Fig. I.3. The task of the iterative reconstruction method is to design an inverse iteration scheme that finds material properties that reduce the objective function to a fairly small minimum. During each iteration a forward calculation is performed using the latest iteration of material properties, yielding new predicted values and thus a new objective function.

The problem is therefore posed as minimization of the objective function with respect to the material properties within the unknown object. To solve this optimization problem, a forward model capable of calculating the detector responses (both transmitted image and scattered image) for the beam passing through a known object is needed. In addition to this forward model an inverse model is needed in order to create a new "guess" of the object structure (essentially the cross section sets defining the object) after each new objective function is calculated. The forward model can then be repeated using the more accurate guess. These iterations would

continue until the calculated detection rates matched the measured detection rates to within some tolerance (i.e., an objective function is minimized).

Our research work in deterministic optimization follows the work of Scipolo [54], who developed a transport solver (i.e. forward model) using the step characteristic (SC) spatial discretization method to provide reasonably accurate forward transport calculations. Following the work of Klose et al. [36, 37], Scipolo included logic in the forward code to calculate not only the predicted detector readings but also the derivative of the objective function with respect to each unknown material property (cross section). Collectively these derivatives form the gradient of the objective function. Scipolo's inverse model is built with the steepest-descent updating scheme, which of course relies on knowledge of the gradient of the objective function. Scipolo has gained some success in the application of his method to neutron tomography.

For the deterministic component of our method we follow the same basic strategies of Klose et al. [36, 37] and Scipolo [54], but we have implemented several improvements to the approach. We first allow illumination of the object from all four sides of a rectangular object in 2D, with each illumination producing a set of measurements. All four sets are included in the sum that defines the objective function. To increase efficiency we apply a Krylov subspace iterative technique that speeds up each forward calculation. In addition, we employ the nonlinear conjugate gradient (CG) [56] updating scheme as the heart of our search procedure and integrate Brent's method [57] into the associated line-search algorithm. The most striking aspect we improve in this stage is that we perform a variable change to impose non-negativity constraints on cross sections; this is described later in this chapter and in a forthcoming publication [55].

In the following sections of this chapter, we present the essential components of our deterministic optimization method with emphasis on the improvements we introduce in our implementation.

III.B   Multi-beams Incorporation

The uniqueness of the inverse problem is discussed in Boyd [10]. We have encountered ill-conditioning in our inverse problems even in the case of very simple configuration such as only 4 cells in the object. In these cases we may end with a solution that is far from the correct answer but gives a very small objective function. Such ill-conditioning could be mitigated if we can illuminate the object with beams from all of its surfaces. The quality of the reconstruction could be improved by an increase in the number of sources and detectors, or sometimes with smaller mesh sizes, but these tactics are not always practical [35]. In this section we discuss our techniques and implementation of multiple beams, which we use to improve conditioning.

Since the shape of the object in our problem is rectangular (see Fig. I.3, we light the object with beams incident from 4 directions, each of them on one edge of the object. In the simulated experiment, we accomplished this by rotating the object about its center axis and leave the beam and detectors invariant. Then we have to make the transport solver to run four times to collect all the exiting radiation which works as predicted radiation for each forward calculation. We also have to prepare four groups of experiment measurements. This produces four objective functions:

$$\Phi_1 = \frac{1}{2} \sum_{i=1}^{N} (M_{1i} - P_{1i})^2,$$

$$\Phi_2 = \frac{1}{2} \sum_{i=1}^{N} (M_{2i} - P_{2i})^2,$$

$$\Phi_3 = \frac{1}{2} \sum_{i=1}^{N} (M_{3i} - P_{3i})^2,$$

$$\Phi_4 = \frac{1}{2} \sum_{i=1}^{N} (M_{4i} - P_{4i})^2.$$

We sum them and define the new objective function as below:

$$\Phi = \frac{\Phi_1 + \Phi_2 + \Phi_3 + \Phi_4}{\frac{1}{2}\sum_{j=1}^{4}\sum_{i=1}^{N}(M_{ji})^2} \qquad \text{(III.2)}$$

The objective function has the same form of the old one in Eq. (III.1) except it has four groups of misfit functions, and it is normalized to the total sum of the four groups of measurements.

In deterministic optimization stage, the inverse model we adopted is a gradient-based iterative scheme. Therefore if we change the form of the objective function, we also need to be careful of the gradient calculation term for the objective. It is modified as the following: For the property in a specific cell i, we have the expression for the gradient with the relationship to the old gradient values

$$\frac{\partial \Phi}{\partial \sigma_i} = \frac{1}{\frac{1}{2}\sum_{j=1}^{4}\sum_{i=1}^{N}(M_{ji})^2}\left(\frac{\partial \Phi_1}{\partial \sigma_i} + \frac{\partial \Phi_2}{\partial \sigma_i} + \frac{\partial \Phi_3}{\partial \sigma_i} + \frac{\partial \Phi_4}{\partial \sigma_i}\right). \qquad \text{(III.3)}$$

Note that the gradient calculation must be performed four times, once per forward calculation, to obtain the final gradient with respective to σ_i as illustrated in Eq. (III.3).

Our multi-beam procedure is described below:

Input 4 groups of measurements (m1, m2, m3, m4)

Input initial guess for cross sections

Search loop begins

    Forward calculation to obtain Φ_1

    Evaluate Φ_1 by calling measurements m1

    Gradient calculation to obtain $\dfrac{\partial \Phi_1}{\partial \sigma_i}$

    Rotate cross sections distribution

    Same way to obtain $\Phi_2, \dfrac{\partial \Phi_2}{\partial \sigma_i}; \Phi_3, \dfrac{\partial \Phi_3}{\partial \sigma_i}; \Phi_4, \dfrac{\partial \Phi_4}{\partial \sigma_i}$

    Calculate Φ [Eq. (III.2)]

    Calculate $\dfrac{\partial \Phi}{\partial \sigma_i}$ [Eq. (III.3)]

CG/SD updating procedure begins

      Line search to find α - here each objective evaluation needs to run forward transport solver 4 times.

      Cross sections updating - here the dimension of updating variables will be the same as before.

CG/SD updating procedure ends

If the minimum value obtained, output solutions and exit

If not, continue searching

Search loop ends

III.C   Transport Forward Model and Accelerating Iterative Techniques

Our forward model is illustrated with a simple one-group version of the neutron transport equation for a non-multiplying material with linearly anisotropic scattering:

$$\underline{\Omega} \cdot \underline{\nabla} \psi(\underline{r}, \underline{\Omega}, t) + \Sigma_t(\underline{r})\psi(\underline{r}, \underline{\Omega}, t) =$$
$$\frac{1}{4\pi}\Sigma_s(\underline{r})\left[\phi(\underline{r}, t) + 3g\underline{\Omega} \cdot \underline{J}(\underline{r}, t)\right] + S_{ext}(\underline{r}, \underline{\Omega}, t). \tag{III.4}$$

Here Σ_t and Σ_s are macroscopic total and scattering cross sections and g denotes the averaging scattering cosine. These three parameters are properties of the material in the object being studied. The task of a "forward" transport problem is to solve for the angular flux ψ if the material properties (Σ_t, Σ_s, g) are provided as a function of position in the spatial domain.

Σ_t and Σ_s may be easy to catch up, here we give a further introduction to the property of neutron linear scattering anisotropy factor, which is also referred to as neutron scattering asymmetry factor. It is often denoted by g or $\overline{\mu_0}$ in some nuclear-reactor texts [11, 73]. It is the average cosine of the scattering angle of a single-scattering event, which is used to characterize the angular distribution of scattering. See the simple Fig. III.1 below:
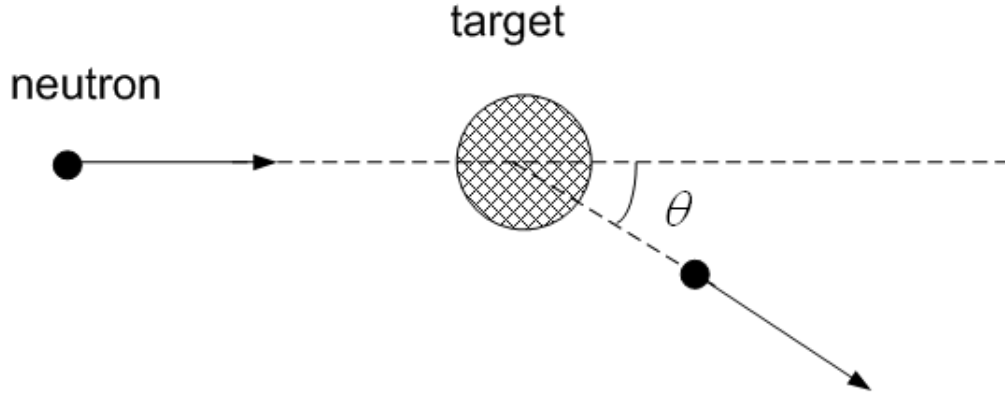
Fig. III.1: Neutron scatters through angle θ, called the "scattering angle", after colliding with a nucleus.

If we define $\mu_0 = \cos\theta$, we have

$$g = \overline{\mu_0} = \frac{\int_{-1}^{1} \mu_0 \sigma_s(\mu_0) d\mu_0}{\int_{-1}^{1} \sigma_s(\mu_0) d\mu_0},$$

where when

$$
\begin{cases}
g = 1, & \text{particles scattering is forward peaked} \\
g = 0, & \text{particles scattering is isotropic} \\
g = -1, & \text{particles scattering is backward peaked}
\end{cases}
.
$$

Different nuclear isotope has different but specific $\sigma_s(\mu_0)$ distribution in neutron-target interaction. It also changes with incident neutron energy, sometimes dramatically. All these will synthesize to determine a specific g. In the relatively common case of isotropic scattering in the center-of-mass reference frame, we can show that the lab-frame anisotropy factor is $g \approx \frac{2}{3A}$, where A is the atomic mass number of the scattering nucleus [73].

The general neutron transport equation (which is more complicated than Eq. (III.4) is a linear form of the Boltzmann equation, developed more than one century ago for

the study of the kinetic theory of gases [11]. It describes the evolution of a particle distribution function in an infinitesimally small six-dimensional phase-space (space, energy, direction) volume. The analytic solution of this equation is known only for very highly idealized cases often concerning semi-infinite mediums [74]. The solution of the equation for more common but complicated problems is obtained through the use of numerical approximations and computational calculations.

The numerical solutions to the transport equation are divided into stochastic (Monte Carlo) and deterministic. The Monte Carlo method treats all the events that can occur to a particle in terms of probability functions. It tracks a representative sample of particles from "birth" until "termination" (for many reasons such as absorption, leaking) and thus makes the history of each sampled particle [75]. By using a large number of histories it estimates the average particle behavior. This method is in general computationally more expensive than deterministic methods. The advantage is the possibility of simulating complex geometrical systems and physically complex histories.

Deterministic methods solve the transport equation by discretization of the phase space volume in order to reduce the transport equation to a set of simpler algebraic equations. The discretization into energy groups leads to a multi-group transport equation. The transport equation can be expressed as an integro-differential equation or as an integral equation. The choice of spatial and angular discretization depends on the form of the equation. The form used for this project is the steady-state, one-group integro-differential form that involves an angular integral and a first-order spatial derivative. Other forms are described elsewhere [12, 74]. Different angular discretization can be applied o simplify the angular integral into a set of differential equations. We choose to treat the angular dependence with a discrete ordinate

(S_N) method in this work. The S_N methods approximates the angular integral as a quadrature summation:

$$\begin{cases} \phi(\underline{r}) = \sum_m w_m \psi(\underline{r}, \Omega_m) \\ J(\underline{r}) = \sum_m w_m \Omega_m \psi(\underline{r}, \Omega_m) \end{cases}.$$

If we now recognize that we need to solve Eq. (III.4) only for each direction in the quadrature set, we see that the resulting set of equations is a coupled system of partial differential equations in space. Each of this is spatially discretized to generate a set of algebraic equations.

In the present work, we consider an X-Y two-dimensional problem, thus the solution of the forward neutron transport model needs to be derived for the two dimensional case. The detailed procedure for the forward transport solver development can be found in [54] chapter II. Here we only point out that the method chosen for the spatial discretization in our work is the Step Characteristic (SC) method. It has been developed first by Lathrop [76]. Like every other characteristic method the SC method transforms the Sn equation into a one-dimensional equation by rotating the axis of the coordinate system along the direction of motion (the characteristic line). Given the value of the angular flux at a point along the characteristic line and known source term the characteristic equation can be analytically solved for the angular flux everywhere along the line.

In most cases, transport solver requires a long time to compute a solution. We speed the forward calculation by applying some acceleration techniques to the solver and implement them into the forward model. For simplicity in illustrating these techniques, we consider Eq. (III.4) in the slab-geometry case with isotopic source and isotropic scattering:

$$\mu \frac{\partial \psi(x, \mu)}{\partial x} + \Sigma_t(x)\psi(x, \mu) = \frac{\Sigma_s(x)}{2}\phi(x) + \frac{Q_e(x)}{2}, \tag{III.5}$$

where

$$\phi(x) = \int_{-1}^{1} \psi(x,\mu)d\mu. \tag{III.6}$$

Mathematically, this is an inhomogeneous equation. In general, Eq. (III.5) would always have a stable solution provided that $\Sigma_s \leq \Sigma_t$. To write Eq. (III.5) in operator forms, we define

$$L \equiv \mu\frac{\partial}{\partial x} + \Sigma_t(x) = \text{``leakage plus collision'' operator,}$$

$$S \equiv \frac{\Sigma_s(x)}{2} = \text{scattering operator,}$$

$$q(x) = \frac{Q_e(x)}{2}.$$

Then Eq. (III.5) may be written into

$$L\psi = S\phi + q. \tag{III.7}$$

For general purpose, Eq. (III.7) may be written as a form of

$$Ax = b. \tag{III.8}$$

In many cases, when we attempt to solve the linear equation in Eq. (III.8) using an iterative method, first we partition A into

$$A = D - L - U, \tag{III.9}$$

where $D = \text{diag}(A)$, L is the negative of the strictly lower triangular part of A, and U is the negative of the strictly upper triangular part of A. We can summarize some basic iterative methods in terms of these key matrices as follows:

- **Jacobi:**

$$Dx^{(k+1)} = (L + U)x^{(k)} + b. \tag{III.10}$$

- **Gauss-Seidel:**

$$(D - L)x^{(k+1)} = Ux^{(k)} + b. \tag{III.11}$$

- **SOR (successive overrelaxation):**

$$D - \omega L)x^{(k+1)} = \omega(Ux^{(k)} + b) + (1 - \omega)Dx^{(k)}. \qquad \text{(III.12)}$$

- **SSOR (symmetric successive overrelaxation):**

$$\begin{cases} (D - \omega L)x^{(k+\frac{1}{2})} = \omega(Ux^{(k)} + b) + (1 - \omega)Dx^{(k)} \\ (D - \omega U)x^{(k+1)} = \omega(Lx^{(k+\frac{1}{2})} + b) + (1 - \omega)Dx^{(k+\frac{1}{2})} \end{cases}. \qquad \text{(III.13)}$$

Each iteration of the **SSOR** method consists of first a **forward SOR** iteration that computes the unknowns in a certain order and then a **backward SOR** *sweep* that solves for them in the opposite order. Choosing the *best* relaxation parameters for the SOR and SSOR methods is an intriguing question with rather complicated answers.

- **Richardson:**

$$x^{(k+1)} = (I - A)x^{(k)} + b. \qquad \text{(III.14)}$$

- **Preconditioned Richardson:**

$$x^{(k+1)} = (I - PA)x^{(k)} + Pb. \qquad \text{(III.15)}$$

Here the preconditioner is P.

In some references [77], these iteration methods described above are noted as stationary iterative methods, because the matrices used for updating variables are kept constant during the iterative procedure. Nonstationary iterative methods, unlike stationary ones, involve information that changes at each iteration in the computation. Typically, constants are computed by taking inner products of residuals or other vectors arising from the iterative method. Numerical experiments show that the nonstationary iterative methods accelerate the convergence the solutions to transport model and in most of cases work as more efficient iterative scheme in the forward calculation. We present some of these iterative techniques in this section and apply them to the forward calculation in this research.

In neutron transport category, within an energy group the source iteration (SI) scheme would be written as follows:

$$\mu \frac{\partial \psi^{(l+1)}(x,\mu)}{\partial x} + \Sigma_t(x)\psi^{(l+1)}(x,\mu) = \frac{\Sigma_s(x)}{2}\phi^{(l)}(x) + \frac{Q_e(x)}{2},$$

where

$$\phi^{(l)}(x) = \int_{-1}^{1} \psi^{(l)}(x,\mu)d\mu.$$

If represent it with operator form as Eq. (III.7), it is

$$L\psi^{(l+1)} = S\phi^{(l)} + q.$$

Therefore the iteration form derived here is solved by the method of iteration on the scattering term. In the work prior to this research [54], the forward calculation is indeed developed based on source iteration. However, in some physical scenario, e.g. the problem with optically thick geometry (which means $\Delta x \Sigma_t$ is large) and highly scattering physical material (which means $c = \Sigma_s/\Sigma_t$ is close to unity), the source iteration technique becomes very inefficient and the solution hardly converges. As a result, more rapidly convergent iterative methods are required [12, 78]. In fact, this is one of most active research topics in transport theory and application.

The solution to transport equation is the scalar flux ϕ. With the Richardson updating scheme Eq. (III.14), we may write it as

$$\phi^{(k+1)} = (I - A)\phi^{(k)} + b. \tag{III.16}$$

It is easy to show that source iteration satisfies Eq. (III.14) with the following definition of A:

$$A = I - \int_{-1}^{1} \left(L^{-1}S\right) d\mu.$$

So we would have

$$A\phi^{(k)} = \phi^{(k)} - \phi^{(k+1)} + b. \tag{III.17}$$

The equation we end here is very advantageous; it indicates that if we find $\phi^{(k+1)}$ by performing a transport sweep with $\Phi^{(k)}$ used in the scattering source, we will

be able to evaluate the matrix vector multiplication $A\phi^{(k)}$ with simple subtraction and summation operation. And we know in computational methods to transport equation, the transport "sweep" process gives us the capability to calculate $\phi^{(k+1)}$ once the previous (initial) flux $\phi^{(k)}$ is given. Once we can use transport sweeps to implement Krylov-subspace based acceleration techniques for transport solver, because all those techniques require the operation of matrix vector multiplication. We have done this in our forward transport solver. Our quantitative results show that the forward calculation has dramatically speeded up and the computation time is greatly reduced. This conclusion is consistent with results obtained by previous authors [78–81]. The detailed method for some classic Krylov-subspace based accelerating iterative scheme, such as Bi-CGSTAB [82], CGS [83], GMRES, etc., are presented in Appendix B.

III.D   Nonlinear Conjugate Gradient Optimization

III.D.1   Inverse model

The inverse model we apply in the deterministic optimization method is a gradient based iterative scheme, in which we make use of nonlinear conjugate gradient updating scheme for the minimization of the objective function. We start with problem with steepest descent (SD) method [54, 84] in which the search direction in each updating iterate is the direction opposite to the gradient of the objective function. SD method normally converges very slowly especially when the optimized value is getting close to the right solution. The conjugate gradient (CG) method is slightly different from the steepest descent [56]. At every step instead of moving along a direction orthogonal to the previous one the CG moves along an A-orthogonal direction (A is the matrix that defines the quadratic dependence of the function with respect to all the variables). From a more understandable point of view, the CG method tries to minimize the residual instead of the objective function itself. In

order to achieve the goal, the new direction in CG of every iterate is calculated with a linear interpolation between the old direction and the new gradient.

We present the pseudo code for nonlinear **conjugate gradient** (CG) algorithm as below:

Variables initialize $\mathbf{x}^{(1)}$, *where* $x = \{\Sigma_t, \Sigma_s, g\}$

Set the initial search direction $\mathbf{d}^{(1)} = \mathbf{r}^{(1)}$, *where* $\mathbf{r}^{(1)} \equiv -\nabla\Phi\left(\mathbf{x}^{(1)}\right)$

Define termination tolerance ε

Set iteration counter $k = 0$

Loop

Perform line search to find $\alpha_{\min}$ *that minimizes* $\Phi(\mathbf{x}^{(k)} + \alpha\mathbf{d}^{(k)})$

$\mathbf{x}^{(k+1)} = \mathbf{x}^{(k)} + \alpha_{\min}\mathbf{d}^{(k)}$

$\mathbf{r}^{(k+1)} \equiv -\nabla\Phi\left(\mathbf{x}^{(k+1)}\right)$

$\mathbf{d}^{(k+1)} = \mathbf{r}^{(k+1)} + \beta_k\mathbf{d}^{(k)}$ *(we will elaborate the choice of* β_k *later.)*

$k = k + 1$

Until $\left\|\nabla\Phi\left(\mathbf{x}^{(k)}\right)\right\| < \varepsilon$

For the contrasting purpose, we also present the pseudo code for **steepest descent** (SD) optimization algorithm, it differs from the CG algorithm only within the loop part:

Loop

Perform line search to find $\alpha_{\min}$ *that minimizes* $\Phi(\mathbf{x}^{(k)} + \alpha\mathbf{r}^{(k)})$

$\mathbf{x}^{(k+1)} = \mathbf{x}^{(k)} + \alpha_{\min}\mathbf{r}^{(k)}$

$\mathbf{r}^{(k+1)} \equiv -\nabla\Phi\left(\mathbf{x}^{(k+1)}\right)$

$k = k + 1$

Until $\left\|\nabla\Phi\left(\mathbf{x}^{(k)}\right)\right\| < \varepsilon$

The method of Steepest Descent is simple, easy to apply, and each iteration is fast. It also very stable; if the minimum points exist, the method is guaranteed to locate it eventually. But, even with all these positive characteristics, the method

has one very important drawback: it generally has slow convergence. For badly scaled systems; i.e. if the eigen-values of the Hessian matrix at the solution point are different by several orders of magnitude, the method could take an extremely large number of iterations before locating a minimum point. It starts out with a reasonable convergence, but the progress gets slower and slower as the minimum is approached to the exact solution, especially in the case of a quadratic function with a long, narrow valley. The method may converge fast for such badly scaled systems, but is then very much dependent on a good choice of starting point. In other words, the Steepest Descent method can be used where one has an indication of where the minimum is, but is generally considered to be a poor choice for any optimization problem. It is mostly only used in conjunction with other optimizing methods.

III.D.2 Problems associated with nonlinear CG method

In our initial application of the nonlinear steepest descent/conjugated gradient optimization, we encountered some difficulties in the procedure. Some of them we have addressed successfully and some of them still can cause problems in certain situations. We summarize them as follows.

1. **Starting of SD or CG**

   In general, if there exists a rough estimate of the value of x , it should be used as the starting value x_0 . If not, set $x_0 = 0$; either SD or CG will eventually converge when used to solve linear systems. However, Nonlinear minimization is trickier, because there may be several local minima, and the choice of starting point will determine which minimum the procedure converges to, or whether it will converge at all. The closer the starting point is to the solution, the more similar the convergence of nonlinear CG is to that of linear CG.

2. **Loss of conjugacy**

   In linear case, conjugacy means A-orthogonal, but in nonlinear cases, it means

f''-orthogonal where f is the objective function [56]. The less similar f is to a quadratic function, the more quickly the search directions lose conjugacy. (Because if f is a quadratic form, then f'' is just the familiar matrix A.) However, in the general (nonlinear) case, the meaning of "conjugacy" keeps changing, because f'' varies with updating variable. The more quickly f'' varies with the variable, the more quickly the search directions lose conjugacy. On the other hand, the closer the variable is to the right solution, the less f'' varies from iteration to iteration. The approach we apply to avoid the loss of conjugacy is restart CG as SD at a certain step if the code detects that conjugacy may possibly be lost in that step.

3. **Restart CG (downhill search direction protected)**

An inexact line search may lead to the construction of a search direction that is not a descent direction. A common solution to this problem is as below, since

$$\mathbf{d}^{(k+1)} = \mathbf{r}^{(k+1)} + \beta_k \mathbf{d}^{(k)}, \tag{III.18}$$

before doing that, test the value of $\left(\mathbf{r}^{(k+1)}, \mathbf{d}^{(k)}\right)$, if the line search is exact, then this value should equal to zero, but if $\left(\mathbf{r}^{(k+1)}, \mathbf{d}^{(k)}\right) < 0$, we will restart the CG, which means set

$$\beta_k = 0 \quad i.e. \quad \mathbf{d}^{(k+1)} = \mathbf{r}^{(k+1)} \tag{III.19}$$

and thus we use the SD direction as the next search direction.

4. **Different Choice of β_k**

Three of the best known formulas for β_k are titled Fletcher-Reeves (FR), Polak-Ribière (PR), and Hestenes-Stiefel (HS) [also known as Sorenson-Wolfe (SW)] after their developers. They are given by the following formulas.

- Fletcher-Reeves (FR) formula

$$\beta_k^{FR} = \frac{\left(\mathbf{r}^{(k+1)}, \mathbf{r}^{(k+1)}\right)}{\left(\mathbf{r}^{(k)}, \mathbf{r}^{(k)}\right)}, \tag{III.20}$$

- Polak-Ribière (PR) formula

$$\beta_k^{PR} = \frac{\left(\mathbf{r}^{(k+1)}, \mathbf{r}^{(k+1)} - \mathbf{r}^{(k)}\right)}{\left(\mathbf{r}^{(k)}, \mathbf{r}^{(k)}\right)}, \tag{III.21}$$

- Hestenes-Stiefel (HS) formula

$$\beta_k^{HS} = \frac{\left(-\mathbf{r}^{(k+1)}, \mathbf{r}^{(k+1)} - \mathbf{r}^{(k)}\right)}{\left(\mathbf{d}^{(k)}, \mathbf{r}^{(k+1)} - \mathbf{r}^{(k)}\right)}. \tag{III.22}$$

These formulas are equivalent for a quadratic function, but for nonlinear optimization the preferred formula is a matter of heuristics or taste. Interestingly, the last two formulas are generally preferred in practice, though the first has better theoretical global convergence properties. In fact, very recent research has focused on combining these practical and theoretical properties for construction of more efficient schemes. A popular choice is

$$\beta_k = \max\left\{0, \beta_k^{PR}\right\}, \tag{III.23}$$

which provides a direction reset automatically. Eq. (III.23) sometimes is referred to as Polak-Ribière-Polyar formula.

5. **CG and SD hybrid**

   Because CG can only generate n vectors in an n-dimensional space, it makes sense to restart CG every n iterations (restart CG means go SD method for one iteration), especially if n is small. Numerical experience shows this is a very effective way to get more minimum values in nonlinear optimization problems.

6. **Stopping of SD or CG**

   When Steepest Descent or CG reaches the minimum point, the residual becomes zero. Because of accumulated roundoff error the recursive formulation of the residual may yield a false zero residual; also, usually one wishes to stop before convergence is perfect. It is customary to stop when the norm of the residual falls below a specified value, often, this value is some small fraction of the initial residual:

$$\left\|\mathbf{r}^{(k)}\right\| < \varepsilon \left\|\mathbf{r}^{(0)}\right\| \tag{III.24}$$

III.D.3   Line search methods

Another important subject related to nonlinear conjugate gradient optimization scheme is the line search (also referred to as 1-D search) method, which is the approach to find α to minimize the objective function $f(\mathbf{x}^{(k)} + \alpha \mathbf{d}^{(k)})$ along the search direction $\mathbf{d}^{(k)}$. Here the $\mathbf{d}^{(k)}$ could be taken as the line search direction, and α could be taken as how far to go (step size) along the direction to obtain the minimum value in the direction.

When using either Newton-Raphson or Secant method to line search in the conjugated gradient among the nonlinear optimization problems, the searched value should be terminated when it is reasonably close to the exact solution [56]. Demanding too little precision would cause a failure of convergence, but on the other hand demanding too much precision would make the computation unnecessarily slow and gains nothing, because conjugacy will break down quickly anyway if f'' varies much with searched value. Therefore, a quick but inexact line search is often the better policy (for instance, use only a fixed number of Newton-Raphson or Secant method iterations, or even choose some fixed step size in the line as the solution). Unfortunately, inexact line search may lead to the construction of a search direction that is not a descent direction. A common solution is to test for this eventuality (i.e. is $(\mathbf{r}, \mathbf{d})$ nonpositive?), and restart CG to SD if $(\mathbf{r}, \mathbf{d}) \leq 0$.

We note that the line search involves multiple evaluations of the objective function, and each such evaluation requires the solution of a forward transport problem. It is therefore important for the line search to locate the minimum efficiently (that is, with a reasonably small number of function evaluations).

To locate the minimum along the search direction, there are a variety of line search methods to accomplish it but they are all more or less based from Newton's method (quasi-Newton method). They either utilize gradient information or use only function evaluations such as the quadratic fit method. It is often difficult to predict

which of these routines provides the best results for any given problem. In this section we summarize some of the common used line search methods as following:

1. **Newton-Raphson method**

   This method requires the evaluation of the first and second order of derivatives.

2. **Secant method**

   This method requires calculation of the first order of derivative.

3. **Section method: Bisection or Golden section method**

   The section method is a linear search that does not require the calculation of the gradients. It begins by locating an interval in which the minimum of the performance function occurs. This is accomplished by evaluating the performance at a sequence of points, starting at a distance of delta and doubling in distance each step, along the search direction. When the performance increases between two successive iterations, a minimum has been bracketed. The next step is to reduce the size of the interval containing the minimum.

   Bisection method systematically reduces the located bracket interval of uncertainty by function comparison. It evaluates the midpoint of the interval and the performance of the midpoint determines which side of the interval would be discarded. Then each comparison reduces the width of the interval to half of the original one until the interval of uncertainty goes to a width of per-determined tolerance.

   The golden section method, in a little bit different manner, evaluates two new points that are located within the initial interval. The values of the performance at these two points determine a section of the interval that can be discarded, and a new interior point is placed within the new interval. This procedure is continued until the interval of uncertainty is reduced to a width of pre-defined tolerance. Please refer to [85] starting on page 12-16 for a complete description of the golden section method.

4. **Brent's method**

   Brent's method is a linear search that is a hybrid of the golden section search and a quadratic interpolation. Function comparison methods, like the golden section search, have a first-order rate of convergence, while polynomial interpolation methods have an asymptotic rate that is faster than super-linear. On the other hand, the rate of convergence for the golden section search starts when the algorithm is initialized, whereas the asymptotic behavior for the polynomial interpolation methods can take many iterates to become apparent. Brent's method attempts to combine the best features of both approaches. For Brent's method, you begin with the same interval of uncertainty used with the golden section search, but some additional points are computed. A quadratic function is then fitted to these points and the minimum of the quadratic function is computed. If this minimum is within the appropriate interval of uncertainty, it is used in the next stage of the search and a new quadratic approximation is performed. If the minimum falls outside the known interval of uncertainty, then a step of the golden section search is performed. Please refer to [57] for a complete description of this method. This method has the advantage that it does not require computation of the derivative. The derivative computation requires a back propagation through the network, which involves more computation than a forward pass. However, the method can require more performance evaluations than methods that use derivative information.

5. **Hybrid bisection-Cubic interpolation method**

   Like Brent's method, this method is also a hybrid algorithm. It is a combination of bisection and cubic interpolation. For the bisection algorithm, one point is located in the interval of uncertainty, and the function and its derivative are computed. Based on this information, half of the interval of uncertainty is discarded. In the hybrid algorithm, a cubic interpolation of the function is obtained by using the value of the function and its derivative at the two

endpoints. If the minimum of the cubic interpolation falls within the known interval of uncertainty, then it is used to reduce the interval of uncertainty. Otherwise, a step of the bisection algorithm is used. Refer to [9] for a complete description of the hybrid bisection-cubic search. This algorithm does require derivative information, so it performs more computations at each step of the algorithm than the golden section search or Brent's method.

6. **Charalambous method**

   The method of Charalambous was designed to be used in combination with a conjugate gradient algorithm for neural network training. Like the previous two methods, it is a hybrid search. It uses a cubic interpolation together with a type of sectioning. Refer to [86] for a description of Charalambous method. This method is used as the default search for most of the conjugate gradient algorithms because it appears to produce excellent results for many different problems. It does require the computation of the derivatives (back propagation) in addition to the computation of function, but it overcomes this limitation by locating the minimum with fewer steps, at least for some problems.

7. **Backtracking method**

   The backtracking method is best suited to use with the quasi-Newton optimization algorithms. It begins with a step multiplier of 1 and then backtracks until an acceptable reduction in the objective function is obtained. On the first step it uses the value of the function at the current point and a step multiplier of 1. It also uses the value of the derivative of the function at the current point to obtain a quadratic approximation to the function along the search direction. The minimum of the quadratic approximation becomes a tentative optimum point (under certain conditions) and the function at this point is tested. If the function is not sufficiently reduced, a cubic interpolation is obtained and the minimum of the cubic interpolation becomes the new tentative optimum point.

This process is continued until a sufficient reduction in the function is obtained. The backtracking algorithm is described in [87]. Backtracking method is a good candidate for in-exact line search for the quasi-Newton algorithms, however, in conjugate gradient or steepest descent method, the precision of result in line search is instead vital to final solution of the method.

After testing several line search method we listed above, we finally adopted Brent's method to perform the line search in the optimization process in our research. We choose Brent's method due to the following two considerations: (1) The calculation of the gradients of the objective function in our problem is time consuming and second-order derivatives of the objective function would be challenging; (2) We require high level of precision in the line search results as we use the conjugate gradient updating scheme. In the implementation stage, we firstly locate an interval used to bracket the minimum along the search direction. We then employ Brent's method to determine the minimum in the bracketed region by choosing the value between quadratic fit and golden search. Brent's search is in fact a linear search that is a hybrid of the golden section search and a quadratic interpolation. The standard FORTRAN subroutine of this method can be found in the book "Numerical Recipes in Fortran 77", which is available in the website: http://www.library.cornell.edu/nr/).

III.E   Variable Change Technique in Constrained Optimization

Deterministic optimization methods minimize the objective function in Eq. (III.1) by treating the measurements P_i (and thus the objective function) as a function of the macroscopic cross sections of the materials in the object. Let x be the vector of unknowns, so that x_j is a cross section or g factor for some spatial region. The goal is to find the x that minimizes Φ. The procedure is outlined in the work of Klose et

al. [36, 37] as corrected by Scipolo [54]. We present the details of this approach in previous sections, but we note here that updated iterates are produced as follows:

$$x_i^{(k+1)} = x_i^{(k)} + \alpha_{x,step} d_i^{(k)}, \qquad \text{(III.25)}$$

where the update-direction vector, d, depends on several things including the gradient of the objective function:

$$\left\{ d_i^{(k)}, i = 1..N \right\} \text{ depends on } \left\{ \left. \frac{\partial \Phi}{\partial x_j} \right|^{(k)}, \ j = 1..N \right\}. \qquad \text{(III.26)}$$

The components of the objective function's gradients are constructed after a forward calculation for a given iterate using the procedure described by Scipolo [54]. An updated value may be outside the physically meaningful range for the variable. For example, a new cross section may be negative. If this is not corrected, then it may not be possible to perform the next forward calculation, which causes the entire method to fail.

In our problem we perform a variable change to address this issue. The new variables are not constrained; thus our procedure makes the optimization problem appear unconstrained to the minimization method. The important ingredient is a well behaved function for the variable change process. We have found simple functions that appear to work well. For cross sections we use

$$y_j = \log(\Sigma_j) \ \Rightarrow \ \frac{\partial \Phi}{\partial y_j} = \frac{\partial \Phi}{\partial \Sigma_j} \frac{d\Sigma_j}{dy_j} = \frac{\partial \Phi}{\partial \Sigma_j} \Sigma_j \quad .$$

For the anisotropic scattering factor we use

$$y_j = \tan\left(\frac{\pi}{2} g_j\right) \ \Rightarrow \ \frac{\partial \Phi}{\partial y_j} = \frac{\partial \Phi}{\partial g_j} \frac{dg_j}{dy_j} = \frac{\partial \Phi}{\partial g_j} \frac{2}{\pi} \frac{1}{1 + \tan^2\left(\frac{\pi}{2} g_j\right)} \quad .$$

Fig. III.2 shows how the changed variables vary smoothly along the entire real line as the physical variables vary along their allowed ranges. After variable changes, the new updating scheme is

$$y_i^{(k+1)} = y_i^{(k)} + \alpha_{y,step} d_{y,j}^{(k)}. \qquad \text{(III.27)}$$

After this unconstrained update of the transformed variables, it is simple to calculate updated physical variables. As is clear from Fig. III.2, any value of a transformed variable will map to an allowed value of the associated physical variable.

(a) $y = log(\Sigma)$

(b) $y = tan(\frac{\pi g}{2})$
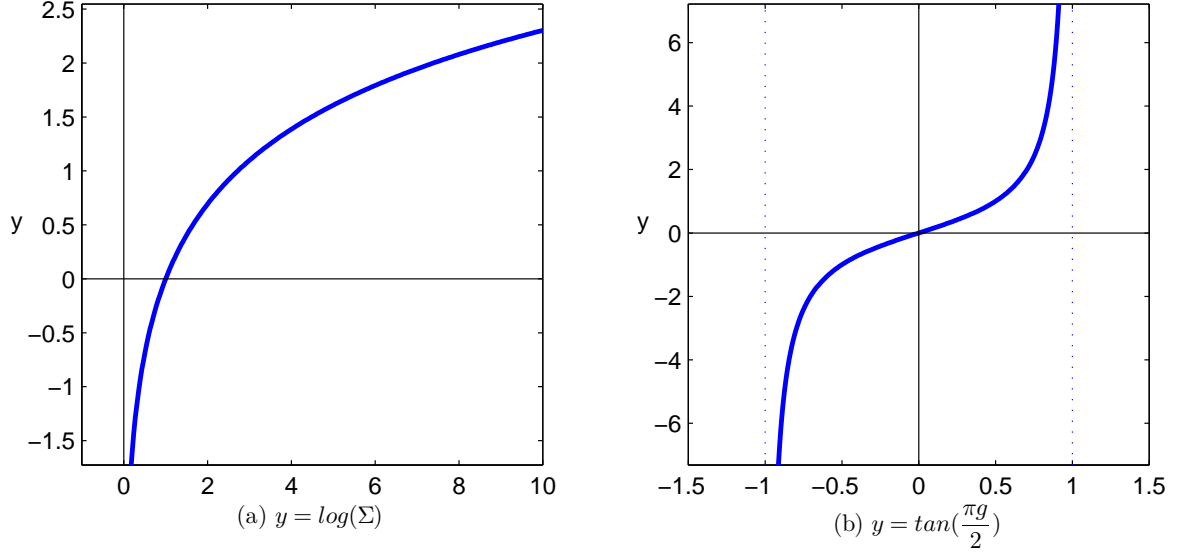
Fig. III.2: Variable change functions. (a) cross sections and (b) average scattering cosine.

Therefore the CG updating scheme with variable change technique incorporated becomes:

Start of iteration loop

Change variable x to y

Perform line search to find $\alpha_{\min}$ *that minimizes* $\Phi(\mathbf{y}^{(k)} + \alpha\mathbf{d}^{(k)})$

$\mathbf{y}^{(k+1)} = \mathbf{y}^{(k)} + \alpha_{\min}\mathbf{d}^{(k)}$

$\mathbf{r}^{(k+1)} \equiv -\nabla\Phi\left(\mathbf{y}^{(k+1)}\right),$ *where* $\nabla\Phi(\mathbf{y}^{(k+1)})$ *is calculated based* $\nabla\Phi(\mathbf{x}^{(k+1)})$

$\mathbf{d}^{(k+1)} = \mathbf{r}^{(k+1)} + \beta_k\mathbf{d}^{(k)}$

$k = k + 1$

Change variable y to x

Until $\left\|\nabla\Phi\left(\mathbf{x}^{(k)}\right)\right\| < \varepsilon$

End of iteration loop

We highlight the different places existed in the new algorithm with contrast to the old one (see page 50), i.e. before the variable being updated, we need to change the variable $\mathbf{x}$ into $\mathbf{y}$ to let the updating scheme being processed in $\mathbf{y}$ domain and after updating we then need to change variable $\mathbf{y}$ back to $\mathbf{x}$ to make the forward calculation being capable to proceed. We describe the variable change technique in more detail in [55].

III.F   Shortcomings in Current Methods

Existing methods for minimizing the objective function in Eq. (III.1) treat the measurements P_i as functionals of the macroscopic cross sections of the materials in an unknown object, which is usually partitioned into spatial cells, each assumed to have uniform material properties. The goal is to find a set of cross sections in each spatial cell such that the objective function Φ is minimized. Mathematically, this involves a very high-dimensional space. The number of dimensions equals the number of spatial cells times the number of cross sections needed to characterize the material in each cell - the total number of unknowns in the problem. Note that each unknown is a continuous variable. Note further the following:

- Dimensionality grows rapidly as the transport model becomes more realistic (in its energy resolution and its treatment of anisotropic scattering). If energy dependence is important, so that many energy groups are needed to accurately treat the problem, the number of dimensions becomes very high indeed, scaling as number of energy groups squared because of group-to-group scattering.

- Each P_i is a complicated nonlinear functional of each unknown cross section.

- While Φ is a continuous function of each unknown cross section, it may have many local minima. This makes it difficult to find a global minimum. Deter-

ministic versions (such as CG based optimization) are particularly susceptible to becoming trapped in local instead of global minima.

- These inverse problems are ill-conditioned: In many cases, there are a wide range of cross section distributions that produce approximately the same objective function.

- Individual stochastic versions (such as Simulated Annealing or Genetic Algorithm) tend to be unable to use valuable information, for example gradients of with respect to the unknowns. As a result, they require enormous numbers of "forward" calculations given high-dimensional spaces of unknowns.

- Cross-section sets are not constrained to be realistic - a cell's set may not correspond to any real material.

We introduce some new ideas in this work that are designed to address these drawbacks. The biggest novelty we apply here is to combine deterministic and stochastic method together for the purpose of leveraging advantages of both sides. We treat the results from the deterministic optimization stage as prior knowledge and use this as input to stochastic optimization procedure. The important aspect in stochastic part is to devise some key dimension reduction techniques to dramatically reduce the computational burden. We will present the details of these new features of the methods in next chapter (Chapter IV).

III.G   Summary of Chapter III

In this chapter we have discussed deterministic optimization and presented the version that we use in the research. We have described several techniques that we have employed to make the deterministic optimization more robust, accurate, and efficient; these are summarized as follows. We expose the object to multiple beams to mitigate the ill conditioning of the inverse problem. We accelerate the transport

forward calculation by applying Krylov-subspace based acceleration techniques to it. Regarding the inverse model, we apply nonlinear conjugated gradient updating scheme to search for the optimal solutions. We have introduced a variable-change technique to convert the constrained optimization problem into an unconstrained problem. This technique may be beneficial on its own to many gradient-based iterative optimization problems as long as the proper variable-change function can be found.

CHAPTER IV

NEW APPROACHES IN HEURISTIC OPTIMIZATION

IV.A   Introduction

Traditional inverse-transport methods attempt to determine interaction parameters -cross sections - as a function of position in the object. As the modeling of the problem becomes more realistic, the number of unknown parameters (spatial and energy-dependent cross sections) increases drastically, which makes the optimization problem far more difficult to solve. The dimension of the search space is the number of spatial regions (cells) times the total number of unknown cross sections, which in a neutron scattering problem scales as the square of the number of energy groups or energy points (because of group-to-group scattering). The larger number of unknowns (higher-dimensional space) makes the problem more ill-conditioned and increases the number of iterations needed to find a minimum. Further, in practice it is highly unlikely that the set of parameters found in a given cell by the search algorithm will correspond to any real material. Thus, even if a set of parameters is found that yields an acceptably small objective function, the end goal of determining the material distribution in the object may remain difficult to achieve.

In this chapter we describe the strategies we have devised to address these difficulties and describe how each strategy can be applied to a particular class of neutron tomography problems. A common theme of these strategies is that they dramatically reduce the dimension of the search space for the optimization algorithm that is employed at the end. The basic strategies are:

1. Use an inexpensive forward-transport model with a gradient-based search algorithm to gain helpful information about the problem. The inexpensive model could, for example, use only a small number of energy groups, a relatively coarse spatial grid, low-order anisotropic scattering, and possibly diffusion instead of transport.

2. Use the information from the first step to group cells that are likely to have the same material (even though this material may be unknown) into "material regions". Some cells may fall into "interface regions" that are spatially between "material regions". Cells in such regions are likely to contain the same material as one of the bounding material regions.

3. Use prior knowledge or hypothesis to create a library of candidate materials. The search procedure will ultimately consider materials only from this library.

4. Exploit hypotheses for the internal structure of the object. For example, the analyst might ask the algorithm to look for a single one-material region embedded in a homogeneous background.

5. Employ a stochastic-based heuristic optimization method to search for a material distribution that satisfies the constraints imposed by previous steps. An important part of this is that for each trial to be tested, each cell is assigned the cross sections from a real material from the candidate library. That is, the unknown becomes the material, not the cross sections. Further, all the cells in a given material region are assigned the same material in a given trial. Finally, each cell in an interface region is assigned the material of one of its bounding regions, and the interface is required to conform to the analyst's hypotheses. Taken together, these constraints dramatically reduce the dimension of the search space. As we shall show, this makes it feasible to obtain very good solutions to very difficult problems.

An example can illustrate the dramatic reduction in problem complexity that these strategies can achieve. Suppose that a transport model of adequate fidelity for a given two-dimensional inverse problem is characterized by a 40×40 spatial grid, 15 energy groups, and 3rd-order anisotropic scattering. If cross sections are the primary unknowns, as is the usual case for gradient-based search algorithms, then each cell contains four cross-section moments for each allowed group-to-group

scattering transition, which could mean up to $4 \times 15^2 = 900$ scattering cross sections per cell. With 1600 cells this means up to 1,440,000 unknown scattering cross sections in this modest two-dimensional problem. If there is no upscattering the number remains large (768,000). This is an extremely high-dimensional space in which to perform a search, even though this is a rather simple example problem.

This motivates us to consider our problem from a different point of view. Instead of viewing the unknowns as cross sections, we view the unknowns as the material itself. This reduces the unknowns from a large number per cell to only one per cell. However, it changes the nature of the problem and thus the methodologies needed to solve it. The unknowns are now discrete (the material index in a given spatial cell) instead of continuous (a real number for a given cross section in a given cell). Now we cannot take meaningful derivatives of the objective function with respect to an unknown and thus cannot apply gradient-based minimization approaches. In fact, the problem now can be viewed as a combinatorial optimization (CO) problem. This type of problem is often attacked using stochastic-based heuristic approaches such as simulated annealing, tabu search, or genetic algorithms. In these approaches, guesses for the solution (material index for each spatial cell) are generated using random numbers coupled with some information learned from previous guesses. When we evaluate the direct application of standard CO methods (simulated annealing, genetic algorithms, etc.) to our problem we find that the dimensionality of the problems of interest is so high that the methods are not likely to produce results with sufficient efficiency for practical use. Returning to our example problem with its 40×40 spatial grid, suppose that prior knowledge or a reasonable guess suggests that there are only a few - say 10 - materials that could be in the object. Then there are 10 possibilities for each of the 1600 cells, which means 10^{1600} possible configurations. This is a large search space, in which it is difficult to find a global minimum.

Suppose that instead of direct application of gradient-based searches or stochastic-based approaches we employ the strategies outlined above, suppose for illustration

that after the second step we arrive at the cell groupings shown in the figure [see Fig. IV.1]. Further, suppose that after the second step we have determined that only 2 of the candidate materials fit what has been learned about the M2 region and only 3 fit this for the M1 region.

Suppose that instead of direct application of gradient-based searches or stochastic-based approaches we employ the strategies outlined above, suppose for illustration that after the second step we arrive at the cell groupings shown in the figure [see Fig. IV.1]. Further, suppose that after the second step we have determined that only 2 of the candidate materials fit what has been learned about the M2 region and only 3 fit this for the M1 region.
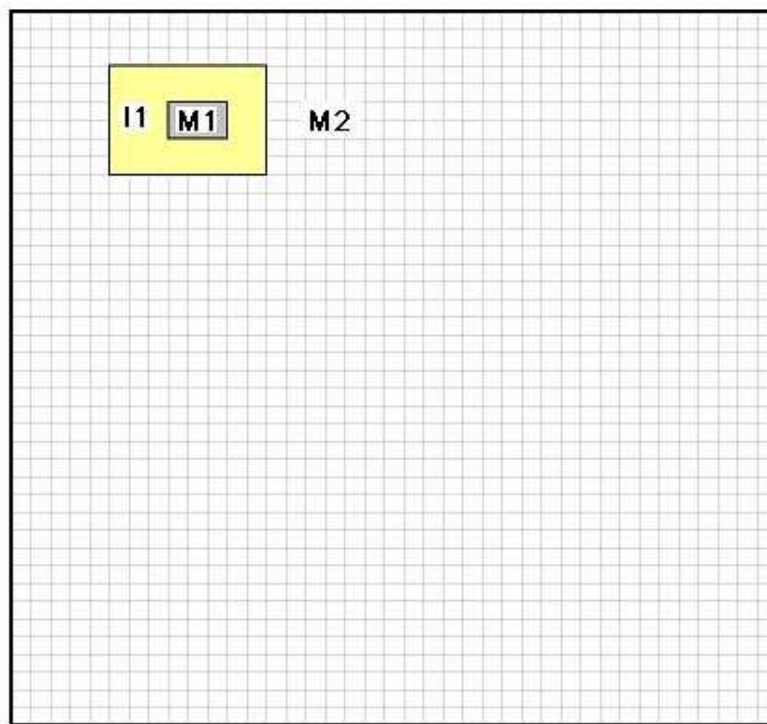
Fig. IV.1: Three regions (M1, M2, I1) are determined after cell grouping process in a demonstration example with 40×40 grids discretization.

Finally, suppose the analyst postulates that the object contains a single rectangular "inclusion" in a homogeneous background. Now we ask how many possible configurations fit the constraints of what has been learned and what has been postulated. There are only four possible locations of the left boundary of material M2, 3 for the top, three for the bottom, and three for the right. This gives only $4 \times 3 \times 3 \times 3$ = 108 possible geometric layouts that fit the constraints and postulate. In each of these there are 3 possible M1 materials and 2 possible M2 materials, or 6 possible combinations. The total possible configurations is therefore 648. This is to be compared against the 10^{1600} possible configurations that we would encounter with a pure brute-force approach. Note that if the postulate is correct, then one of the 648 configurations is very likely the single optimal configuration out of the original 10^{1600} possibilities.

This is an admittedly simple example, but as we shall see later it is not far from what can be achieved in the test problems that we have studied.

In the remainder of this chapter we provide an explicit example of how each of the above strategies can be implemented for a family of two-dimensional neutron-tomography problems. This includes a detailed description of the algorithm that implements each strategy.

IV.B   Demonstration Problems

The problems on which demonstrate our approach are two-dimensional rectangular objects. Measurements are provided from detectors on three sides while an object is subjected to a neutron beam on the fourth side, and this is repeated with the beam striking the other three sides. We assume a room-temperature Maxwellian distribution of the incident neutrons and thus model the system using Maxwellian-averaged cross sections. For simplicity, the exiting partial current from a given segment of a given side is assumed to be proportional to the detector reading associated with that segment. For the demonstrations in this work, we use the same transport code

to generate "measurements" that we use to perform forward calculations during the inverse-transport solution, and we do not add noise to the measurements. A practical algorithm must deal with noise, and there are established methods for this. Our goal in this stage of algorithmic development is to determine whether our strategies can make it possible to obtain sharp answers in the presence of a high degree of scattering, where previous approaches have been largely unable to do so even without noise.

IV.C   Overview of the Methods in Chapter IV

Our forward transport model is a one-group equation with linearly anisotropic scattering in both the deterministic gradient-based optimization stage and the final heuristic optimization stage. In the former stage we use a moderately coarse spatial grid (say 20×20 cells); in the final step we use a finer grid (say 40×40 cells). The methodology permits more difference between the model fidelities of the two stages, but this is what we have chosen for our demonstrations.

In the previous chapter we described the details of the deterministic gradient-based search that forms the initial stage of our approach. This includes a change of variables, a nonlinear conjugate-gradient algorithm, Brent's method embedded for line searches, etc. See Chapter III for details.

In this chapter, we present a hierarchical algorithm to solve the same problem with the following steps:

1. We use the same model with the exact material distribution to generate the "measurements" and we do not add any noise. This is to simplify our initial demonstration of the method and to determine whether it can work under ideal circumstances. If it does, then future work can address practical complications such as measurement noise.

2. We employ a cell-grouping algorithm based on the prior knowledge we gain from the deterministic optimization stage. This algorithm divides the domain of the problem into three regions: background, inclusion, and interface. Note that it is possible there exists multiple inclusion regions.

3. We begin with a library of ten candidate materials. The library includes water, iron, paraffin, boron, silicon, nitrogen, cadmium, aluminum, natural uranium and high enriched uranium (HEU). For all ten materials we used thermal cross sections averaged with a roughly-Maxwellian spectrum. These cross sections are generated with MCNP output post process.

4. We allow the user to impose constraints on what kind of inclusion the algorithm will try to find. In our examples we constrain the interface so that it cannot be arbitrarily ragged; for example, a "finger" of one material that is one cell wide is not permitted to extend into the other material to a depth beyond one cell. We employ bias in the stochastic material-choice algorithm for the interface region, such that a cell close to the inclusion region is more likely to be assigned the inclusion material and a cell close to the background region is more likely to be assigned the background material.

5. The stochastic based heuristic optimization method employed in the final step is extremely simple. Each guess is determined independently from all other guesses (no learning is attempted), using random numbers for each degree of freedom. The biasing described above is employed; the constraints described above are imposed.

We have addressed some of the steps (step 1 and 2) in the algorithm which are associated with the deterministic optimization procedure in Chapter III. In this chapter we present the steps associated with heuristic optimization in details in forthcoming sections. Meanwhile we elucidate the advances we devised in these steps.

IV.D   Cell Grouping Technique

Our strategies in this stage are based on the results gained from the deterministic optimization process. We group into *regions* the cells that are likely to contain the same material; the cells in the same region have similar or related cross section information as provided by the deterministic search. Another kind of region can be identified as likely to contain interfaces between materials. Henceforth each cell will be associated with a region, with materials varying by region according to some chosen constraints. After this grouping, the forthcoming search process will work on regions rather than cells, which greatly reduces the search-space dimension and thus greatly saves computation time.

We must devise criteria to divide the problem into different regions. Many criteria are possible here; for the test problems in this research, in which there is a single material that forms one or more inclusions within a homogenous background material, we set up the following simple criteria:

$$\Sigma_{tr} > \Sigma_{tr,mean} + \alpha(\Sigma_{tr,max} - \Sigma_{tr,mean}) \Rightarrow \text{ Inclusion region}$$

$$\Sigma_{tr} < \Sigma_{tr,mean} + \beta(\Sigma_{tr,max} - \Sigma_{tr,mean}) \Rightarrow \text{ Background region} \quad . \qquad \text{(IV.1)}$$

$$\text{otherwise } \Rightarrow \text{ Interface region}$$

Here Σ_{tr} refers to the "transport" cross section, defined as $\Sigma_t - g\Sigma_s$. The equations above apply if the inclusion material has a larger transport cross section than the background. If the results of the gradient-based search show that an inclusion has a lower cross section these equations are modified in the obvious way. We chose in the test problems that will be shown in the next chapter.

With the criteria we set up in Eq. (IV.1) we can group the cells of the problem into 3 regions: background region, interface region and inclusion region. Note that the number of inclusion and interface region is determined by the search results provided by the first search stage. After grouping cells into regions, we proceed with the search

process in the scale of regions rather than cells. Furthermore, as described above, we will search in the regions in the space of materials rather than cross sections.

IV.E   Material Restriction Technique

As we address in the introductory section of this chapter, in this optimization stage we treat materials as unknown rather cross sections. Therefore we start this section with a description of building a material candidate library (MCL), in which the different treatment to regular material and fissile material are address separately. Then we present some simple material restriction techniques we apply to reduce the material search dimension in the regions of the object.

IV.E.1   Building material candidate library (MCL)

1. Regular materials

We evaluate the one-group (i.e. thermal-energy with Maxwellian-spectrum collapse) microscopic cross sections of each material as following:

$$\overline{\sigma_i} = \frac{\int_0^{E_{th}} \sigma_i(E)\phi(E)dE}{\int_0^{E_{th}} \phi(E)dE} = \frac{(F4 + Fm4) \text{ Tally}}{F4 \text{ Tally}}, \tag{IV.2}$$

where the subscript i represents the *type of interaction* with which the cross section is associated. We also include the tally number for the integral in Eq. (IV.2). These tallies are generated with MCNP [58] output from a problem in which a homogeneous volume of the given material is subjected to an incident Maxwellian beam of neutrons. The MCNP input source we use to evaluate the cross section is attached in Appendix A.3.

Another parameter we must have in our cross-section library is the linear anisotropic factor of each material, which is defined as

$$g = \frac{\int_{-1}^{1} \mu_0 \sigma_s(\mu_0)d\mu_0}{\int_{-1}^{1} \sigma_s(\mu_0)d\mu_0}. \tag{IV.3}$$

Different isotopes have different specific $\sigma_s(\mu_0)$ distribution in neutron-target inter-action. But if we assume isotropic scattering in center-of -mass (COM) system, then the average cosine of the scattering angle in the laboratory system is $g = \frac{2}{3A}$, where A is the ratio of the nucleus mass to the neutron mass, or approximately the atomic mass number of the scattering nuclei. Because thermal-neutron scattering is very nearly isotropic in the COM frame under many interesting scenarios, we this equation to generate values of g for each material in our candidate library.

2. Modification for fissile materials

In order to gain more practical interest, we want to add some fissile materials in our material library, such as natural uranium, high-enriched uranium (HEU), etc. But recalling the forward model development in Chapter III, we built the forward model in the problem with transport equation valid only for non-multiplying system; i.e., we did not incorporate the fission source in the forward model. Therefore we need to make some modification of the cross sections of fissile material to make it suitable to be worked in our model.

The one group transport equation with fission source is described as

$$\underline{\Omega} \cdot \underline{\nabla}\psi(\underline{r}, \underline{\Omega}) + \Sigma_t(\underline{r})\psi(\underline{r}, \underline{\Omega})$$
$$= \frac{1}{4\pi}\Sigma_s(\underline{r})\left[\phi(\underline{r}) + 3g\underline{\Omega} \cdot \underline{J}(\underline{r})\right] + \frac{1}{4\pi}\nu\Sigma_f(\underline{r})\phi(\underline{r}) + S_{ext}(\underline{r}, \underline{\Omega}) \quad . \tag{IV.4}$$

But in our current model, we are really working on the equation

$$\underline{\Omega} \cdot \underline{\nabla}\psi(\underline{r}, \underline{\Omega}) + \Sigma_t(\underline{r})\psi(\underline{r}, \underline{\Omega}) = \frac{1}{4\pi}\Sigma_s(\underline{r})\left[\phi(\underline{r}) + 3g\underline{\Omega} \cdot \underline{J}(\underline{r})\right] + S_{ext}(\underline{r}, \underline{\Omega}) \quad . \tag{IV.5}$$

Thus in order to "squeeze" Eq. (IV.4) to be the form of Eq. (IV.5), we defined the "modified parameters" as

$$\begin{cases} \widetilde{\Sigma_s}(\underline{r}) = \Sigma_s(\underline{r}) + \nu\Sigma_f(\underline{r}) \\ \widetilde{g} = g\dfrac{\Sigma_s(\underline{r})}{\Sigma_s(\underline{r}) + \nu\Sigma_f(\underline{r})} \end{cases} . \tag{IV.6}$$

Then Eq. (IV.4) is reshaped to the form of

$$\underline{\Omega} \cdot \underline{\nabla}\psi(\underline{r}, \underline{\Omega}) + \Sigma_t(\underline{r})\psi(\underline{r}, \underline{\Omega}) = \frac{1}{4\pi}\widetilde{\Sigma_s}(\underline{r})\left[\phi(\underline{r}) + 3\widetilde{g}\underline{\Omega} \cdot \underline{J}(\underline{r})\right] + S_{ext}(\underline{r}, \underline{\Omega}) \quad . \tag{IV.7}$$

Table IV.1: Properties of the 10 materials in MCL.

#	Material	Σ_t (1/cm)	Σ_s (1/cm)	$g(\frac{2}{3A})$
1	Paraffin	0.567	0.567	5.56E-2
2	B-10	5.54E+2	3.20E-1	6.67E-2
3	water	0.744	0.736	3.70E-2
4	Si	0.110	0.103	2.37E-2
5	Fe	1.179	0.967	1.19E-2
6	Nitrogen	6.54E-4	5.54E-4	4.76E-2
7	Cadmium(Cd)	0.301	0.247	5.90E-3
8	Aluminum(Al)	0.097	0.083	2.47E-3
9	Natural Uranium	0.821	0.921	1.40E-3
10	HEU	2.70E+1	5.25E+1	3.61E-5

Therefore, for fissile material, the cross sections in the material candidate library are calculated with modified version as expressed in Eq. (IV.6). We realize that this ignores the extremely important fact that fission neutrons are born with MeV-range energies, whereas the cross sections in our model are from the sub-eV energy range. Thus, this is not a physically realistic model of fissile material. Nevertheless, it provides a reasonable set of cross sections for testing our algorithms, which is our purpose.

Table IV.1 gives the parameters of the 10 candidate materials we set up in the material candidate library (MCL).

IV.E.2   Material restriction strategy

With the availability of the MCL, we are ready to set off the material restriction step. The purpose of the step is to narrow the material candidates to be considered in

each region hence reduce material search burden in the region. Given the few-group parameters found for the cells in a given region, an material restriction algorithm determines which materials could realistically have few-group parameters that are similar, and then places those materials in the material candidate library (MCL) for that region.

The material restriction work is taken place after we finish the gradient-based continuous optimization procedure. At this time, we suppose we already have the approximated cross section information (i.e. σ_s, σ_t, σ_{tr}) for each cell. The ultimate goal is to know exactly what the material is in each cell. The material restriction part will help us to greatly narrow the search space with respect to the materials in the candidate library and tells us which materials are most likely to reside in each region. This work will drastically save our energy and time for our next combinatorial optimization procedure.

The next step is to restrict the material candidates in the inclusion and background regions by comparing each material's cross sections to the cross sections that were found in the deterministic search process. We first calculate an error associated with each material for each region. Many "error" metrics and restriction criteria are possible; for this illustration we have chosen the following metric:

$$e_m = error = \frac{1}{3}\left(\left|\frac{\Sigma_s^m - \Sigma_s^r}{\Sigma_s^m + \Sigma_s^r}\right| + \left|\frac{\Sigma_t^m - \Sigma_t^r}{\Sigma_t^m + \Sigma_t^r}\right| + \left|\frac{\Sigma_{tr}^m - \Sigma_{tr}^r}{\Sigma_{tr}^m + \Sigma_{tr}^r}\right|\right) \quad . \qquad \text{(IV.8)}$$

Here Σ^m is the cross section of a given material and Σ^r is cross section determined by the gradient-based search, averaged over the given region. We restrict the material candidates for the region based on the following criterion: if there exists one and only one material that has $e_m < a$, the region is determined to be that material m; i.e., we find the material in the region. Otherwise we include all materials for which $e_m < b$. Here a is a relatively small number and b is a relatively larger number; In the model problems in this research we use $a = 0.01$, $b = 0.5$. At the end of this stage we have significantly reduced the material search dimension for the final step.

Each material in the MCL will be sorted for the region according to the error associated with it. Then the one with the smallest error will be the first choice for this region. In some cases, if the deterministic search result is accurate enough, the algorithm may locate the correct material for the background region.

IV.F   Heuristic Optimization

The final step is the combinatorial optimization process. A single iteration in this step proceeds as follows. First the material in the inclusion region is selected from the restricted set of candidates, as is the material in the background region. Then the algorithm selects one material for inclusion region from the restricted set of candidates of this region. With background region and inclusion region determined, the algorithm proceeds to assign one of these two materials to each cell in the interface region.

To acquire higher accuracy from the optimization search in this stage, we refine the mesh construction of the object by using smaller grid size for each cell. For example, a model problem that uses a 20x20 cells discretization configuration in the first stage will be refined to 40x40 cells as demonstrated in Fig. IV.2.

The assignment begins with the cells adjacent to inclusion region and marches out to those adjacent to background region, proceeding as follows. For each cell in the inner ring the material was chosen based on a random number and a bias factor. The probability that the inclusion material was assigned to a cell was approximately the cell's distance to background region divided by the distance from inclusion region to background region. The bias technique is illustrated in Fig. IV.3.

With the demonstration in Fig. IV.3, the algorithm has the following steps:

1. Find the longest distance between a cell in the interface region and the center of the inclusion region, call it $d_{\max}$, and record the center of the inclusion region.

2. Find the shortest distance between a cell in the interface region and the center of the inclusion region, call it $d_{\min}$,
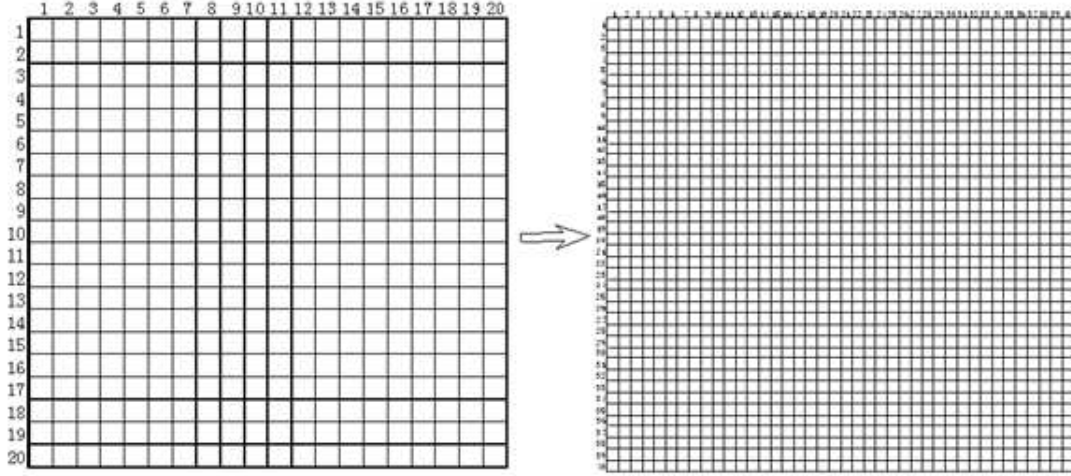
Fig. IV.2: The number of cells in the mesh is quadrupled - 40×40 instead of 20×20 - in the optimization of this stage.

3. For each cell in interface region

a) Calculate the length from the center of the cell to center of the inclusion region, call it x,

b) The corresponding probability threshold of the cell is $P_i = \dfrac{d_{\max} - x}{d_{\max} - d_{\min}}$,

c) If $rnd < P_i$ then choose the interface material as the material in this cell, otherwise choose background material.

To further reduce the search space we could impose other constraints that embody prior knowledge or that are postulated. For example, we could constrain the algorithm to consider only material sub-objects with relatively sharp boundaries as opposed to fragmentary objects. We could bias the stochastic search process so that it favors a small number of material regions embedded in a single-material background. The chosen constraints restrict the kinds of material distributions that will be considered as viable candidates in the final step. This is described in more detail below.
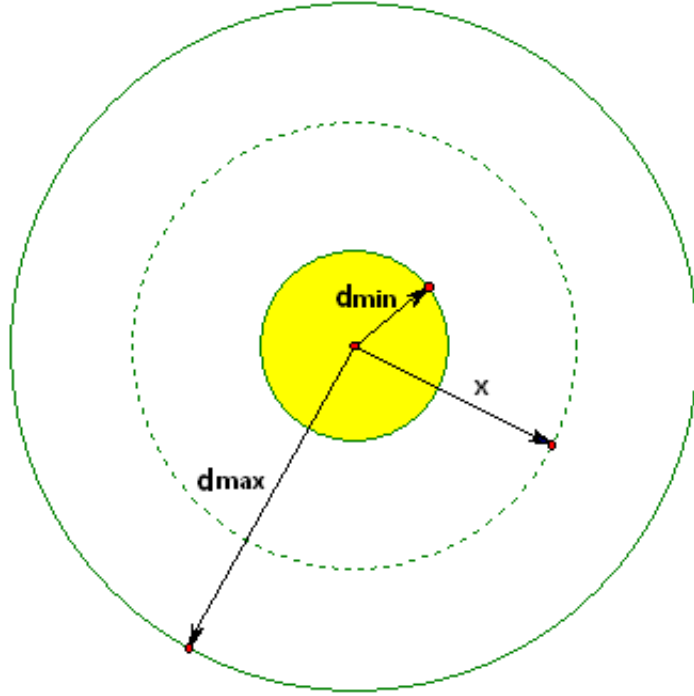
Fig. IV.3: Bias rule applied in combinatorial optimization.

After materials are assigned to the inner ring of interface-region cells we checked whether the assignments for other interface-region cells were determined by constraints imposed by the analyst. For example, given the constraint of a relatively smooth interface between the inclusion and the background, if the background material were assigned to an entire row of cells, then all interface cells between that row and the background region must also be the background material - otherwise the inclusion region would be disjoint or more ragged than permitted by the imposed constraint. This greatly reduces the number of allowed configurations and avoids time-consuming calculations of unrealistic configurations.

Once a configuration is constructed in accordance with prior knowledge and imposed constraints, a full-fidelity transport forward model with refined mesh is applied

to evaluate the objective function. This procedure terminates either when a suitably small objective function is found or when an iteration limit is reached.

IV.G   Summary of Chapter IV

In this chapter, we first introduced the motivation and objective of heuristic optimization involved in the research. We describe our general strategies for addressing difficult inverse-transport problems with the goal of performing well on problems with a high degree of scattering. Then we walk through in detail all the steps involved in the hierarchical approach we develop to carry out the stochastic based optimization for our problem. These steps include cell grouping, material restriction and combinatorial optimization with smart constraints imposed.

With the description of the steps of the heuristic optimization algorithm, we mainly focus on the novelties we devise in the heuristic optimization process, in which we combine the deterministic and stochastic optimization techniques together for the purpose of fully leveraging the advantages of both sides. We especially focus on the dimension reduction techniques we apply in the model problems. We believe some of the ideas we present in this chapter will advance the approaches in neutron tomography area.

In next chapter, we will apply the techniques we describe in Chapter III and IV to some test problems to demonstrate the efficiency and advantages of the methodology we introduce here.

CHAPTER V

RESULTS

V.A   Introduction

In foregoing two chapters we have fully discussed the methodology for solving inverse transport problems that we have developed in the research. In this chapter we apply these methods to some simple test problems and thereby demonstrate the feasibility and efficiency these approaches.

We present two test problems in this chapter. Both of them are in 2-D Cartesian coordinate system and constructed with background material containing some block inclusions. We choose the size of the objects to be several mean free paths thick. We also choose the materials in the object (both background and inclusion material) to have high scattering cross sections. This creates problems in which the detected particles emerging from the object are dominated by scattered particles. Solving such problems is the main concern we address in the research.

V.B   Model Problem 1: Water with one iron inclusion

We first consider a model problem with two materials inside an object, with an "inclusion" of one material embedded in a "background" of another material. Fig. V.1 is a schematic diagram for the problem.

Table V.1 lists the properties of the materials in the model problem. The transport cross section (Σ_{tr}), mean free path (mfp) and scattering ratio (c) are deduced properties which are defined as:

$$\Sigma_{tr} = \Sigma_t - g\Sigma_s, \quad mfp = \frac{1}{\Sigma_t}, \quad c = \frac{\Sigma_s}{\Sigma_t}. \tag{V.1}$$

We list these three properties because they are usually considered important and useful characteristics of the physical problem. For example, by observing the magnitude of mfp and c, we may state that our model problem is optically thick (λ 7 mean
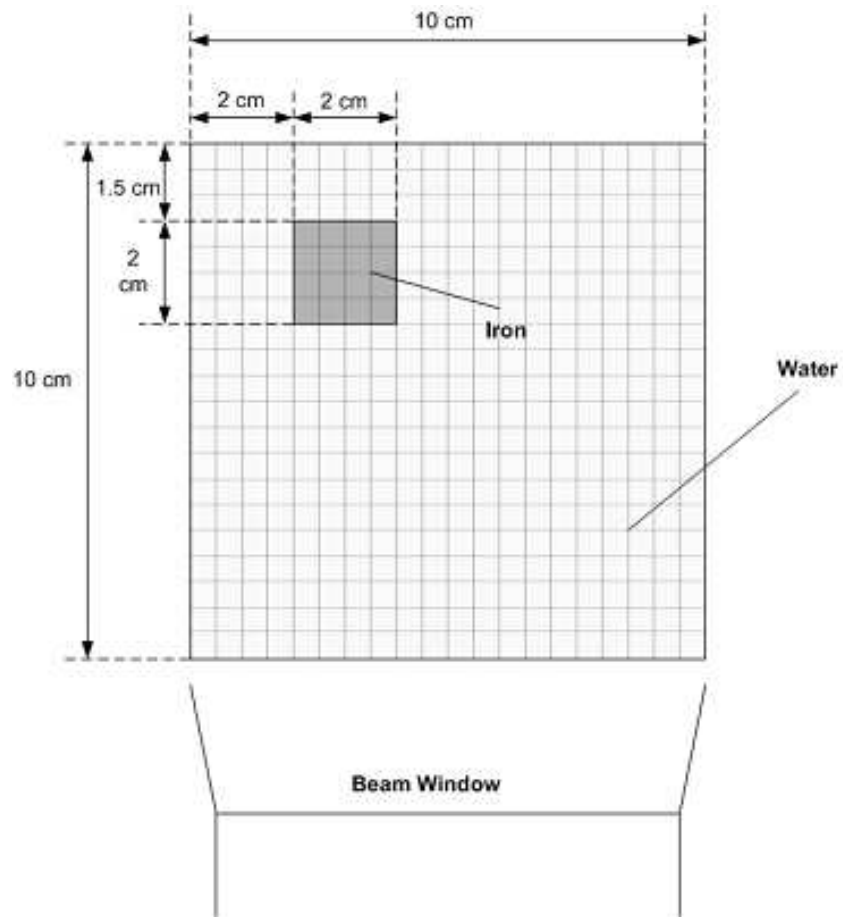
Fig. V.1: Schematic diagram of the one inclusion problem.

free paths) and highly scattering (vast majority of collisions are scattering events) problem. We will use Σ_{tr} as a representative factor to infer material distribution in our example problem.

The configuration of this test problem is the same as the one we present in Chapter II, in which we attempted to reconstruct the tomogram of the object with an FBP-based method. We start our demonstration with the exactly the same problem configuration and material constitution with the purpose of emphasizing the advantages of our proposed methods.

Table V.1: Physics properties of the materials in the model problem.

Material	Water	Iron
Σ_s (1/cm)	0.736	0.967
Σ_t (1/cm)	0.744	1.18
g $\left(\frac{2}{3A}\right)$	3.70E-2	1.20E-2
Σ_{tr} (1/cm)	0.716	1.167
mfp (cm)	1.35	0.848
c	0.990	0.820

Before we proceed to present the results from the inverse problem, we show some work to verify the solution of transport solver in our forward model. Recall that we assume if we know the material constitutes of the object and incident source, the forward model is capable of predicting accurate radiation exiting the boundary of the object. The results yielded from our Sn transport solve are compared to MCNP simulation results in Fig. V.2 with the same problem configurations shown in Fig. V.1. The results in Fig. V.2 shows the predicting radiation exiting from three sides (left, right and back side) of the object all agree with the Monte-Carlo simulation results very well. Note that both radiation data in Fig. V.2 have been normalized to their maximum value.

Next we begin our approach by approximately solving the inverse problem (searching for cross sections and g factors) with gradient-based deterministic optimization (as described in Chapter II). This is the first stage of our methodology. The image reconstruction yielded by this stage is illustrated in Fig. V.3. The corresponding objective function change with the number of the iterations is presented as the plot in Fig. V.4. The overall normalized objective function has been reduced by a factor
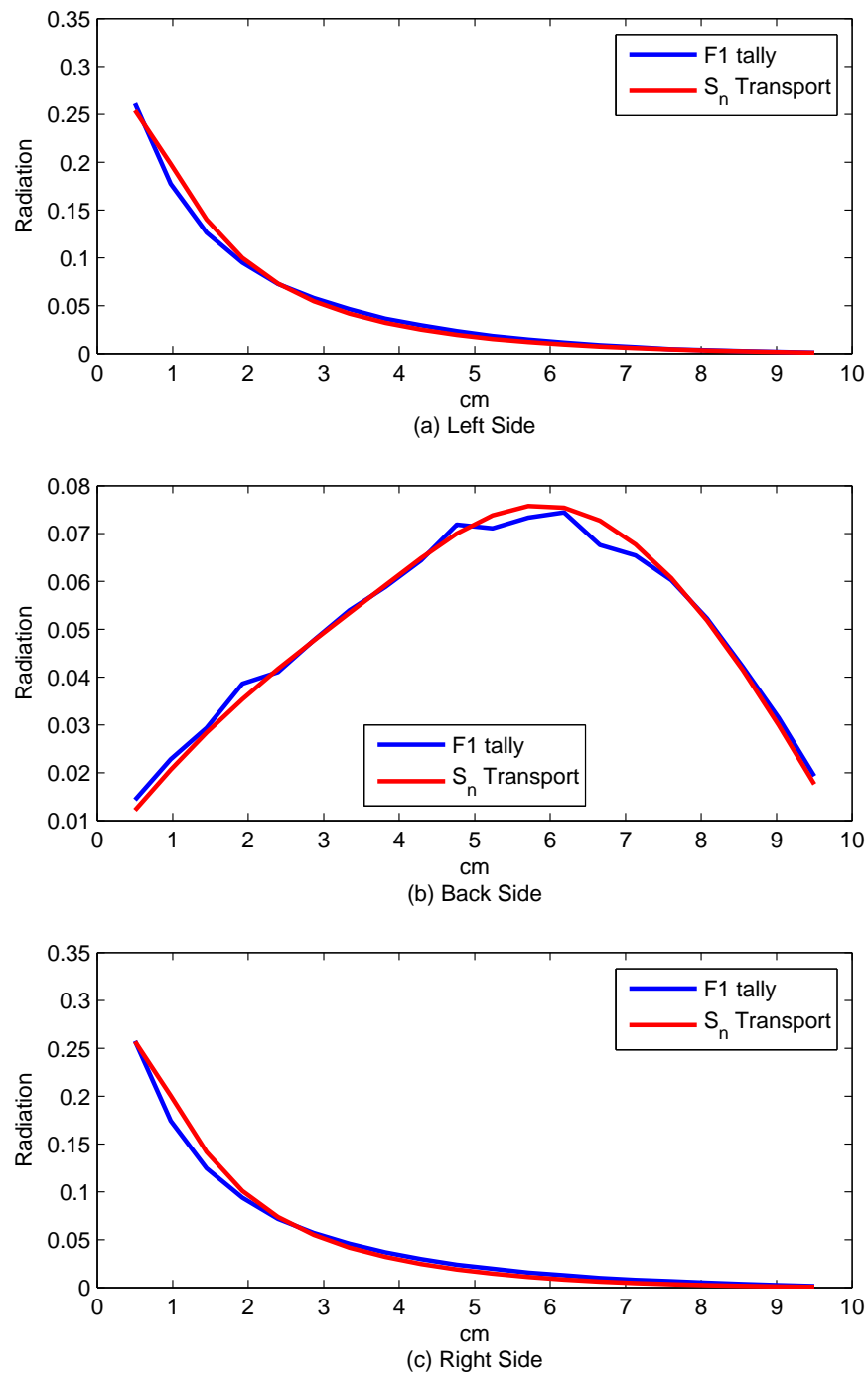
Fig. V.2: Comparison of MCNP F1 tally and S_N transport solution.

of 10^6 after 1000 iterations which indicates that the gradient-based updating scheme is working very efficiently.
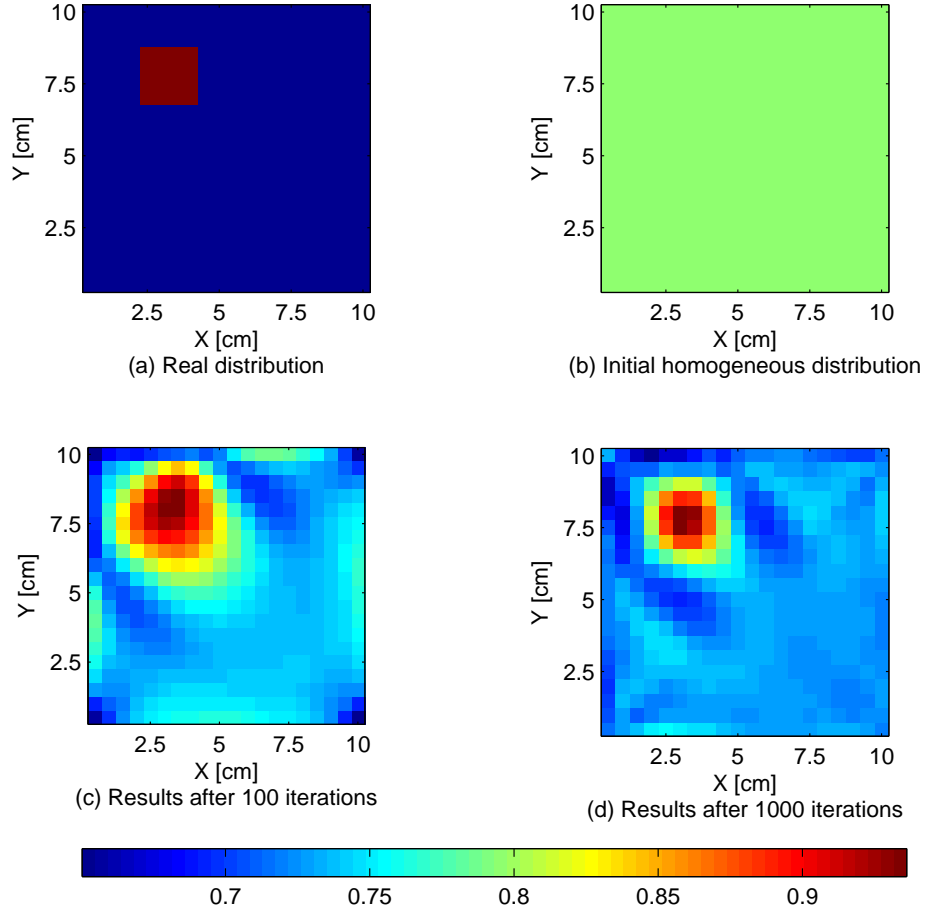
Fig. V.3: Transport cross section (Σ_{tr}) distribution obtained from deterministic CG based iterative search scheme for the one iron problem. (a) The real Σ_{tr} (background is water and square inclusion is iron). (b) Initial guess for Σ_{tr}. (c) and (d) are results after 100 and 1000 iterations, respectively.

Fig. V.3(a) is the actual Σ_{tr} distribution of the problem as shown in Fig. V.1, repeated here for comparison with our first-stage results. We start the deterministic optimization process with a homogeneous material distribution (see Fig. V.3(b)). Fig. V.3(c) and (d) are the Σ_{tr} distribution the object yielded from the process of
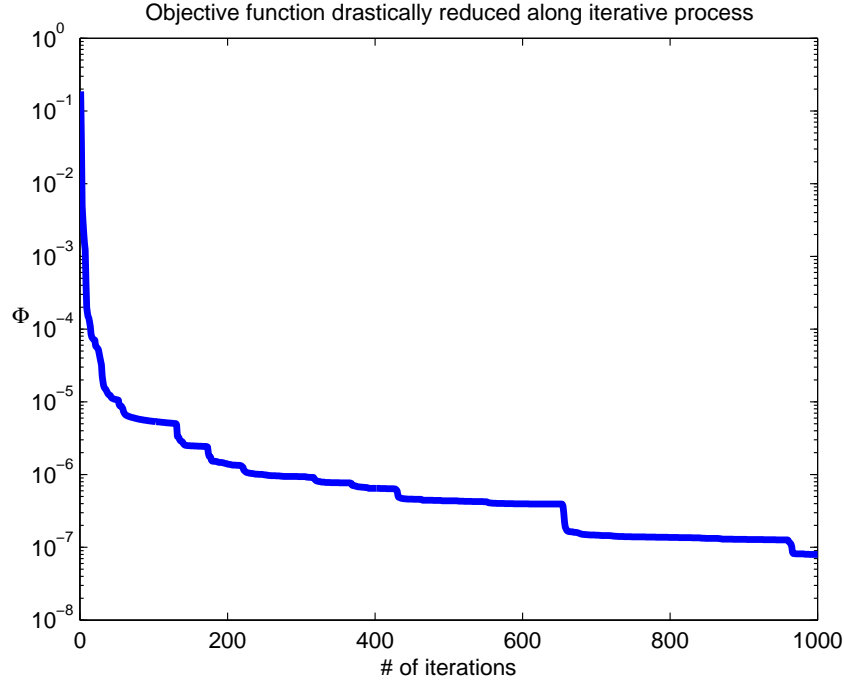
Fig. V.4: The objective function changes after each iteration for the one inclusion problem.

updating schemes of our inverse model. We expect the more accurate results as the more iterates carried on. We see that the gradient-based continuous search process indicates that there is an inclusion and roughly tells its location after 1000 iterations. By this stage we have the similar outcome for parameters Σ_t and g as well in our inverse problem though we only depict Σ_{tr} as representative in Fig. V.3.

We may use this information to try to discern the real physical material in the object and in fact many traditional tomography methods do work in this way. However, there are significant drawbacks associated with this approach. For example, the converged cross sections always have deviations from the real ones and they are not constrained to be realistic; that is, they may not correspond to any real material. In addition, it is usually difficult to tell which material is inside the object from this limited information, and it is also difficult to locate the boundary and thus quantify

how much area is occupied by the inclusion. Our method, whose results we are about to present, attempts to overcome these drawbacks.

Here we emphasize again that we continue our process by working with *materials* themselves as unknowns rather than *cross sections*. First we group the cells based on the knowledge gained from the first stage as we describe in Chapter IV. We use the prior information we obtain in Fig. V.3 and carry out cell grouping process to combine the cells with close cross section quantities to be same region. The details of the criterion applied for cell grouping is described in section D of Chapter IV. The result of cell grouping is illustrated in Fig. V.5, where we see 3 regions: external region (region 1), interface region (region 2) and internal region (region 3).
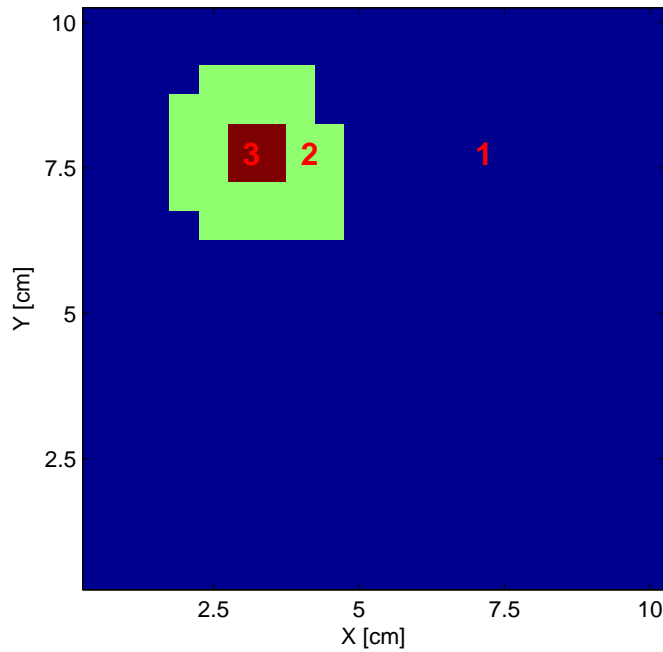
Fig. V.5: Different regions identified by the cell grouping process for the one inclusion problem. (Color in this figure denotes region only, not any particular numerical value.)

The next step is to restrict the material candidates in the inclusion and background regions by comparing cross sections of each material in material candidate

library (MCL) to the cross sections that were found in the deterministic search process. The detailed criterion and process for material restriction is described in section E of Chapter IV. For the example problem at the end of this stage we have significantly reduced the material search dimension for all those three regions: our algorithm determined that the background material must be water; thus region 1 will always be water in the subsequent trials. Our algorithm determined that the inclusion could be any one of four different materials: iron, water, paraffin, or natural uranium.

The final step is the combinatorial optimization process. A single iteration in this step proceeds as follows. First the material in the inclusion region is selected from the restricted set of candidates, as is the material in the background region. (Implementation detail: instead of randomly selecting the inclusion material for each iterate, which would have apportioned roughly 25% of the iterations to each candidate material, we deterministically assigned 25% of the iterations to each candidate material.) With water assigned to region 1 and a choice made for region 3, the algorithm proceeds to assign one of these two materials to each cell in the interface region (region 2).

The assignment begins with the cells adjacent to region 3 and marches out to those adjacent to region 1, proceeding as follows. For each cell in the inner ring the material was chosen based on a random number and a bias factor. The probability that the inclusion material was assigned to a cell was approximately the cell's distance to region 1 divided by the distance from region 3 to region 1. After materials were assigned to the inner ring of interface-region cells the algorithm checks whether the assignments for other interface-region cells are determined by defined constraints. For example, if water were assigned to an entire row of cells, then all interface cells between that row and the water region must also be water - otherwise the inclusion region would be disjoint or more ragged than permitted by the imposed constraint.

This greatly reduces the number of allowed configurations and avoids time-consuming calculations of unrealistic distributions.

The results of applying this algorithm are shown in Fig. V.6 and quantitatively assessed in Table V.2. With only 200 random guesses (50 for each candidate inclusion material), the configuration shown in the figure was found and selected as the best of the 200 distributions because it had the lowest objective function. The graphical solution is strikingly similar to the correct distribution, but more important is the quantitative comparison shown in Table V.2. Here we find that the method produces *exactly the correct mass* (area corresponds to mass) of the *correct material* and almost exactly the *correct center-of-mass location*. This is exactly what one would like to get from a neutron tomography method.

Fig. V.6: Results from the heuristic optimization for the single-inclusion problem: Material distribution from the stochastic heuristic optimization after 200 iterations (50 iterations per candidate inclusion material). Color in this figure denotes material only, not any particular cross-section value.

Table V.2: Inclusion location and area comparison for one inclusion problem.

Parameter	Actual [Fig. V.3(a)]	Opt. Result [Fig. V.6]
Material	Iron	Iron
X-center (cm)	3.00	2.97
Y-center (cm)	7.50	7.49
Area (cm^2)	4.00	4.00
Iron/Water	4.17E-2	4.17E-2

V.C   Model Problem 2: Water with two iron inclusions

The schematic layout of the second model problem is shown in Fig. V.7. In this problem, the object has two iron inclusions being located in different places inside water (see Fig. V.7). The dimension of the whole object is the same as the first problem. One inclusion (the left-top iron block in Fig. V.7) has the same size and located in the same place as in the first test problem. A smaller iron inclusion is placed close to the right bottom corner of the object. The properties of the background and inclusion materials in this problem are the same as listed in Table V.1.

The transport cross section (Σ_{tr}) distribution results we obtain in the deterministic optimization stage for this problem is shown in Fig. V.8. We again start the optimization process with an homogeneous material distribution (see Fig. V.8(a)). Fig. V.8 (c) and (d) shows the Σ_{tr} distribution after 100 and 1000 conjugate-gradient iterations respectively. We see more accurate results in (d) and this approximately infers the location and size of the two inclusions.

Fig. V.9 is the plot of the objective function in this problem as a function of the number of iterations. This demonstrates the efficiency of the iterative search
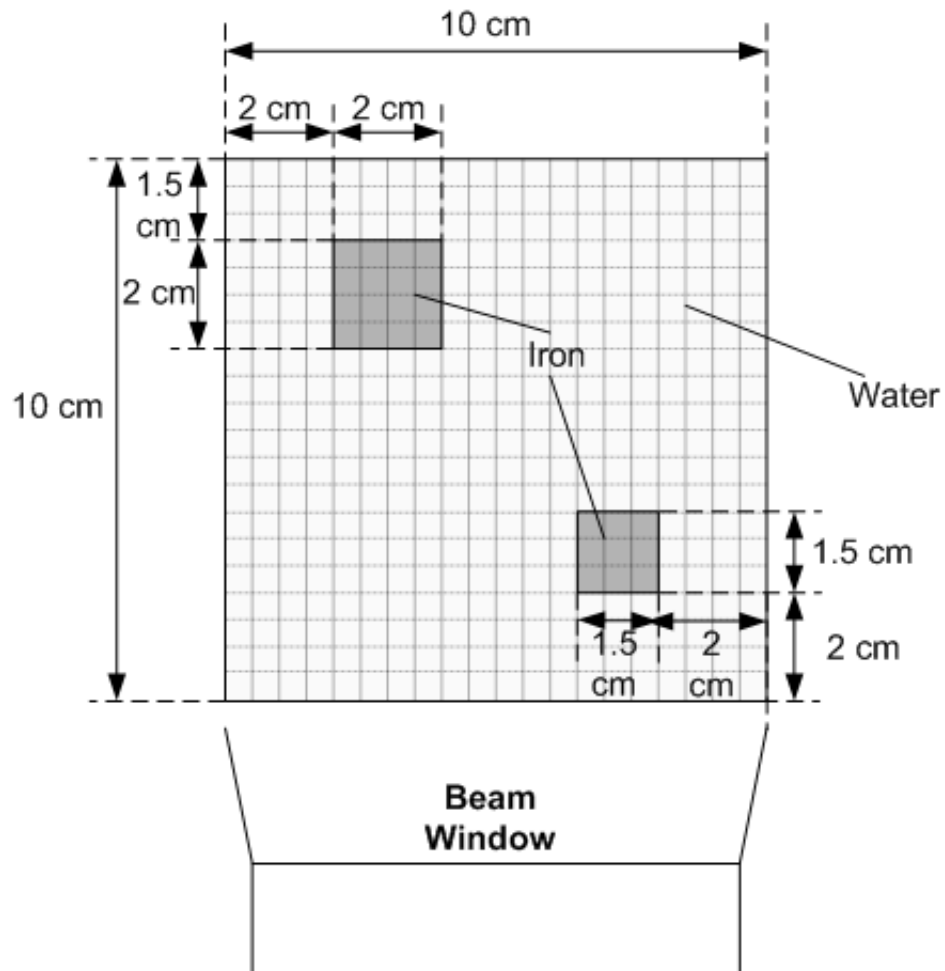
Fig. V.7: Schematic diagram of the two-inclusion problem.

process. The overall objective function has been reduced by a factor of 10^6 after 1000 iterations.

By only analyzing the data (including $\Sigma_t, \Sigma_s, \Sigma_{tr}, g$), we are still not be able to tell the type of inclusion material in the problem. Next we proceed to finish the problem with heuristic optimization methods.

Fig. V.10 shows the result from the cell grouping process in this problem. The numbers and colors in the figure denote different regions. Since we have no clue to

Fig. V.8: Transport cross section (Σ_{tr}) distribution obtained from deterministic CG based iterative search scheme for the two-iron problem. (a) The real Σ_{tr} (background is water and square inclusion is iron). (b) Initial guess for Σ_{tr}. (c) and (d) are results after 100 and 1000 iterations, respectively.

tell the two inclusions are the same material or not in this stage, we use different region number to identify them separately.

We carry out the same material restriction and stochastic optimization process as we described for the single-inclusion test problem. We present the material distribution results of this problem in Fig. V.11 and quantitatively assess the results in Table V.3.
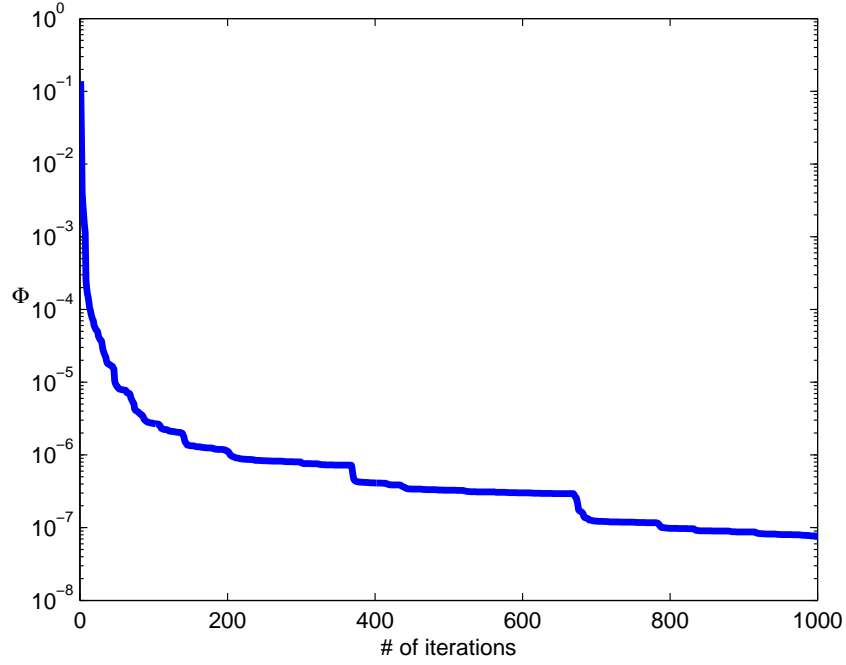
Fig. V.9: The objective function changes after each iteration for the two-inclusion problem.

Table V.3: Inclusions location and areas comparison for two-inclusion problem.

Parameter		Material	X-center (cm)	Y-center (cm)	Area (cm^2)
Inclusion 1	Actual	Iron	3.00	7.50	4.00
	Opt. Result	Iron	2.95	7.37	4.25
Inclusion 2	Actual	Iron	7.25	2.75	2.25
	Opt. Result	Iron	7.29	2.66	2.19

Fig. V.11 is the best material distribution selected after 100 random guesses for each candidate inclusion material in each inclusion region. (There were a total of 4x4x100=1600 forward transport calculations performed in this stage.) The selection
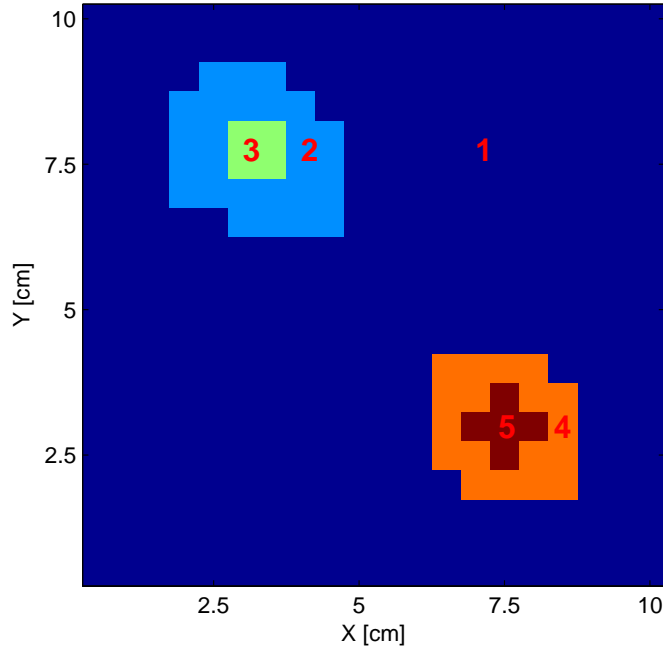
Fig. V.10: Different regions identified by the cell grouping process for the two-inclusion problem. (Color in this figure denotes region only, not any particular cross-section value.)

is based on the criterion that the object function it yields is lowest. The quantitative results shown in Table V.3 demonstrate that the algorithm successfully finds the material composition of each inclusion, accurately determines the area (mass) of each, and accurately determines each location.

V.D   More Model Problems

In this section, we present three more problems with similar configurations. The schematic diagram of these problems can be seen in Fig. V.12 and the geometric configuration to these model problems is list in Table V.4. These problems are designed to find the limits of our methodology's ability to find small inclusions deeply buried in optically thick scattering media. We use the same materials as in previous
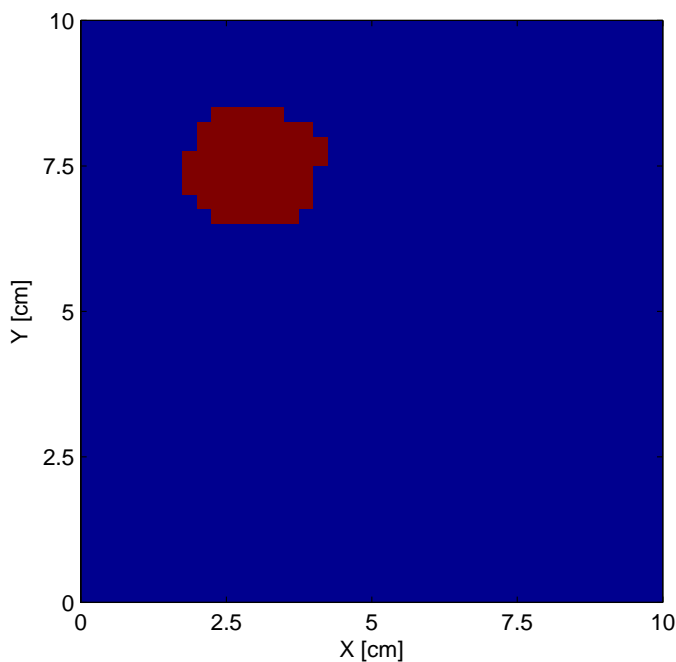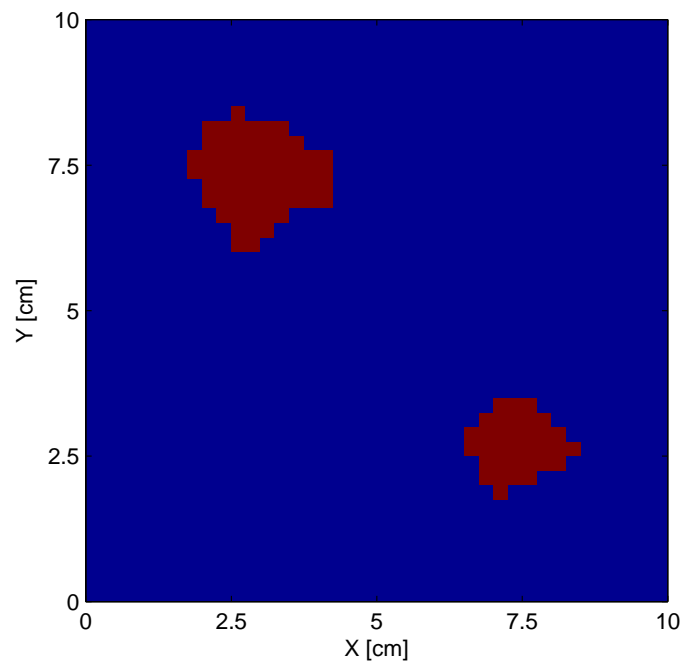
Fig. V.11: Results from the heuristic optimization in two-inclusion problem: Material distribution from the stochastic heuristic optimization after 100 iterations. (Color in this figure denotes material only, not any particular cross-section value.)

model test problems (water and iron), but we increase thickness and decrease feature size until the methodology fails.
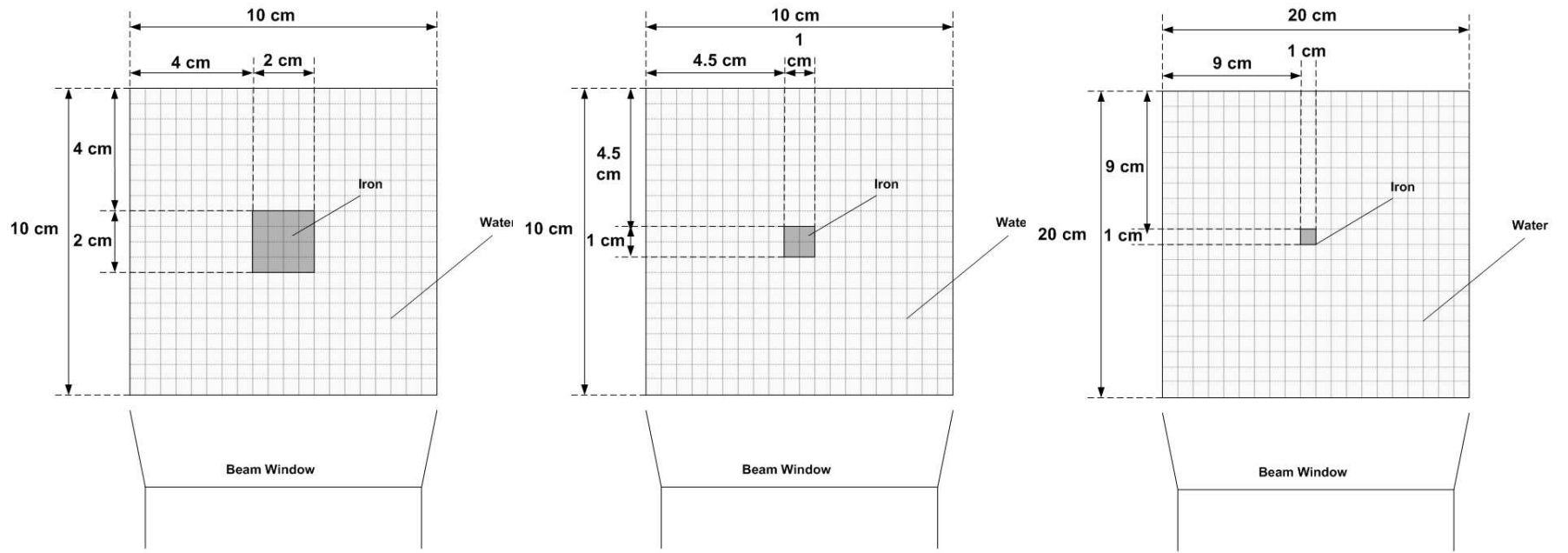
(a) Model Problem 3   (b) Model Problem 4   (c) Model Problem 5

Fig. V.12: Schematic diagram of three more model problems.

Table V.4: Geometry configuration comparison for model problems 3 - 5.

Problem	Model Problem 3	Model Problem 4	Model Problem 5
Water Area (cm^2)	10×10	10×10	20×20
Iron Area (cm^2)	2×2	1×1	1×1

The corresponding deterministic optimization results for Σ_{tr} (transport cross section) distribution for each model problem is illustrated in Fig. V.13. These results were obtained after 500 gradient-based iterations.

Relatively, the cross section distribution gained in MP3 has stronger contrast than the one in MP4. This is reasonable because the inclusion area in MP4 is smaller and more thoroughly hidden behind the background material. The result gained in MP5 almost has flat distribution which indicates that our CG based method actually failed in this case to find a clear indication of an included object. The depth of the water in front of the iron is almost 10 times of the depth of the iron itself, with the result that the exiting radiation has little or no information from which to infer the existence of the iron.

The next step in our approach is to perform cell grouping based on the information we gained in the first stage. Results are given in Fig. V.14. Results are reasonable in the first two problems (MP3 and MP4), but in model problem 5, the cell grouping result are not consistent with the actual configuration, for reasons already discussed.

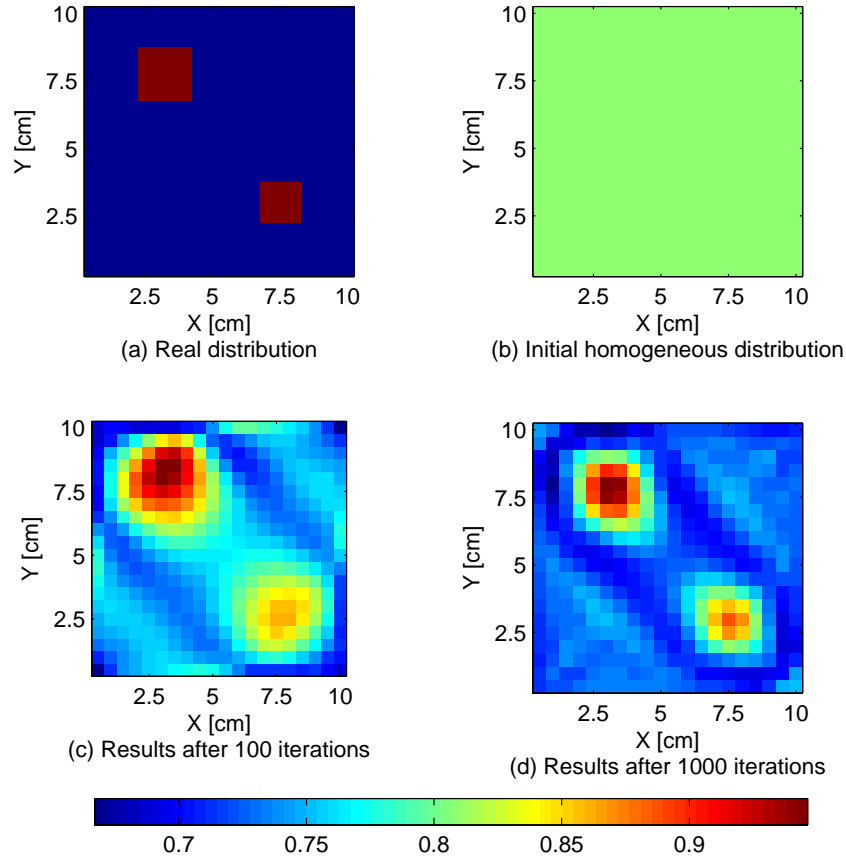(a) Results for MP3   (b) Results for MP4   (c) Results for MP5
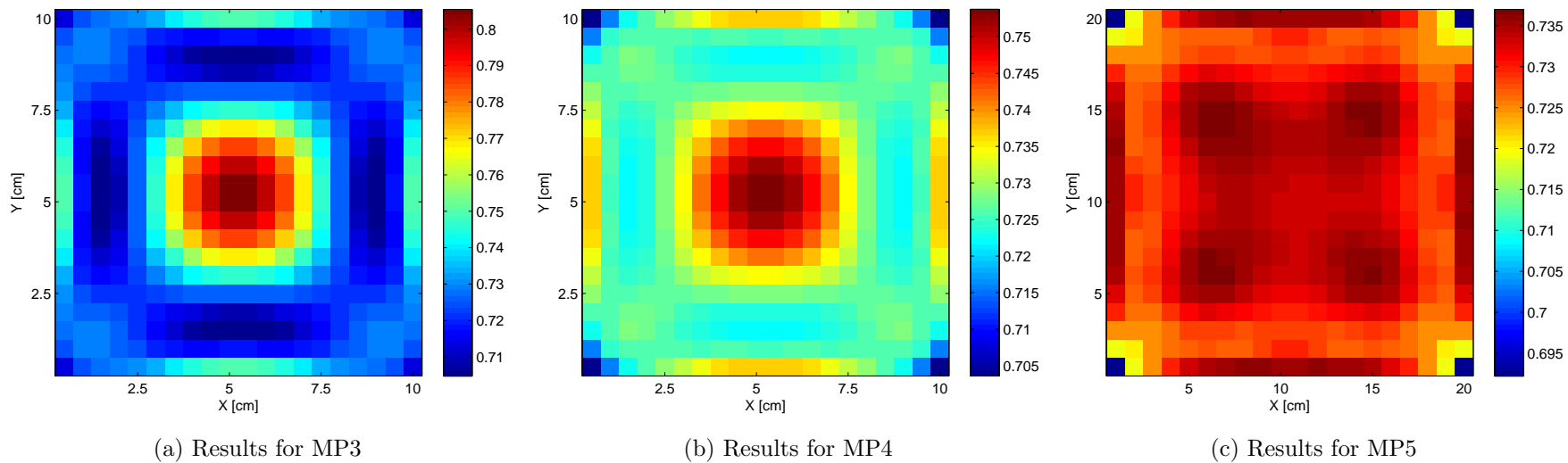
Fig. V.13: Transport cross section (Σ_{tr}) distribution obtained from deterministic CG-based iterative search scheme for model problem 3 - 5 after 500 iterations.
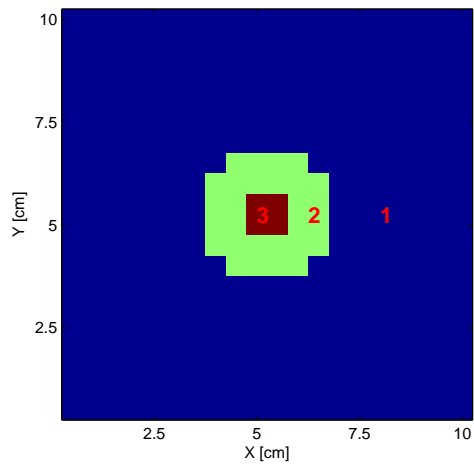
(a) Cell grouping results for MP3   (b) Cell grouping results for MP4   (c) Cell grouping results for MP5
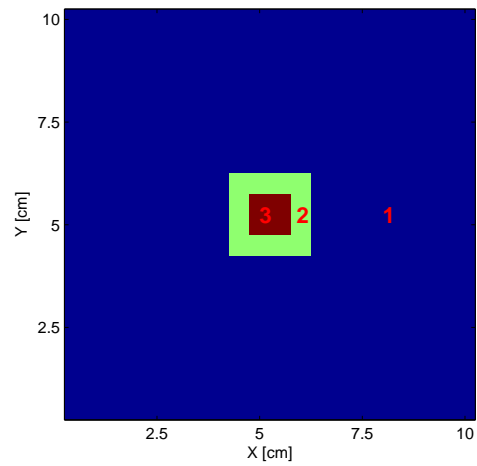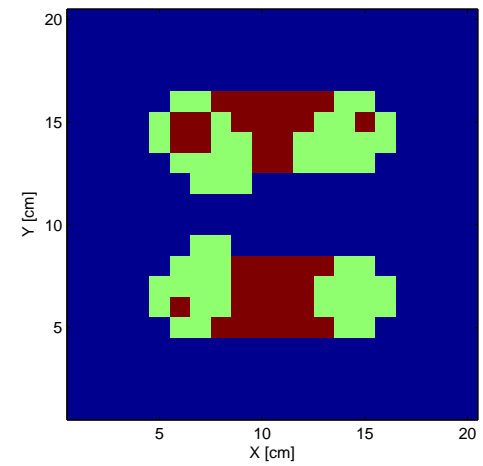
Fig. V.14: Different regions identified by the cell grouping process for model problem 3 - 5.

Need to note here that we actually improve the cell grouping result by adjusting the parameters in the cell grouping criterion (see details in section D of Chapter IV). In the model problems in previous section, we set the parameters $\alpha = 0.8$, $\beta = 0.2$, for MP3 and MP5 we set $\alpha = 0.95$, $\beta = 0.6$ and for MP2 we set $\alpha = 0.95$, $\beta = 0.8$, which means we use more rigor standard to determine the internal and interface region in the cell grouping process in these new model problems. In our proposed approach, these parameters (or completely different cell-grouping criteria) would be available to the analyst as he/she attempted to use all available tools to obtain a solution to the inverse problem.

For model problem 3 and 4, after we perform material restriction algorithm to select the candidate materials from MCL, we find that we gain the exact the same results as we see in the previous model problems (model problem 1 and 2), which is that region 1 was always chosen to be water and the inclusion could be any one of four different materials: iron, water, paraffin, natural uranium. Based on this prior knowledge, we proceed to process the problem with stochastic optimization and the results yielded are presented in the next paragraphs.

The corresponding stochastic optimization results for model problem 3 is shown in Fig. V.15, with quantitative results shown in Table V.5.

Need to emphasize here that at this time we actually gain perfect material distribution in this model problem after only 10 iterations in the stochastic optimization process. This is mainly because that we incorporate a rectangular shape based search algorithm into the combinatorial optimization process at this stage. In each iterate we start with a solution with the hypothesis that the shape of the inclusion is a rectangular. Our algorithm is also able to choose alternative randomly selected combinatorial solution if the objective function come out with the rectangular solution is higher.

We gained perfect material distribution in this model problem after only 10 iterations in the stochastic optimization process. This is because we instructed the
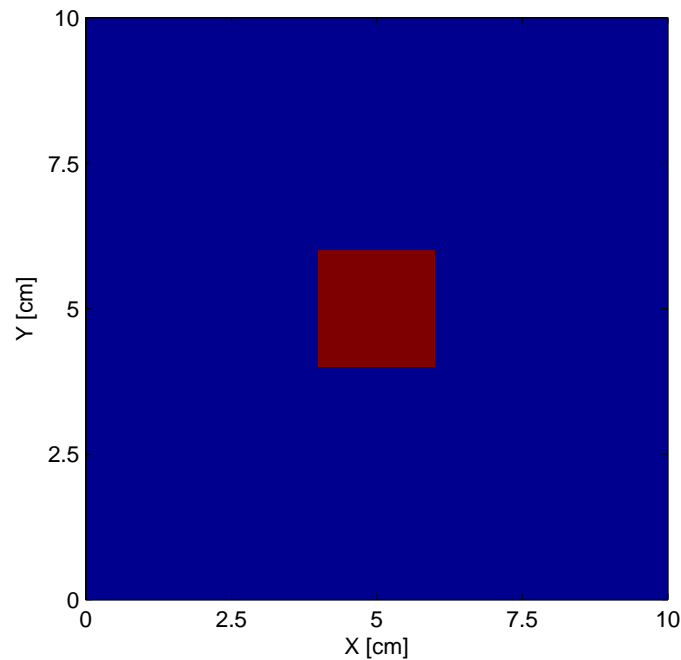
Fig. V.15: Material distribution result from the heuristic optimization for model problem 3 based on the cell grouping results in Fig. V.14(a)

stochastic search algorithm to consider only rectangular shapes for the interior material. This illustrates the power of our overall approach, which allows the user to test hypotheses (such as "the inclusion is rectangular") and quickly determine whether a hypothesis yields a small objective function, In this case it does. If the best objective function that resulted from the rectangular hypothesis were too large, then the analyst would relax this and search for more complicated shapes, as we demonstrated in previous model problems.

The corresponding stochastic optimization results for model problem 4 is shown in Fig. V.16, with quantitative results in Table V.6.

Once again we gain the perfect result for this model problem after once again instructing the algorithm to search first for a rectangular inclusion. Note that this restriction dramatically reduces the number of possible material configurations that

Table V.5: Inclusion location and area comparison for model problem 3.

Parameter	Actual [Fig. V.12(a)]	Opt. Result [Fig. V.15]
Material	Iron	Iron
X-center (cm)	5.0	5.0
Y-center (cm)	5.0	5.0
Area (cm^2)	4.0	4.0
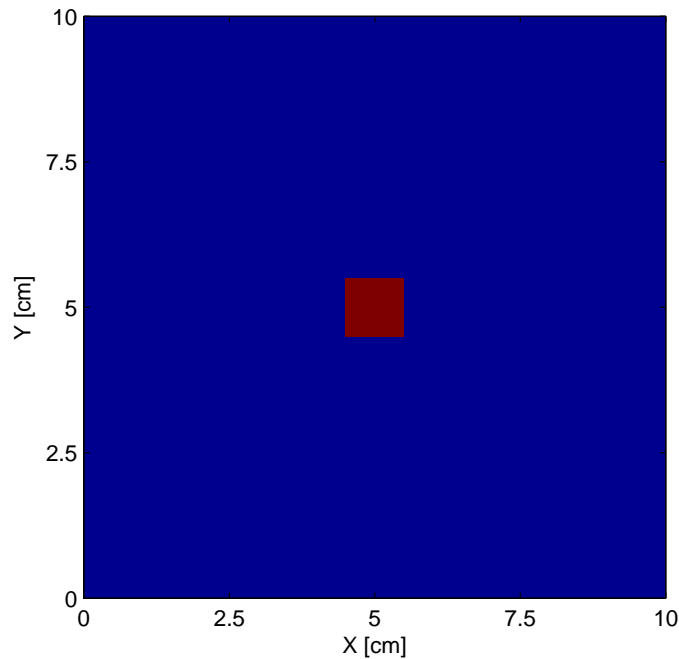
Fig. V.16: Material distribution result from the heuristic optimization for model problem 4 based on the cell grouping results in Fig. V.14(b)

satisfy the cell-grouping results. After approximately 50 iterations, the algorithm gives us the perfect result to the problem.

The model problem 5 is obviously more difficult. Cell grouping result of this problem yielded from our algorithm is illustrated in Fig. V.14(c), which demonstrated

Table V.6: Inclusion location and area comparison for model problem 4.

Parameter	Actual [Fig. V.12(b)]	Opt. Result [Fig. V.16]
Material	Iron	Iron
X-center (cm)	5.0	5.0
Y-center (cm)	5.0	5.0
Area (cm^2)	1.0	1.0

faulty characteristic region distribution comparing to our real model problem. We can imagine that if we continue to process this problem with the same methodology as we presented in the previous chapters, we would eventually obtain totally false optimization result. However, after performing material restriction process to each sub-region in this model problem, our algorithm indicates the background material - water - has been overwhelming favorable to each region, therefore we have reasons to state that the optimal material distribution yield from our methodology for MP5 is water everywhere. Though this result is not the correct one for this case, the approximately flat distribution of the cross section yielded from the first optimization stage prohibits us from knowing more details inside the object. Thus we find that given the detection information that we have postulated (with detectors that are not collimated, for example), the combination of optical thickness (approximately 14 mean free paths) and small object size (1/20th of the problem diameter) makes MP5 too difficult for our methodology. The methodology fails at the first step, in which the gradient-based search does not find any significant variation in the inferred cross section as a function of position in the object.

V.E Summary of Chapter V

In this chapter we have presented computational results from applying our new inverse-problem strategies to a set of neutron tomographic model problems. The results illustrate the efficiency and advantages of our systematic approach to inverse transport problems. We purposefully chose the objects in the our test problems to be optically thick with highly scattering materials (water and iron). The first model problem has one iron inclusion embedded in water while the second one has two iron inclusions embedded in different places of the object. The third, fourth, and fifth model problems are similar except that each one is more difficult than the previous. Difficulty is increased by reducing the size of the iron inclusion, increasing the thickness of the water object, or both.

In the first four model problems, the gradient-based deterministic optimization successfully reduces the objective function to a relatively low value and identifies regions that are likely to have different cross sections. However, it is not capable of identifying the material type or the size of the inclusions. The fifth problem is so optically thick and highly scattering, with such a small inclusion, that the gradient-based algorithm cannot identify a region with a different cross section.

The optimization methodology that we propose in this research can provide significantly improved results compared to previous methods, for problems that are optically thick and highly scattering. The cell grouping process incorporates the cells with approximately the same cross sections (as found in the gradient-based search stage) into regions and divides the object into background, inclusion, and interface regions. The material restriction process greatly reduces the material search space in each region. The stochastic-based heuristic optimization process finally identifies the exact material type of each region and quantitatively tells the area and location of each inclusive region. The results that our algorithms produce for the model problems in this chapter are strikingly accurate, are vastly better than can be achieved through deterministic searches, and are achieved with dramatically lower

computational cost than would be incurred with standard stochastic optimization procedures.

CHAPTER VI
SUMMARY AND RECOMMENDATIONS

VI.A   Summary

We have introduced some advances in inverse transport methods and applied them to 2D neutron tomography problems. We are interested in problems that are notoriously difficult for inverse algorithms: problems that are optically thick and highly scattering and whose exiting radiation is therefore dominated by scattered particles. Our main goal is to employ multiple steps that work together to dramatically reduce the difficulty of the combinatorial optimization problem that ultimately produces an estimate of the material distribution in the object being investigated. Our results indicate that we have achieved this goal.

Results from a simple model problem in Chapter II show that direct (analytic) tomography based on filtered back projection (FBP) fails to infer the material distribution within an object that is optically thick and whose exiting radiation has a dominant scattering component. This is true even in the case of collimated sources and collimated detectors, and it is true even for methods that are designed to find only the interfaces between materials (and not their cross sections). We conclude that for the class of problems we address, we can obtain little or no useful information from these direct methods. We therefore turn to methods that seek to minimize an objective function, a function that quantifies the difference between measured results and the results that would be obtained from a given guess for the unknown object's configuration.

Results from the same simple model problem in Chapter III show that gradient-based deterministic optimization methods can produce helpful information about optically thick, highly scattering objects. We introduce some techniques to improve the gradient-based search, including a variable-change technique that converts the usual constrained optimization problem into an unconstrained one. However, we

still encounter many defects associated with the methods themselves in this stage. Deterministic minimization algorithms can get stuck in local minima. They can obtain cross sections that do not match a real material. The dimension of their search space grows rapidly as the fidelity of the transport model increases. These difficulties lead us to move beyond gradient-based minimization techniques and to develop more powerful and efficient techniques. We ultimately devised the following general strategies:

1. Use an inexpensive forward-transport model with a gradient-based search algorithm to gain helpful information about the problem. The inexpensive model could, for example, use only a small number of energy groups, a relatively coarse spatial grid, low-order anisotropic scattering, and/or possibly diffusion instead of transport.

2. Use the information from the first step to group cells that are likely to have the same material (even though this material may be unknown) into "material regions". Some cells may fall into "interface regions" that are spatially between "material regions". Cells in such regions are later presumed likely to contain the same material as one of the bounding material regions.

3. Use prior knowledge or hypothesis to create a library of candidate materials. The final search procedure will consider materials only from this library.

4. Exploit hypotheses that constrain the internal structure of the object. For example, the analyst might ask the algorithm to look for a single one-material region embedded in a homogeneous background.

5. Employ a stochastic-based heuristic optimization method to search for a material distribution that satisfies the constraints imposed by previous steps. For each trial to be tested, each cell is assigned the cross sections from a real material from the candidate library. Each cell in an interface region is assigned the

material of one of its bounding regions, and the interface is required to conform to the analyst's hypotheses. Taken together, these constraints dramatically reduce the dimension of the search space.

Chapter IV develops these strategies and presents concrete examples of algorithmic implementations of each of them for a family of neutron-tomography problems. Chapter V applies these algorithms to optically thick, highly scattering test problems. Results are excellent. Our hierarchical step-by-step approach correctly identifies each material in the test problems and very accurately finds the locations and masses of each embedded object in the larger overall object. The computational effort required for this is modest because our strategies eliminate configurations that do not conform to what was learned in previous stages or to the constraints imposed by the analyst.

VI.B   Recommendations for Future Work

Though our simple implementation of our general strategies has worked well for the problems we have considered, our work leaves room for exploration and innovation that could improve on what we have shown and expand its applicability.

We have ignored the issues of measurement noise and model error, both of which must be addressed in any practical method. There are proven methods for addressing these issues, but it remains to be conclusively demonstrated that they can be employed within

In our implementation of the deterministic search that forms the first stage of our method we rely on the gradient of the objective function - its derivative with respect to each of the unknown cross-section parameters in each cell. This involves the construction and manipulation of matrices (whose elements are partial derivatives of various quantities with respect to other quantities). This process avoids the explicit calculation of an adjoint solution, but it can be computationally costly. A possibly

fruitful area of future investigation is whether an explicit adjoint calculation could be more computationally efficient. The answer could be problem-dependent.

Regarding the stochastic based heuristic optimization stage, in our testing we have made simple choices for constraints and biases; these could probably be improved and placed on firmer theoretical footing. The same is true of our algorithms for restricting materials based on results from the deterministic search. In practical applications the initial deterministic search phase may use a crude few-group model and thus produce few-group cross sections, but each material is actually characterized by energy-dependent or many-group cross sections. In the absence of known weighting spectra it is not obvious how to compare the few-group cross sections from the deterministic search with the real material cross sections. This question would benefit from further research.

Finally, an intriguing area for future work could be the application and extension of our general strategies to a different kind of highly scattering problem (for example, medical diagnosis using optical wavelengths). There are different kinds of prior knowledge and hypotheses that can be exploited in such different applications, and it would be interesting to see whether their exploitation provides the dramatic quantitative improvements that we have seen in our example neutron-tomography problems.

REFERENCES

[1] W. S. Charlton. Scattered neutron tomography based on a neutron transport inverse problem. Proposal for NEER Program, 2003.

[2] J. P. Barton. Contrast sensitivity in neutron radiography. *Appl. Mater. Res*, 4(2):90–96, 1965.

[3] J. M. Ollinger. Model-based scatter correction for fully 3D PET. *Physics in Medicine and Biology*, 41:153–176, 1996.

[4] H. Joo and S. Glickstein. Development of a scattering probability method for accurate vapor fraction measurements by neutron radiography. *Nuclear Instruments and Methods in Physics Research Section A*, 424:172–176, 1999.

[5] A. C. Kak and M. Slaney. *Principles of Computerized Tomographic Imaging*. IEEE Press, Piscataway, NJ, 1987.

[6] G. T. Herman. *Image Reconstruction from Projections*. Academic Press, Salt Lake City, UT, 1980.

[7] A. Markoe. *Analytic Tomography*. Cambridge University Press, West Nyack, NY, 2006.

[8] D. G. Luenberger. *Optimizatioin by Vector Space Methods*. John Wiley & Sons, New York, 1969.

[9] L. E. Scales. *Introduction to Non-Linear Optimization*. Springer-Verlag, New York, 1985.

[10] S. Boyd and L. Vandenberghe. *Convex Optimizaiton*. Cambridge University Press, West Nyack, NY, 2004.

[11] J. J. Duderstadt and L. J. Hamilton. *Nuclear Reactor Analysis*. John Wiley & Sons, New York, 1976.

[12] E. E. Lewis and W. F. Miller Jr. *Computational Methods of Neutron Transport*. John Wiley & Sons, New York, 1984.

[13] W. M. Stacey. *Nuclear Reactor Physics*. John Wiley and Sons, New York, 2001.

[14] E. I. Vainberg, I. A. Kazak, and V. P. Kurozaev. Reconstruction of the internal three-dimensional structure of objects based on real-time internal projections. *Soviet J. Nondestructive Testing*, 17:415–423, 1981.

[15] K. T. Smith and F. Keinert. Mathematical foundations of computed tomography. *Applied Optics*, 24:3950–3957, 1985.

[16] P. Kuchment, K. Lancaster, and L. Mogilevskaya. On local tomography. *Inverse Problems*, 11:571–589, 1995.

[17] A. Faridani. Introduction to the mathematics of computed tomography. *Inside Out: Inverse Problems, MSRI Publications*, 47, 2003.

[18] J.C. Domanus, editor. *Practical Neutron Radiography*. Kluwer Academic Publishers, Dordrecht, Netherlands, 1992.

[19] M. Zanarini, P. Chirco, M. Rossi, G. Baldazzi, and E. Querzola et al. Evaluation of hydrogen content in metallic samples by neutron computed tomography. *IEEE Transactions on Nuclear Science*, 42(4):580–584, 1995.

[20] E. Svab, M. Balasko, and F. Korosi. Dynamic neutron radiography in petrophysical application. *Physica B*, 276:916–917, 2000.

[21] N. Takenaka, H. Asano, T. Fujii, M. Mizubata, and K. Yoshii. Application of fast neutron radiography to three-dimensional visualization of steady two-phase flow in a rod bundle. *Nuclear Instruments and Methods in Physics Research Section A*, 424:73–76, 1999.

[22] G. Bayon. Present application of neutron radiography in France. *Nuclear Instruments and Methods in Physics Research Section A*, 424:92–97, 1999.

[23] R. Wacha, V. Crispim, C. Lage, and J. Lopesa. Neutron radiography applied to the microorganisms detection. *Radiation Measurements*, 32:159–162, 2000.

[24] B. E. Allman, P. J. McMahon, K. A. Nugent, D. Paganin, and D. L. Jacobson et al. Phase radiography with neutrons. *Nature*, 408:158–159, 2000.

[25] H. Berger. *Radiography, Methods, Capabilities and Applications*. Elsevier, New York, 1965.

[26] H. Jiang, K. D. Paulsen, and U. L. Osterberg. Optical image reconstruction using DC data: Simulations and experiments. *Journal of the Optical Society of America A*, 13:253–266, 1995.

[27] A. J. Davies, D. B. Christianson, L. Dixon, R. Roy, and P. van der Zee. Reverse differentiation and the inverse diffusion problem. *Advances in Engineering Software*, 28:217–221, 1997.

[28] Z. Zhou, R. M. Leahy, and J. Qi. Approximate maximum likelihood hyperparameter estimation for Gibbs priors. *IEEE Transactons on Image Processing*, 6(6):844–861, 1997.

[29] S. R. Arridge and M. Schweiger. A gradient-based optimization scheme for optical tomography. *Optics Express*, 2(6):213–226, 1998.

[30] S.S. Saquib, C. A. Bouman, and K. Sauer. ML parameter estimation for Markov random fields with applications to Bayesian tomography. *IEEE Transactions on Image Processing*, 7(7):1029–1040, 1998.

[31] O. Dorn. A transport-backtransport method for optical tomography. *Inverse Problems*, 14:1107–1130, 1998.

[32] K. M. Hanson, G. S. Cunningham, and S. S. Saquib. Inversion based on complex computational simulations. In E. Coyle and G. Adams, editors, *Proceedings of IEEE Nonlinear Signal and Image Processing Workshop*, Piscataway, NJ, 1998.

[33] A. H. Hielscher, A. D. Klose, and K. M. Hanson. Gradient-based iterative image reconstruction scheme for time-resolved optical tomography. *IEEE Transactions on Medical Imaging*, 18(3):262–270, 1999.

[34] N.J. McCormick. Inverse problems for biomedical characterization and imaging. In *Proceedings of 3rd Int. Conf. on Inverse Problems in Engineering: Theory and Practice*, Port Ludlow, Washington, June 13-18, 1999.

[35] A. D. Klose and A. H. Hielscher. Iterative reconstruction scheme for optical tomograpy based on the equation of radiative transfer. *Medical Physcis*, 26(8):1698–1706, 1999.

[36] A. D. Klose and A. H. Hielscher. Optical tomography using the time-independent equation of radiative transfer - part 1: Forward model. *J. Quantitative Spectroscopy & Radiative Transfer*, 72:691–713, 2002.

[37] A. D. Klose and A. H. Hielscher. Optical tomography using the time-independent equation of radiative transfer - part 2: Inverse model. *J. Quantitative Spectroscopy & Radiative Transfer*, 72:715–732, 2002.

[38] S. Kirkpatrick, Jr. C. D. Gelatt, and M. P. Vecchi. Optimization by simulated annealing. *Science*, 220(4598):671–680, 1983.

[39] W. E. Smith, H. H. Barrett, and R. G. Paxman. Reconstruction of objects from coded images by simulated annealing. *Optics Letters*, 8(4):199–201, 1983.

[40] W. E. Smith, R. G. Paxman, and H. H. Barrett. Applications of simulated annealing to coded-aperture design and tomographic reconstruction. *IEEE Transactions on Nuclear Science*, 32:758–761, 1985.

[41] P. Carnevali, L. Coletti, and S. Patarnello. Image processing by simualted annealing. *IBM Journal of Research and Development*, 29(6):569–579, 1985.

[42] H. Haneishi, T. Masuda, N. Ohyama, and T. Honda. Three-dimensional blood vessel reconstruction by simulated annealing. *Optics Letters*, 14(20):1095–1097, 1989.

[43] K. A. Girodias, H. H. Barrett, and R. L. Shoemaker. Parallel simualted annealing for emission tomography. *Physics in Medicine and Biology*, 36(7):921–938, 1991.

[44] C. Ortiz-Aleman, R. Martin, and J. C. Gamio. Reconstruction of permittivity images from capacitance tomography data by using very fast simulated annealing. *Measurement Science and Technology*, 15:1382–1390, 2004.

[45] R. Olmi, M. Bini, and S. Priori. A genetic algorithm approach to image reconstruction in electrical impedance tomography. *IEEE Transactions on Evolutionary Computation*, 4(1):83–88, 2000.

[46] H. C. Kim, D. C. Moon, M. C. Kim, S. Kim, and Y. J. Lee. Improvement in EIT image reconstruction using genetic algorithm. In *Proceedings of the American Control Conference*, pages 3858–3863, Anchorage, AK, May 8-10, 2002.

[47] C. Ortiz-Aleman, R. Martin, J. C. Gamio, and A. Nicolas. Applications of simulated annealing and genetic algorithms to the reconstruction of electrical permittivity images in capacitance tomography. In *Proceedings of 3rd World Congress on Industrial Process Tomography*, pages 794–798, Banff, Canada, Sept. 2-5, 2003.

[48] C. Mou, L. Peng, D. Yao, and D. Xiao. Image reconstruction using a genetic algorithm for electrical capacitance tomography. *Tsinghua Science and Technology*, 10(5):587–592, 2005.

[49] H-C Kim, C-J Boo, and M-J Kang. Image reconstruction using genetic algorithm in electrical impedance tomography. pages 938–945. Part III, LNCS 4234, ICONIP 2006.

[50] L. Herault and R. Horaud. Figure-ground discrimination: A combinatorial optimizatioin approach. *IEEE Transactions on Pattern and Machine Intelligence*, 15(9):899–914, 1993.

[51] F. Glover and M. Laguna. Fundamentals of scatter search and path relinking. *Control and Cybernetics*, 29(3):653–684, 2000.

[52] A. Kuba, L. Rusko, L. Rodek, and Z. Kiss. Preliminary studies of discrete tomography in neutron imaging. *IEEE Transactions on Nuclear Science*, 52(1):380–385, 2005.

[53] J. Dedkova. Image reconstruction using combination determistic and stochatic method. *Piers Online*, 4(1):73–76, 2008.

[54] V. Scipolo. Scattered neutron tomography based on a neutron transport problem. Master's thesis, Texas A&M University, 2004.

[55] Z. Wu and M. L. Adams. Variable change technique applied in constrained inverse transport applications. American Nuclear Society (ANS) Summer Annual Meeting, San Diego, CA, June 13-17, 2010.

[56] J. R. Shewchuk. An introduction to the conjugate gradient method without the agonizing pain. unpublished paper, 1994.

[57] R. Brent. *Algorithms for Minimization without Derivatives*. Prentice-Hall, Upper Saddle River, NJ, 1973.

[58] J.F. Briesmeister, editor. *MCNP-A general Monte Carlo n-particle transport code*. LA-UR-03-1987, 2003. Version 5, LANL.

[59] E. R. Quinto. An introduction to x-ray tomography and Radon transforms. In *Proceedings of Symposia in Applied Mathematics*, volume 63, pages 1–23, 2006.

[60] F. Natterer. On the inversion of the attenuated Radon transform. *Numerische Mathematik*, 32:431–438, 1979.

[61] S. B. Colak, D. G. Papaioannou, G. W. 't Hooft, M. B. van der Mark, and H. Schomberg et al. Tomographic image reconstruction from optical projections in light-diffusing media. *Applied Optics*, 36(1):180–213, 1997.

[62] N. G. Gencer, Y. Z. Ider, and M. Kuzuoglu. Electrical impedance tomography using induced and injected currents. *Clinical Physics and Physiological Measurement*, 13:95–99, 1992.

[63] W. R. B. Lionheart. Boundary shape and electrical impedance tomography. *Inverse Problems*, 14:139–147, 1998.

[64] M. Soleimani. Electrical impedance tomography imaging using a priori ultrasound data. *BioMedical Engineering OnLine*, 5(8), 2006.

[65] E. I. Vainberg, I. A. Kazak, and M. L. Faingoiz. X-ray computerized back projection tomography with filtration by double differentiation: Procedure and information features. *Soviet J. Nondestructive Testing*, 17:415–423, 1985.

[66] A. Faridani, E. L. Ritman, and K. T. Smith. Local tomography. *SIAM Journal on Applied Mathematics*, 52:459–484, 1992.

[67] A. Faridani, D. V. Finch, E. L. Ritman, and K. T. Smith. Local tomography II. *SIAM Journal on Applied Mathematics*, 57:1095–1127, 1997.

[68] A. Faridani, K. A. Buglione, P. Huabsomboon, O. D. Iancu, and J. McGrath. Introduction to local tomography. *Contemporary Mathematics*, 278:29–47, 2001.

[69] W. J. T. Spyra, A Faridani, K. T. Smith, and E. L. Ritman. Computed tomographic imaging of the coronary arterial tree - use of local tomography. *IEEE Transactions on Medical Imaging*, 9:1–4, 1990.

[70] A. C. Kak. Computerized tomography with x-ray emission and ultrasound sources. In *Proceedings of the IEEE*, volume 67, pages 1245–1272, 1979.

[71] S. X. Pan and A. C. Kak. A computational study of reconstruction algorithms for diffraction tomography: Interpolation vs. filtered-backpropagation. *IEEE Transactions on Acoustic, Speech, and Signal Processing*, ASSP-31:1262–1275, 1983.

[72] F. B. Brown, J. E. Sweezy, and R. B. Hayes. Monte Carlo parameter studies and uncertainty analysis with MCNP5. 2004. LA-UR-04-0499, LANL.

[73] J. R. Lamarsh. *Introduction to Nuclear Reactor Theory*. Addison-Wesley Pub., New York, NY, 1966.

[74] R. Sanchez and N. J. McCormic. A review of neutron transport approximations. *Nuclear Science and Engineering*, 80:481–535, 1982.

[75] J. K. Shultis and R. E. Faw. *Radiation Shielding*. American Nuclear Society, Chicago, IL, 2000.

[76] K. D. Lathrop. Spatial differencing of the transport equation: Positivity vs. Accuracy. *Journal of Computational Physics*, 4:475–498, 1969.

[77] R. Barrett, M. Berry, T. F. Chan, J. Demmel, and J. Donato et al., editors. *Templates for the Solution of Linear Systems: Building Blocks for Iterative Methods.* SIAM, Philadelphia, PA, 2004.

[78] M. L. Adams and E. W. Larsen. Fast iterative methods for discrete-ordinates particle transport calculations. *Progress in Nuclear Energy*, 40(1):3–159, 2002.

[79] R. Sanchez and S. Santandrea. Symmetrization of the transport operator and Lanzcos' iterations. In *Proceedings of the 2001 International Meeting on Mathematical Methods for Nuclear Applications*, pages 9–13, 2001.

[80] B. Babaoglu. Application of biconjugate gradient stabilized method with spectral acceleration for propagation over terrain profiles. Master's thesis, The Institute of Engineering and Science of Bilkent University, Ankara, Turkey, 2003.

[81] G. S. Chen and R. D. Sheu. Application of two preconditioned generalized conjugate gradient methods to three-dimensional neutron and photon transport equations. *Progress in Nuclear Energy*, 45(1):11–23, 2004.

[82] H. A. Van Der Vorst. Bi-CGSTAB: A fast and smoothly converging variant of Bi-CG for the solution of nonsymmetric linear systems. *SIAM Journal on Scientific and Statistic Computing*, 13:631–644, 1992.

[83] P. Sonneveld. A fast Lanczos-type solver for nonsymmetric linear systems. *SIAM Journal on Scietific and Statistics Computing*, 10:36–52, 1989.

[84] F. S. Acton. *Numerical Methods That Work.* Mathematical Association of America, Washington DC, 1990.

[85] M. T. Hagan, H.B. Demuth, and M.H. Beale. *Neural Network Design.* PWS Publishing, Boston, MA, 1996.

[86] C. Charalambous. Conjugate gradient algorithm for efficient training of artificial neural networks. *IEEE Proceedings*, 139(3):301–310, 1992.

[87] J. E. Dennis and R. B. Schnabel. *Numerical Methods for Unconstrained Optimization and Nonlinear Equations.* Prentice-Hall, Englewood Cliffs, NJ, 1983.

[88] W. Arnoldi. The principle of minimized iterations in the solution of the matrix eigenvalue problem. *Quarterly of Applied Mathematics*, 9:17–29, 1951.

APPENDIX A

MCNP INPUT DECKS

MCNP Inputs for Model Problem 1

```
Detetor measurements for water-iron model problem 1
c Geometry sets up to match the exact transport solutions
c and test different tally type (F1, F2, F5, etc.)
c
c Cell cards
c
c #cell,#material,#density,#domain
11      1 -1.0 -55 u=1 imp:n=1
12      2 -7.874 -55 u=2 imp:n=1
13      0 -52 +51 -54 +53 -16 +17 u=6 lat=1 imp:n=1
        fill=-10:9 -10:9 0:0
        1 1 1 1 1 1 1 1 1 1 1 1 1 1 1 1 1 1 1 1
        1 1 1 1 1 1 1 1 1 1 1 1 1 1 1 1 1 1 1 1
        1 1 1 1 1 1 1 1 1 1 1 1 1 1 1 1 1 1 1 1
        1 1 1 1 1 1 1 1 1 1 1 1 1 1 1 1 1 1 1 1
        1 1 1 1 1 1 1 1 1 1 1 1 1 1 1 1 1 1 1 1
        1 1 1 1 1 1 1 1 1 1 1 1 1 1 1 1 1 1 1 1
        1 1 1 1 1 1 1 1 1 1 1 1 1 1 1 1 1 1 1 1
        1 1 1 1 1 1 1 1 1 1 1 1 1 1 1 1 1 1 1 1
        1 1 1 1 1 1 1 1 1 1 1 1 1 1 1 1 1 1 1 1
        1 1 1 1 1 1 1 1 1 1 1 1 1 1 1 1 1 1 1 1
        1 1 1 1 1 1 1 1 1 1 1 1 1 1 1 1 1 1 1 1
        1 1 1 1 1 1 1 1 1 1 1 1 1 1 1 1 1 1 1 1
        1 1 1 1 1 1 1 1 1 1 1 1 1 1 1 1 1 1 1 1
```

```
         1 1 1 1 2 2 2 2 1 1 1 1 1 1 1 1 1 1 1 1 1

         1 1 1 1 2 2 2 2 1 1 1 1 1 1 1 1 1 1 1 1 1

         1 1 1 1 2 2 2 2 1 1 1 1 1 1 1 1 1 1 1 1 1

         1 1 1 1 2 2 2 2 1 1 1 1 1 1 1 1 1 1 1 1 1

         1 1 1 1 1 1 1 1 1 1 1 1 1 1 1 1 1 1 1 1 1

         1 1 1 1 1 1 1 1 1 1 1 1 1 1 1 1 1 1 1 1 1

         1 1 1 1 1 1 1 1 1 1 1 1 1 1 1 1 1 1 1 1 1
c
1        0 1 -2 3 -4 17 -16 fill=6 imp:n=1
4        0 -32 -30 31 #1 imp:n=1
5        0 32:30:-31  imp:n=0


c
c Surface cards
c
c SURFACES OBJECT
1        px -5.0
2        px +5.0
3        py -5.0
4        py +5.0
*16      pz +1
*17      pz -1
30       pz +4
31       pz -4
32       cz 20
c
c SURFACES U=1
51       px 0.0
```

```
52        px 0.5

53        py 0.0

54        py 0.5

55        cz +20.0

c

c SURFACES FOR TALLY DIVIDER

100       px -5.0

101       px -4.5

102       px -4.0

103       px -3.5

104       px -3.0

105       px -2.5

106       px -2.0

107       px -1.5

108       px -1.0

109       px -0.5

110       px 0.0

111       px +0.5

112       px +1.0

113       px +1.5

114       px +2.0

115       px +2.5

116       px +3.0

117       px +3.5

118       px +4.0

119       px +4.5

120       px +5.0

c
```

```
200      py -5.0
201      py -4.5
202      py -4.0
203      py -3.5
204      py -3.0
205      py -2.5
206      py -2.0
207      py -1.5
208      py -1.0
209      py -0.5
210      py 0.0
211      py +0.5
212      py +1.0
213      py +1.5
214      py +2.0
215      py +2.5
216      py +3.0
217      py +3.5
218      py +4.0
219      py +4.5
220      py +5.0


c
c All the data cards
c
mode     n
c Materials
m1       1001 -0.111894 $water
```

```
        8016 -0.888106
m2      26000 -1.000000 $Iron
c Source
sdef    pos=0 -10 0 vec=0 1 0 erg=d2 y=-10 x=d3 z=d4
sp2     -2 2.5e-8
si3     h -7.08 7.08
sp3     d 0 1
si4     h -1 1
sp4     d 0 1
nps     1e7
prdmp   2j 1 1
print   -85 -110
c
c Tally card section
c
fq0 s c $change the output order for all tallies
c
c F1 Tally
c
c Tally along back surface
f11:n   4
fs11    -100 -101 -102 -103 -104 -105 -106 -107 -108 -109
        -110 -111 -112 -113 -114 -115 -116 -117 -118 -119 -120
sd11    (1 1 1 1 1 1 1 1 1 1 1 1 1 1 1 1 1 1 1 1 1 1 1)
c11     0 1
c Tally along left surface
f21:n   1
fs21    -200 -201 -202 -203 -204 -205 -206 -207 -208 -209
```

```
          -210 -211 -212 -213 -214 -215 -216 -217 -218 -219 -220
sd21     (1 1 1 1 1 1 1 1 1 1 1 1 1 1 1 1 1 1 1 1 1)
c21       0 1
c Tally along right surface
f31:n    2
fs31     -200 -201 -202 -203 -204 -205 -206 -207 -208 -209
          -210 -211 -212 -213 -214 -215 -216 -217 -218 -219 -220
sd31     (1 1 1 1 1 1 1 1 1 1 1 1 1 1 1 1 1 1 1 1 1)
c31        0 1
c
c F2 Tally
c
c Tally along back surface
f12:n    4
fs12     -100 -101 -102 -103 -104 -105 -106 -107 -108 -109
          -110 -111 -112 -113 -114 -115 -116 -117 -118 -119 -120
sd12     (1 1 1 1 1 1 1 1 1 1 1 1 1 1 1 1 1 1 1 1 1)
c12       1
c Tally along left surface
f22:n    1
fs22     -200 -201 -202 -203 -204 -205 -206 -207 -208 -209
          -210 -211 -212 -213 -214 -215 -216 -217 -218 -219 -220
sd22     (1 1 1 1 1 1 1 1 1 1 1 1 1 1 1 1 1 1 1 1 1)
c22       1
c Tally along right surface
f32:n    2
fs32     -200 -201 -202 -203 -204 -205 -206 -207 -208 -209
          -210 -211 -212 -213 -214 -215 -216 -217 -218 -219 -220
```

```
sd32    (1 1 1 1 1 1 1 1 1 1 1 1 1 1 1 1 1 1 1 1 1 1 1 1)
c32     1
c
c F5 Tally
c
c F5 tally along back surface (flux image radiography)
fir15:n 0 5.1 0 0 0 0 0 0 0 0 nd
c15    -1 1
fs15  -5 19i 5
c F5 tally along left surface (flux image radiography)
fir25:n -5.1 0 0 0 0 0 0 0 0 0 nd
c25    -1 1
fs25  -5 19i 5
c F5 tally along right surface (flux image radiography)
fir35:n 5.1 0 0 0 0 0 0 0 0 0 nd
c35    -1 1
fs35  -5 19i 5
```

<div align="center">MCNP_Pstudy Inputs for Model Problem 1</div>

```
Water-Iron model problem 1 clockwise rotate THETA degrees
c General input file for mcnp_pstudy
c
c @@@ dim = 180
c @@@ number = repeat dim
c @@@ THETA = ( (number-1)*360/dim )
c @@@ PLUS90 = ( 90 + THETA )
c @@@ MINUS90 = ( 90 - THETA )
c @@@ OPTIONS =  -jobdir /emchome/zeyunwu/mcnp/tomography \
```

```
c @@@              -case wi -inner -job wiinp
c
c Cell cards
11        1 -1.0 -55 u=1 imp:n=1
12        2 -7.874 -55 u=2 imp:n=1
13        0 -52 +51 -54 +53 -16 +17 u=6 lat=1 imp:n=1
          fill=-10:9 -10:9 0:0
          1 1 1 1 1 1 1 1 1 1 1 1 1 1 1 1 1 1 1 1
          1 1 1 1 1 1 1 1 1 1 1 1 1 1 1 1 1 1 1 1
          1 1 1 1 1 1 1 1 1 1 1 1 1 1 1 1 1 1 1 1
          1 1 1 1 1 1 1 1 1 1 1 1 1 1 1 1 1 1 1 1
          1 1 1 1 1 1 1 1 1 1 1 1 1 1 1 1 1 1 1 1
          1 1 1 1 1 1 1 1 1 1 1 1 1 1 1 1 1 1 1 1
          1 1 1 1 1 1 1 1 1 1 1 1 1 1 1 1 1 1 1 1
          1 1 1 1 1 1 1 1 1 1 1 1 1 1 1 1 1 1 1 1
          1 1 1 1 1 1 1 1 1 1 1 1 1 1 1 1 1 1 1 1
          1 1 1 1 1 1 1 1 1 1 1 1 1 1 1 1 1 1 1 1
          1 1 1 1 1 1 1 1 1 1 1 1 1 1 1 1 1 1 1 1
          1 1 1 1 1 1 1 1 1 1 1 1 1 1 1 1 1 1 1 1
          1 1 1 1 1 1 1 1 1 1 1 1 1 1 1 1 1 1 1 1
          1 1 1 1 2 2 2 2 1 1 1 1 1 1 1 1 1 1 1 1
          1 1 1 1 2 2 2 2 1 1 1 1 1 1 1 1 1 1 1 1
          1 1 1 1 2 2 2 2 1 1 1 1 1 1 1 1 1 1 1 1
          1 1 1 1 2 2 2 2 1 1 1 1 1 1 1 1 1 1 1 1
          1 1 1 1 1 1 1 1 1 1 1 1 1 1 1 1 1 1 1 1
          1 1 1 1 1 1 1 1 1 1 1 1 1 1 1 1 1 1 1 1
          1 1 1 1 1 1 1 1 1 1 1 1 1 1 1 1 1 1 1 1
c
```

```
1        0 1 -2 3 -4 17 -16 fill=6 imp:n=1

2        3 -0.001205 -5 17 -16 #1 imp:n=1

3        3 -0.001205 11 -12 13 -14 17 -16 #1 #2 imp:n=1

4        3 -0.001205 -32 -30 31 #1 #2 #3 imp:n=1

5        0 32:30:-31  imp:n=0


c Surface cards

c SURFACES OBJECT

1     2  px -5.0

2     2  px +5.0

3     2  py -5.0

4     2  py +5.0

5        cz 7.075

11       px -7.08

12       px 7.08

13       py -7.08

14       py 7.08

*16      pz +1

*17      pz -1

30       pz +4

31       pz -4

32       cz 20

c SURFACES U=1

51    2 px 0.0

52    2 px 0.5

53    2 py 0.0

54    2 py 0.5

55       cz +20.0
```

```
c SURFACES FOR TALLY DIVIDER

91        px -7.08

92        px -7.0

93        px -6.5

94        px -6.0

95        px -5.5

100       px -5.0

101       px -4.5

102       px -4.0

103       px -3.5

104       px -3.0

105       px -2.5

106       px -2.0

107       px -1.5

108       px -1.0

109       px -0.5

110       px 0.0

111       px +0.5

112       px +1.0

113       px +1.5

114       px +2.0

115       px +2.5

116       px +3.0

117       px +3.5

118       px +4.0

119       px +4.5

120       px +5.0

121       px 5.5
```

```
122      px 6.0

123      px 6.5

124      px 7.0

125      px 7.08


c All the data cards

mode     n

c clockwise rotate THETA degree

tr2*   0 0 0 THETA PLUS90 90 MINUS90 THETA 90 90 90 0

c Materials

m1      1001 -0.111894 $Water

        8016 -0.888106

m2      26000 -1.000000 $Iron

m3      6000 -0.000124 $ C(air)

        7014 -0.755268 $ N

        8016 -0.231781 $ O

        18000 -0.012827 $ Ar

c Source

sdef    pos=0 -10 0 vec=0 1 0 dir=1 erg=d2 y=-10 x=d3 z=d4

sp2     -2 2.5e-8

si3     h -7.08 7.08

sp3     d 0 1

si4     h -1 1

sp4     d 0 1

c Others

nps     1.5e6

prdmp  2j 1 1

c
```

```
c Surface Tally

c

c Tally along back surface

f11:n    14

fs11     -91 -92 -93 -94 -95

         -100 -101 -102 -103 -104 -105 -106 -107 -108 -109

         -110 -111 -112 -113 -114 -115 -116 -117 -118 -119 -120

         -121 -122 -123 -124 -125

sd11     (1 0.16 1 1 1 1

          1 1 1 1 1 1 1 1 1 1

          1 1 1 1 1 1 1 1 1 1

          1 1 1 1 0.16 1)

c11      0 1

fq11     s c
```

MCNP Inputs for Cross Section Evaluation

```
Calculate thermal cross section for water

c One-group thermal energy cross section generation

c Cell cards

11       1 -1.0 -55 u=1 imp:n=1

13       0 -52 +51 -54 +53 -30 +31 u=6 lat=1 imp:n=1

         fill=-10:9 -10:9 0:0

         1 1 1 1 1 1 1 1 1 1 1 1 1 1 1 1 1 1 1 1

         1 1 1 1 1 1 1 1 1 1 1 1 1 1 1 1 1 1 1 1

         1 1 1 1 1 1 1 1 1 1 1 1 1 1 1 1 1 1 1 1

         1 1 1 1 1 1 1 1 1 1 1 1 1 1 1 1 1 1 1 1

         1 1 1 1 1 1 1 1 1 1 1 1 1 1 1 1 1 1 1 1

         1 1 1 1 1 1 1 1 1 1 1 1 1 1 1 1 1 1 1 1
```

```
        1 1 1 1 1 1 1 1 1 1 1 1 1 1 1 1 1 1 1 1 1

        1 1 1 1 1 1 1 1 1 1 1 1 1 1 1 1 1 1 1 1 1

        1 1 1 1 1 1 1 1 1 1 1 1 1 1 1 1 1 1 1 1 1

        1 1 1 1 1 1 1 1 1 1 1 1 1 1 1 1 1 1 1 1 1

        1 1 1 1 1 1 1 1 1 1 1 1 1 1 1 1 1 1 1 1 1

        1 1 1 1 1 1 1 1 1 1 1 1 1 1 1 1 1 1 1 1 1

        1 1 1 1 1 1 1 1 1 1 1 1 1 1 1 1 1 1 1 1 1

        1 1 1 1 1 1 1 1 1 1 1 1 1 1 1 1 1 1 1 1 1

        1 1 1 1 1 1 1 1 1 1 1 1 1 1 1 1 1 1 1 1 1

        1 1 1 1 1 1 1 1 1 1 1 1 1 1 1 1 1 1 1 1 1

        1 1 1 1 1 1 1 1 1 1 1 1 1 1 1 1 1 1 1 1 1

        1 1 1 1 1 1 1 1 1 1 1 1 1 1 1 1 1 1 1 1 1

        1 1 1 1 1 1 1 1 1 1 1 1 1 1 1 1 1 1 1 1 1

        1 1 1 1 1 1 1 1 1 1 1 1 1 1 1 1 1 1 1 1 1
c
1       0 1 -2 3 -4 -30 31 fill=6 imp:n=1
2       3 -0.001205 -5 -30 31 #1 imp:n=1
3       3 -0.001205 11 -12 13 -14 -30 31 #1 #2 imp:n=1
4       3 -0.001205 -32 -30 31 #1 #2 #3 imp:n=1
5       0 32:30:-31  imp:n=0


c Surface cards
c SURFACES OBJECT
1       px -1.0
2       px +1.0
3       py -1.0
4       py +1.0
5       cz 1.415
```

```
11       px -1.42

12       px 1.42

13       py -1.42

14       py 1.42

30       pz +2

31       pz -2

32       cz 4

c SURFACES U=1

51       px 0.0

52       px 0.1

53       py 0.0

54       py 0.1

55       cz +20.0


c All the data cards

mode     n

c Materials

m1       1001 -0.111894    $water

         8016 -0.888106

c MT card to treat bounding effect for H,O

mt1      lwtr.60t

m2       26000 -1.000000  $Iron

m3       6000 -0.000124    $ C(air)

         7014 -0.755268    $ N

         8016 -0.231781    $ O

         18000 -0.012827   $ Ar

c Source

sdef     pos=0 -2 0 vec=0 1 0 dir=1 erg=d2 y=-2 x=d3 z=d4
```

```
sp2     -2 2.5e-8
si3     h -1.42 1.42
sp3     d 0 1
si4     h -2 2
sp4     d 0 1
c Others
nps     10000
prdmp   2j 1 1
c Tally 4 and its multiplication to compute one group cross sections
f4:n    1
sd4     1.
f14:n   1
sd14    1.
c
c Reaction number notification
c 1 total cross section
c 2 elastic cross section
c -2 absorption cross section
c Format: FMn (C M R)
c
fm14    (1 2 2) (1 2 -2) (1 2 1)
```

APPENDIX B

KRYLOV SUBSPACE ACCELERATION SCHEMES

To better describe the accelerating iterative schemes we are going to present, we treat the forward problem as to solve the linear equations in matrix form $Ax = b$, where A is taken as transport operator and b is the source term in the right hand side of the transport equation.

CG Method

The Conjugate Gradient (CG) method is an effective method for symmetric positive definite systems. It is the oldest and best known of the nonstationary methods discussed here. The method proceeds by generating vector sequences of iterates (i.e., successive approximations to the solution), residuals corresponding to the iterates, and search directions used in updating the iterates and residuals. Although the length of these sequences can become large, only a small number of vectors need to be kept in memory. In every iterate of the method, two inner products are performed in order to compute update scalars that are defined to make the sequences satisfy certain orthogonality conditions. On a symmetric positive definite linear system these conditions imply that the distance to the true solution is minimized in some norm. The pseudo-code for the Conjugate Gradient Method is given below:

$d_0 = r_0 = b - Ax_0$

Loop started

$\alpha_k = \dfrac{(r_k, r_k)}{(d_k, Ad_k)}$

$x_{k+1} = x_k + \alpha_k d_k$

$r_{k+1} = r_k - \alpha_k Ad_k$

Convergence check with $\|r_{k+1}\|_2$

$\beta_k = \dfrac{(r_{k+1}, r_{k+1})}{(r_k, r_k)}$

$$d_{k+1} = r_{k+1} + \beta_k d_k$$

Loop finished

Bi-CG Method

The Conjugate Gradient method is not suitable for non-symmetric systems because the residual vectors cannot be made orthogonal with short recurrences. The GMRES method retains orthogonality of the residuals by using long recurrences, at the cost of a larger storage demand. The Bi-Conjugate Gradient (Bi-CG) method takes another approach, replacing the orthogonal sequence of residuals by two mutually orthogonal sequences, at the price of no longer providing a minimization. The update relations for residuals in the Conjugate Gradient method are augmented in the Bi-CG method by relations that are similar but based on A^T instead of A. Instead of orthogonalizing each sequence, they are made mutually orthogonal, or "bi-orthogonal". Thus we update two sequences of residuals

$$r_{k+1} = r_k - \alpha_k A d_k, \quad \widehat{r_{k+1}} = \widehat{r}_k - \alpha_k A^T \widehat{d}_k$$

and two sequences of search directions

$$d_{k+1} = r_{k+1} + \beta_k d_k, \quad \widehat{d_{k+1}} = \widehat{r_{k+1}} + \beta_k \widehat{d}_k$$

The choices

$$\alpha_k = \frac{(\widehat{r}_k, r_k)}{\left(\widehat{d}_k, A d_k\right)}, \quad \beta_k = \frac{(\widehat{r_{k+1}}, r_{k+1})}{(\widehat{r}_k, r_k)}$$

ensure the bi-orthogonality relations

$$\widehat{r}_k^T r_l = \widehat{d}_k^T A d_l = 0, \quad if \quad k \neq l$$

Bi-CG method, like CG, uses limited storage but requires a multiplication with the coefficient matrix and with its transpose at each iterative step. The pseudo-code for the Preconditioned Bi-CG Method is given below:

$d_0 = r_0 = \widehat{d_0} = \widehat{r_0} = b - Ax_0$

Loop started

$\alpha_k = \dfrac{(\widehat{r_k}, r_k)}{\left(\widehat{d_k}, Ad_k\right)}$

$x_{k+1} = x_k + \alpha_k d_k$

$r_{k+1} = r_k - \alpha_k Ad_k$

$\widehat{r_{k+1}} = \widehat{r_k} - \alpha_k A^T \widehat{d_k}$

Convergence check $\|r_{k+1}\|_2$ *and* $\|\widehat{r_{k+1}}\|_2$

$\beta_k = \dfrac{(\widehat{r_{k+1}}, r_{k+1})}{(\widehat{r_k}, r_k)}$

$d_{k+1} = r_{k+1} + \beta_k d_k$

$\widehat{d_{k+1}} = \widehat{r_{k+1}} + \beta_k \widehat{d_k}$

Loop finished

CGS Method

In Bi-CG method, the residual vector r_k can be regarded as the product of r_0 and an kth degree polynomial in A, that is

$$r_k = P_k(A)r_0 \tag{B.1}$$

This same polynomial satisfies $\widehat{r_k} = P_k(A^T)\widehat{r_0}$ so that

$$\rho_i = (\widehat{r_k}, r_k) = \left(P_k(A^T)\widehat{r_0}, P_k(A)r_0\right) = \left(\widehat{r_0}, P_k^2(A)r_0\right) \tag{B.2}$$

This indicates that if $P_k(A)$ reduces r_0 to a smaller vector r_k, then it might be advantageous to apply this "contraction" operator twice, and compute $P_k^2(A)r_0$. Eq. (B.2) shows that the iteration coefficients can still be recovered from these vectors, and it turns out to be easy to find the corresponding approximations for x. This approach leads to the Conjugated Gradient Square (CGS) method [83]. The Conjugate Gradient Squared method is a variant of Bi-CG that applies the updating operations for the A-sequence and the A^T-sequences both to the same vectors. Ideally, this would double the convergence rate, but in practice convergence may be much more

irregular than for Bi-CG. A practical advantage is that the method does not need the multiplications with the transpose of the coefficient matrix. The pseudo-code for the CGS method is given below:

$u_0 = d_0 = r_0 = b - Ax_0$, and arbitrary choose $\widehat{r}$, (for example, let $\widehat{r} = r_0$)

Loop started

$\rho_k = (\widehat{r}, r_k)$, if $\rho_k = 0$, then method fails.

$\alpha_k = \dfrac{(\widehat{r}, r_k)}{(\widehat{r}, Ad_k)}$

$q_k = u_k - \alpha_k Ad_k$

Convergence check with $\|q_k\|_2$, *if small enough,* $x_{k+1} = x_k + \alpha_k d_k$ *and stop.*

$x_{k+1} = x_k + \alpha_k (u_k + q_k)$

$r_{k+1} = r_k - \alpha_k A (u_k + q_k)$

Convergence check with $\|r_{k+1}\|_2$

$\beta_k = \dfrac{(\widehat{r}, r_{k+1})}{(\widehat{r}, r_k)}$

$u_{k+1} = r_{k+1} + \beta_k q_k$

$d_{k+1} = u_{k+1} + \beta_k (q_k + \beta_k d_k)$

Loop finished

Bi-CGSTAB Method

The Bi-Conjugate Gradient Stabilized method (Bi-CGSTAB) was developed to solve non-symmetric linear systems while avoiding the often irregular convergence patterns of the Conjugate Gradient Squared method [82]. The Bi-Conjugate Gradient Stabilized method is a variant of Bi-CG, like CGS, but using different updates for the A^T-sequence in order to obtain smoother convergence than CGS. Instead of computing the CGS sequence $k \mapsto P_k^2(A)r_0$, Bi-CGSTAB computes $k \mapsto Q_k(A)P_k(A)r_0$ where $Q_k(A)$ is an kth degree polynomial describing a steepest descent update. Bi-CGSTAB requires two matrix-vector products and four inner products, i.e., two inner products more than Bi-CG and CGS. The pseudo code for the Preconditioned Bi-Conjugate Gradient Stabilized Method is given below:

$d_0 = r_0 = b - Ax_0$, and arbitrary choose $\widehat{r}$, (for example, let $\widehat{r} = r_0$)

Loop started

$\rho_k = (\widehat{r}, r_k)$, *if* $\rho_k = 0$, *then method fails.*

$\alpha_k = \dfrac{(\widehat{r}, r_k)}{(\widehat{r}, Ad_k)}$

$s_k = r_k - \alpha_k Ad_k$

Convergence check with $\|s_k\|_2$, *if small enough,* $x_{k+1} = x_k + \alpha_k d_k$ *and stop.*

$\omega_k = \dfrac{(s_k, As_k)}{(As_k, As_k)}$

$x_{k+1} = x_k + \alpha_k d_k + \omega_k s_k$

$r_{k+1} = s_k - \omega_k As_k$

Convergence check with $\|r_{k+1}\|_2$, *it is also necessary for* $\omega_k \neq 0$.

$\beta_k = \dfrac{(\widehat{r}, r_{k+1})}{(\widehat{r}, r_k)} \cdot \frac{\alpha_k}{\omega_k}$

$d_{k+1} = r_{k+1} + \beta_k (d_k - \omega_k Ad_k)$

Loop finished

GMRES Method

The Generalized Minimal Residual (GMRES) method is an extension of Minimal Residual (MINRES) method (which is only applicable to solve symmetric systems) to non-symmetric systems. Like MINRES, it generates a sequence of orthogonal vectors, but in the absence of symmetry this can no longer be done with short recurrences; instead, all previously computed vectors in the orthogonal l sequence have to be retained. For this reason, "restarted" versions of the method are used. GMRES method is designed to solve non-symmetric linear system. The most popular form of GMRES is based on the modified Gram-Schmidt procedure, and uses restarts to control storage requirements (See details in page 17 of [77]).

If no restarts are used, GMRES (like any orthogonalizing Krylov subspace method) will converge in no more than n steps (assuming exact arithmetic). Of course this is of no practical value when n is large; moreover, the storage and computational

requirements in the absence of restarts are prohibitive. Indeed, the crucial element for successful application of GMRES revolves around the decision of when to restart; that is, the choice of m as described in the implementation pseudo-code below.

In the Conjugate Gradient method, the residuals form an orthogonal basis for the space span $\{r_0, Ar_0, A^2r_0, \cdots\}$. In GMRES, this basis is formed explicitly:

$w_i = Av_i$

For k=1,$\cdots$, i

$\quad w_i = w_i - (w_i, v_k)\, v_k$

End

$v_{i+1} = \frac{w_i}{\|w_i\|}$

The reader may recognize this as a modified Gram-Schmidt orthogonalization. Applied to the Krylov sequence $\{A^k r_0\}$ this orthogonalization is called the "Arnoldi method" [88]. The inner product coefficients (w_i, v_k) and $\|w_i\|$ are stored in an upper Hessenberg matrix.

The GMRES iterates are constructed as

$$x_i = x_0 + y_1 v_1 + y_2 v_2 + \cdots + y_i v_i$$

where the coefficients y_k have been chosen to minimize the residual norm $\|b - Ax_i\|$. The GMRES algorithm has the property that this residual norm can be computed without the iterate having been formed. Thus, the expensive action of forming the iterate can be postponed until the residual norm is deemed small enough. The pseudo-code for the restarted GMRES(m) algorithm is given below:

Initial guess x_0

For j=1,2, $\cdots$

$\quad r = b - Ax_0$

$\quad v_1 = \frac{r}{\|r\|_2}, \ s = \|r\|_2 e_1$

$\quad$ *For i=1, $\cdots$, m*

$\quad\quad w = Av_i$

$\quad\quad$ *For k=1, $\cdots$, i*

$$h_{k,i} = (w, v_k)$$

$$w = w - h_{k,i}v_k$$

End %end of k loop

$$h_{i+1,i} = \|w\|_2$$

$$v_{i+1} = \frac{w}{h_{i+1,i}}$$

Construct J_i acting on ith and (i+1)st component of $h = (h_{1,i}, h_{2,i}, \cdots, h_{i+1,i})$
such that $(i+1)$st component of J_ih^T is 0

$$s = J_i s$$

If $s(i+1)$ is small enough then UPDATE$(\widehat{x}, i)$ and quit.

End %end of i loop

UPDATE$(\widehat{x}, m)$

End %end of j loop

In this scheme UPDATE$(\widehat{x}, i)$ represents the following computations:

Compute y as the solution of $Hy = \widehat{s}$, in which the upper $i \times i$ triangular part of H has $h_{i,j}$ as its elements and $\widehat{s}$ represents the first icomponents of s

$$\widehat{x} = x_0 + y_1 v_1 + y_2 v_2 + \cdots + y_i v_i$$

$$s_{i+1} = \|b - A\widehat{x}\|_2$$

if $\widehat{x}$is an accurate enough approximation then quit

else $x_0 = \widehat{x}$

The major drawback to GMRES is that the amount of work and storage required per iteration rises linearly with the iteration count. Unless one is fortunate enough to obtain extremely fast convergence, the cost will rapidly become prohibitive. The usual way to overcome this limitation is by restarting the iteration. After a chosen number (m) of iterations, the accumulated data are cleared and the intermediate results are used as the initial data for the next m iterations. This procedure is repeated until convergence is achieved. The difficulty is in choosing an appropriate

value for m. If m is "too small", GMRES(m) may be slow to converge, or fail to converge entirely. A value of m that is larger than necessary involves excessive work (and uses more storage). Unfortunately, there are no definite rules governing the choice of m - choosing when to restart is a matter of experience.

VITA

Zeyun Wu was born in Jiangsu, China. He is the elder of the twin sons of Lagou Wu and Liuzhen Xia. He grew up in Danyang, Jiangsu Province, China. He enrolled in the Department of Engineering Physics of Tsinghua University in 1995 and obtained his B.S. and M.S.E degree from Tsinghua University in 1999 and 2001 respectively. Upon graduation from Tsinghua, he came to the Department of Nuclear Engineering, Texas A&M University to continue his studies. He worked as a graduate research assistant at the master level from Jan. 2002 to Aug. 2005 involved in a research project on neutroncis analysis of an accelerator driven thorium reactor system. He obtained his M.E degree from Texas A&M University in August 2005 and at the same time he started his Ph.D. program in the Department of Nuclear Engineering of Texas A&M University with the research topic of advances in inverse transport methods apply to neutron tomography problems. He will receive his Ph.D. degree in December 2010. Zeyun Wu married Yayun Yu in Dec. 2005 in Danyang, China. They now live together in the U.S.A. and have no kids. Zeyun Wu's interests include badminton sports, travelling, reading etc. He can be reached at zeyunwu@hotmail.com or the following address: Department of Nuclear Engineering, Texas A&M University, 3133 TAMU, College Station, TX 77843-3133.